Beyond ΛCDM: Investigating Alternative Dark Energy Models with Weak Lensing Probes

A Thesis Presented

by

Kunhao Zhong

to

The Graduate School

in Partial Fulfillment of the Requirements

for the Degree of

Master of Arts

in

Physics

Stony Brook University

May 2023

Stony Brook University

The Graduate School

Kunhao Zhong

We, the thesis committee for the above candidate for the Master of Arts degree, hereby recommend acceptance of this thesis.

Vivian Miranda – Thesis Advisor
Professor, Yang Institute of Theoretical Physics

George Sterman – Chairperson of Defense
Professor, Yang Institute of Theoretical Physics

Neelima Sehgal
Professor, Department of Physics and Astronomy

This thesis is accepted by the Graduate School.

Eric Wertheimer
Dean of the Graduate School

Abstract of the Thesis

Beyond ΛCDM: Investigating Alternative Dark Energy Models with Weak Lensing Probes

by

Kunhao Zhong

Stony Brook University

2023

Current weak lensing surveys provide valuable data that enables us to test models beyond the standard ΛCDM. The correlation between different data sets requires us to understand the possible tensions. In this M.A. thesis, we study various aspects of dark energy physics and provide new perspectives on the current cosmology tensions. We start with the key project of the thesis: splitting geometry and growth to test the smooth dark energy paradigm, which offers a model-independent test of a large scope of dark energy theories. We then discuss two specific models that include anisotropic stress in the dark energy fluid description and non-canonical terms in the scalar field description. We also study the early dark energy as the solution to the Hubble tension with the marginalization of the late time expansion. In the end, we present a power emulator between cosmological parameters and weak lensing data vectors, using the state-of-the-art deep learning model, transformers. With all the tools and theories developed, we show how the upcoming data could revolutionize our understanding of the growth of cosmic structures and theories of dark energy.

Contents

Acknowledgements **vii**

List of Figures **ix**

1 Introduction **1**
1.1 Introduction 1
1.2 Chapter Summaries 3

2 Probes to the Universe **5**
2.1 Weak lensing and Galaxy clustering 5
2.1.1 Gravitational Lensing 6
2.1.2 Two-Point Correlation Functions 8
2.1.3 Measurements and Estimators 11
2.1.4 Systematics of 3x2pt Analysis 15
2.2 Cosmic Microwave Background 17
2.2.1 A Very Brief Introduction to CMB 17
2.2.2 CMB Lensing and Cross-Correlations with Galaxy Weak Lensing 18
2.3 BAO, SNIa, and BBN 20
2.3.1 Baryon Accoustic Oscillation 20
2.3.2 Supernovae Type Ia 21
2.3.3 Big Bang Nucleosynthesis 21
2.4 Discussion 23

3 Growth-Geometry Split as a Model Independent Test **24**
3.1 Growth and Geometry of the Cosmic Evolution 24
3.2 Split Growth and Geometry 26
3.2.1 Analysis Choices 26
3.2.2 Non-linearities, Neutrinos, and Comparison to Other Split Formalism 27
3.2.3 Effects of the Split 29

3.3 Results with DES-Y1/Y3 . . . 31
3.3.1 Baseline Results . . . 31
3.3.2 Tensions . . . 33
3.4 Discussion . . . 35

4 Models of Dark Energy I: Fluids **39**
4.1 Problems of ΛCDM . . . 39
4.2 Eulerian Perturbation Theory . . . 40
4.2.1 Metric Perturbation . . . 41
4.2.2 Einstein Equation and Perfect Fluids . . . 42
4.2.3 Distribution Function and Phase Space . . . 43
4.3 Dark Energy as a Non-Smooth Fluid . . . 45
4.3.1 Anisotropic Stress of Dark Energy . . . 45
4.3.2 Modifications to the 2PCF in Galaxy Shear and Overdensity . . . 48

5 Models of Dark Energy II: Scalars **50**
5.1 Basics: A general scalar field . . . 50
5.1.1 Separable Lagrangian . . . 52
5.1.2 Field Redefinition . . . 52
5.2 Properties of k-essence . . . 52
5.2.1 Stability . . . 53
5.2.2 Attractors . . . 53
5.2.3 Dilatonic Ghost Condensate: A Example . . . 55
5.2.4 Phantom Behavior . . . 56
5.3 Perturbations in k-essence . . . 56
5.3.1 Perturbation Equations In Newtonian Gauge . . . 56
5.3.2 Subhorizon approximation . . . 58
5.3.3 Perturbation Equations in Synchronous Gauge . . . 58
5.4 Discussion . . . 61

6 The Hubble Tension and Early Dark Energy **63**
6.1 Hubble Tension . . . 63
6.1.1 Hubble Constant Inferred from CMB . . . 63
6.1.2 Tension between Local Measurement and Possible Solutions . . . 65
6.2 Models of Early Dark Energy . . . 66
6.3 Interacting Neutrinos . . . 67
6.4 Early + Later Dark Energy . . . 69
6.5 Discussion . . . 71

7 Emulator with Deep Learning to Boost Cosmological Inference **72**
7.1 Neural Network 73
7.2 Emulator Design 73
7.2.1 Latin HyperCube 73
7.2.2 Loss Function and Data Pre-Processing 74
7.2.3 Transformer: Attention is all you need 75
7.3 Usage of the Emulator 77
7.3.1 Validations of the Emulator 77
7.3.2 Mapping the growth geometry split to other expansion history 79
7.4 Discussion 79

Bibliography **82**

Acknowledgements

I would like to express my sincere gratitude to all those who have contributed to the completion of my Master thesis. This has been an incredible journey that has challenged me, inspired me, and taught me so much. Without the support, guidance, and encouragement of so many individuals and organizations, this accomplishment would not have been possible.

First and foremost, I am deeply grateful to my advisor Dr. Vivian Miranda for her guidance, mentorship, and support throughout my studies. Her contribution to this thesis and my study goes well beyond being a conventional advisor for a master student. Her expertise, patience, and encouragement were instrumental in shaping my research and developing my skills as a scientist. Her commitment to excellence and passion for the field of cosmology inspired me to pursue this challenging and rewarding path. I will never forget the time we spent together solving problems in coding and physics and the casual chat we had during the walk to the railway station. The support from Vivian made my two-year stay at Stony Brook so valuable and joyful.

I would like to thank other brilliant scientists with whom I had the opportunity to collaborate and work closely during my studies. I would like to thank Dr. Tim Eifler for his invaluable insights and contributions to the project of geometry and growth split. I would also like to thank Dr. Elisabeth Krause and other scientists at the University of Arizona, without whom the project would be impossible. I would also like to thank Dr. Rogerio Rosenfeld and the students at ICTP-SAIFR for their support in studying early dark energy. Their collaboration and support are essential to my early stage of studying cosmology. I am grateful to have had the opportunity to work with such talented and dedicated scientists, and I look forward to future collaborations and conversations.

I am also grateful to my colleagues and peers for their helpful discussions, feedback, and support along the way. Their unique perspectives, insights, and expertise enriched my research and challenged me to think critically and creatively. That includes my cohort: Jonathan Gordon, Evan Saraivanov, Huangfei Xiao, and postdoctoral researcher Joshua Kable. I want to especially

thank Evan for teaching me so much about Machine Learning, making the emulator part of the thesis possible, contributing to other projects, and sharing the anxiety in the application season. I also thank other members of the Stony Brook cosmology group for insightful discussions in the journal club. I would also like to thank my friends that live geographically far away but taught me so much, particularly Jiachuan Xu at the University of Arizona for helping me with the CMB lensing correlations and Xuheng Luo at Johns Hopkins University for the discussion of particle physics.

I would also like to express my gratitude to the faculty and staff in the Physics and Astronomy department at Stony Brook University, as well as the Yang Institute for Theoretical Physics, for their assistance and support during my time here. I would like to thank Dr. Rouven Essig for teaching me electro-weak theory and Dr. Neelima Sehgal for teaching me various subjects in astrophysics. I also thank other senior members at Dark Emergy Survey for enriching my understanding of weak lensing and for the feedback on my projects. Their dedication to education and research, as well as their passion for their respective fields, created a dynamic and inspiring academic environment that fostered my intellectual growth and development.

Furthermore, I would like to acknowledge the support and encouragement of my family and loved ones throughout my academic journey. My parents Wang. Liping, Zhong. Jinhua, my brother, my brother Zhong. Rui, and sister Liu. Yunyin. Their unwavering belief in me and constant love and support have been a source of strength and inspiration during challenging times. Also, special thanks to my cute niece and nephew, your greetings from the other half of the globe always make my day happy.

I would be remiss if I didn't mention how privileged I am during these two difficult years for many people in the world. I could think about galaxies and the universe in comfort while others need to worry about their very basic needs. I am indebted to all the people who work hard for the good of society, to people who fight for others' justice, and to people who make the world a better place. I hope my work can one day be part of it.

To everyone who has played a role in my academic and personal growth, I am deeply grateful for your support and encouragement. Thank you for being part of this journey with me.

List of Figures

2.1 Illustration of different angle defined between real space angle $\boldsymbol{\theta}$, and Fourier vector $\boldsymbol{l}$. The choice of basis $\hat{e}_{1/2}$ is arbitraty. . 9
2.2 Weak lensing two-point correlation function measured from the catalog using TreeCorr. 14
2.3 *Upper*: Glaxy position cross CMB lensing power spectrum. *Lower*: Glaxy shear cross CMB lensing power spectrum. . . . 20

3.1 The different effects of geometry and growth parameters on power spectrum. When changing one parameter, we keep the other at the value $\Omega_{\rm m}$ at 0.3. 28
3.2 σ_8 change under the split parameter change. The solid line shows the change of growth and geometry parameter $\Omega_{\rm m}$ or w simultaneously, same as in the unsplit case, whereas the dashed line is changing the growth parameter only and keeping the geometry parameter the same. It can be seen that the change of growth parameter $\Omega_{\rm m}^{\rm growth}$ results in a smaller change of $\sigma_8(z)$, whereas $w^{\rm growth}$ gives a larger change compared with their geometry parameter counterparts. 29
3.3 Parameter derivative of 2PCF. The derivative is taken around the fiducial value and approximated with 0.1% for all parameters. Both the data and theoretical prediction shown above are after the standard scale cut and using the Y3 modeling method. 30
3.4 Cosmological constraints on split ΛCDM. On the left is 3x2pt with Y1 and Y3 data, and on the right is Y3 data with different combinations of 2PCF and cosmic shear only. The dashed grey line on each plot corresponds to $\Omega_{\rm m}^{\rm growth} = \Omega_{\rm m}^{\rm geo}$. 32
3.5 The cosmological constraints on wCDM. We also show the combination of the difference between growth and geometry, i.e. $\Delta w \equiv w^{\rm growth} - w^{\rm geo}$ and $\Delta\Omega_{\rm m} \equiv \Omega_{\rm m}^{\rm growth} - \Omega_{\rm m}^{\rm geo}$ 33
3.6 Internal Tension of split LCDM cosmology under DES-Y1/Y3 with different geometry priors. 35

4.1 The power spectrum of Wely-Wely and matter-matter under LCDM and PPF-anisotropic-stress model. 49

5.1 Effects of a Dilatonic Ghost Field on the linear matter power spectrum. a is the amplitude of the second-order derivative term. 62

67figure.6.1
6.2 Posterior distribution of LCDM+EDE model. Here DC1 stands for dataset combination 1: CMB (ACT+Planck) + BAO + SNe + CMB-lensing 68
6.3 1D Posterior distribution of wCDM+EDE with a piecewise w under different data set combinations. DC1 stands for dataset combination 1: CMB (ACT+Planck) + BAO + SNe + CMB-lensing. DC2 includes every data set as in DC1 except CMB-lensing. 70

7.1 Architecture of the Neural Network using transformer block. *Upper panel*: In this work, our input dimension is 18 for LCDM and 20 for wCDM. The output dimension of the 3x2pt data vector is 1560. We use the 16 embedding vectors with each of them having a dimension of 128. The total trainable parameters are about 3.5 million. *Lower panel*: the comparison of different network designs for the tension metric calibration project. The x-axis is the total trainable parameters. The transformer block provides orders of magnitude increase in accuracy. 76
7.2 *Upper Panel*: The χ^2 difference between the emulator and CosmoLike. The average χ^2 is about 0.3 after the standard scale cut. *Lower Panel*: The posterior comparison of the MCMC chains using Emulator and Cocoa. As should be expected from the χ^2 plot, there is no difference even near the boundary of the prior range. Note that this is actually a less stringent test since even a larger χ^2 difference at each point could produce the same posterior distribution. 78

7.3 The mapping between w0wa cosmology and the split ΛCDM geometry and growth parameters. We do the minimizer for each point of the w0wa chain to find the maximum likelihood correspondence of the split parameters. The upper and lower panel shows the same result in different projections. The plot shows that even in the case we keep the $w = -1$ in studying the growth geometry split with the underlying cosmology to vary following w0wa, the formalism would not give significant detection of growth $\neq$ geometry. 80

Chapter 1

Introduction

"The effort to understand the universe is one of the very few things that lifts human life a little above the level of farce, and gives it some of the grace of tragedy."

Steven Weinberg

1.1 Introduction

Cosmology is a thriving field that combines theory and observation to understand the fundamental nature of the universe. It is an exciting time for both theory and observation. Our standard model of cosmology is challenged by new data, with two tensions that could hint at new physics. In the upcoming years, advances in observational techniques and the advent of new telescopes and instruments will open up new avenues of research, including the search for evidence of inflation, the study of the growth of cosmic structures, and the exploration of the nature of dark matter and dark energy.

With only a few fundamental parameters, the ΛCDM predicts the temperature and polarization anisotropy of Cosmic Microwave Background (CMB), measured in high accuracy by *Planck* [1, 2], which in turn enable us to constrain the cosmological parameters with small error bars such as the energy density of matter $\Omega_{\rm m}$. The sky surveys also show increasing power to constrain cosmological parameters from the evolution of large-scale structures (LSS). The current generation, called Stage-III, includes Dark Energy Survey(DES)[1] [3–6], the Kilo-Degree Survey(KiDS) [2] [7, 8], the Hyper Suprime-Cam Sub-

[1]https://www.darkenergysurvey.org/

[2]https://kids.strw.leidenuniv.nl/

aru Strategic Program (HSC) [3] [9–11], and the Extended Baryon Oscillation Spectroscopic Survey (eBOSS) [4] [12].

Yet, the origin of dark energy is still unknown. The cosmological constant as a vacuum energy is very fine-tuned, and its value is too small to any known quantum field theory [13]. A dynamical field, called quintessence, was proposed to solve either the fine-tuning problem or the coincidence problem [14], through a dynamical system approach. Models with a non-canonical kinetic term, k-essence, were proposed to solve the two problems simultaneously [15]. Modified gravity is also a way to explain the acceleration of the universe without introducing a new component. But none of them are confirmed by the current observation yet.

On the other hand, two cosmological tensions have become more and more significant in recent years, indicating an inevitable modification to the standard cosmological model ΛCDM. The value of two commonly used parameters, H_0 and S_8, is in a discrepancy between the inferred value from the early universe and the direct measurement of the late universe. The Hubble constant H_0 is now at 5σ discrepancy between the value inferred from CMB anisotropy and local direct measurement [16]. The value of $S_8 \equiv \sigma_8\sqrt{\Omega_m/0.3}$, where σ_8 is the root mean variance of matter perturbation within 8 Mpc/h, is also different from the CMB measurement in local LSS probe, at about $2-3\sigma$ level. Several different late-time probes favor a lower value of S_8, including galaxy weak lensing and clustering [17], redshift-space distortions(RSD)[18] and abundance of galaxy clusters [19]. These probes do not assume a specific early universe model but rather directly measure the structure of galaxies and mass and their evolution. For instance, the two-point correlation between galaxy positions (galaxy clustering) gave early evidence of dark energy [20] 25 years before the confirmation from Type Ia Supernovae. With the correlation of galaxy shear (galaxy-galaxy lensing), it can now give cosmological constraints comparable to other probes [21–23], despite the complexity of galaxy bias and other systematics. Cross-correlation between galaxy shears (cosmic shear), on the other hand, is directly related to the mass distribution and thus avoids the non-linearities in small scale [24]. As all the probes combined, the evidence for the possible tension in ΛCDM is stronger.

Several upcoming cosmological surveys are poised to revolutionize our understanding of the universe. The Large Synoptic Survey Telescope (LSST) in Chile will image the entire southern sky in multiple wavelengths, detecting billions of galaxies and measuring their properties with unprecedented accuracy. The Dark Energy Spectroscopic Instrument (DESI) in Arizona will use

[3] https://www.naoj.org/Projects/HSC/

[4] https://www.sdss.org/surveys/eboss/

fiber-optic cables to measure the distances to millions of galaxies and quasars, creating a three-dimensional map of the universe. The Euclid satellite mission, led by the European Space Agency, will measure the shapes and distances of billions of galaxies using both visible and near-infrared light. The Spectro-Photometer for the History of the Universe, Epoch of Reionization, and Ices Explorer (SPHEREx) will probe inflation physics that is imprinted in the galaxy formation history. Finally, the Roman Space Telescope, formerly known as WFIRST, will study the properties of dark energy and dark matter, surveying large sky areas in both visible and infrared light. Together, these surveys will provide a wealth of new data that will help us refine our models of the universe and address some of the biggest questions in cosmology.

Despite their immense scientific potential, the data from upcoming cosmological surveys will pose significant challenges for analysis. The vast data these surveys produce will require sophisticated algorithms and computing resources to process and analyze. Additionally, the accuracy of the measurements will be limited by various systematic effects, including atmospheric turbulence, instrument noise, and calibration errors. To overcome these challenges, cosmologists must develop new statistical techniques and modeling frameworks to account for these systematic effects and accurately extract the desired cosmological parameters from the data. Furthermore, given the complexity and size of these data sets, collaboration and sharing of resources will be essential, requiring a concerted effort from the scientific community to develop open and transparent data analysis pipelines. Despite these challenges, the potential rewards of these surveys make an effort to analyze their data well worth it.

1.2 Chapter Summaries

In Chapter 2 we discuss the probes to the universe. We focus on galaxy weak lensing and galaxy clustering and introduce the theories of large-scale structure imaging surveys. We show the precision measurement of CMB and how it complements weak lensing survey. We briefly discuss other distance or geometry measurements such as BAO, SNIa, and BBN. We end the chapter by briefly discussing other probes and future surveys.

In Chapter 3 we show the main result of my master research: splitting geometry and growth and test the consistency of the smooth dark energy paradigm. Following the discussion in Chapter 2, we discuss how we choose data set combinations to separate growth and geometry information and present the formalism with various validation steps on synthetic data. We show the results with DES data in 3.3.

In Chapter 4 and Chapter 5 we discuss two extension models to dark

energy: dark energy fluid with anisotropic stress and non-canonical scalar field. We show their effect on cosmic probes, mainly on large-scale structures, with our modified version of the Boltzmann code. We present the constraints on these models with current DES data and future survey forecasts.

Finally, in Chapter 7, we discuss how we utilize a machine-learning-based algorithm to boost the computation of weak lensing analysis. We validate the results and compare our choices to previous emulators. We end the chapter with an example of its application and illustrate why it benefits the upcoming analysis.

Chapter 2

Probes to the Universe

In this chapter, we briefly discuss different probes to the universe, with a focus on galaxy weak lensing, galaxy clustering, and CMB lensing. As we will see, probes to the universe can be divided into two categories, one probes the geometry of the cosmological evolution, and the other probes the growth of structures. This is the motivation for the split formalism we discuss in Chapter 3.

2.1 Weak lensing and Galaxy clustering

Large Scale Structure measurements can be roughly divided into spectroscopic and photometric. In this section, we introduce the key quality in photometric survey summary statistics: the 3x2pt function.

Weak lensing probes the small-scale perturbation. Because weak lensing depends on the gravitational potential, the transformation between the shear field and matter power spectrum is rather linear. It is not easy, however, to measure the shear field because a galaxy has its own shape, and the shapes themselves are poorly understood. That is the reason why weak lensing surveys need large sky coverage and need hundreds of millions of galaxies to reach statistical significance.

Galaxy clustering, on the other hand, assumes galaxies as tracers to the underlying matter field (mostly dark matter) and thus is more non-linear. Their correlation, so-called galaxy-galaxy lensing, associates these two fields. Together, these three measurements are called 3x2pt and are the main result of photometric surveys such as KiDs and DES.

In this subsection, we go through the key derivations of 3x2pt, including the basics, measurement, and systematics. We start with the basics of gravitational lensing.

2.1.1 Gravitational Lensing

Although the idea of gravitational lensing is familiar to most of the audience since it is one of the three classical tests of general relativity, we give the formalism here in the cosmological context. By the end of the section, it will be clear why we would consider the anisotropic stress of dark energy and how it relates to weak lensing. This section mostly follows section 10.2 of Ref [25].

Let the photon traveling in the universe have position $\boldsymbol{x}$, x^3 being the radial distance χ, and the transverse components equal to $\chi\boldsymbol{\theta}$. The geodesic equation follows:

$$\frac{d^2x^i}{d\lambda^2} = -\Gamma^i_{\alpha\beta}\frac{dx^\alpha}{d\lambda}\frac{dx^\beta}{d\lambda}, \tag{2.1}$$

where λ is the affine parameter. In FRW cosmology, we have

$$\frac{d\chi}{d\lambda} = \frac{d\chi}{dt}\frac{dt}{d\lambda} = \frac{-1}{a}p(1-\Psi), \tag{2.2}$$

where p is the space-space component of the photon, and Ψ is the perturbation of the time-time component of the metric in Newtonian gauge [1]. The geodesic equation 2.2 thus reduces to

$$\Gamma^i_{\alpha\beta}\frac{dx^\alpha}{d\lambda}\frac{dx^\beta}{d\lambda} = \left(\frac{p}{a}\right)^2(1-\Psi)^2\Gamma^i_{\alpha\beta}\frac{dx^\alpha}{d\chi}\frac{dx^\beta}{d\chi}. \tag{2.3}$$

Collecting the transverse component and neglecting second-order terms gives the transverse displacement

$$\frac{d^2}{d\chi^2}(\chi\theta^i) = \Phi - \Psi, \tag{2.4}$$

and integrating the displacement equation twice (be careful with the integral range) we have the difference between the observed angle θ^i, and the real angle θ^i_S:

$$\theta^i_S = \theta^i + \int_0^\chi d\chi' \left(\Phi_{,i}\left(\boldsymbol{x}\left(\chi'\right)\right) - \Psi_{,i}\left(\boldsymbol{x}\left(\chi'\right)\right)\right)\left(1 - \frac{\chi'}{\chi}\right). \tag{2.5}$$

Similar to the formalism in CMB polarization split to E mode and B mode, we can define a 2 x 2 symmetric transformation matrix with two fields, con-

[1] The Newtonian gauge is defined as $ds^2 = -(1+2\Phi)dt^2 + a^2(t)(1-2\Psi)\delta_{ab}dx^a dx^b$. For a light-like curve like the geodesic of photon, we have $P^2 = 0 = -(1+2\Psi)(P^0)^2 + p^2$ where P is the 4-momentum $P^\mu \equiv \dfrac{dx^\mu}{d\lambda}$. So assuming the gravitational field is first order gives $P^0 = p(1-\Psi)$

vergence κ and shear γ, as:

$$A_{ij} \equiv \frac{\partial \theta_S^i}{\partial \theta^j} \equiv \begin{pmatrix} 1-\kappa-\gamma_1 & -\gamma_2 \\ -\gamma_2 & 1-\kappa+\gamma_1 \end{pmatrix}, \tag{2.6}$$

then the shear field γ is:

$$\begin{aligned} \gamma_1 &= -\frac{A_{11}-A_{22}}{2} \\ \gamma_2 &= -A_{12} \end{aligned} \tag{2.7}$$

Since the only θ^i dependent variable of Eq 2.5 is $\boldsymbol{x}(\chi') = \chi'\boldsymbol{\theta}$, $d/d\theta^i = \chi' d/dx^i$. The shear field is then fully determined by the gravitational potential:

$$\psi_{ij} \equiv A_{ij} - \delta_{ij} = \int_0^\chi d\chi' \left(\Phi_{,ij}\left(\boldsymbol{x}\right) - \Psi_{,ij}\left(\boldsymbol{x}\right)\right) \chi' \left(1 - \frac{\chi'}{\chi}\right), \tag{2.8}$$

where ψ_{ij} is called distortion tensor. In ΛCDM, there is no late-time anisotropic stress, namely $\Psi = -\Phi$. In Sec. 4.3.1 we relax this requirement and test the shear stress term induced by dark energy.

Similar to CMB angular correlations, a galaxy survey has a window function that contains the information of redshift distribution $W(\chi)$, such that $\int d\chi W(\chi) = 1$. So,

$$\psi_{ij}(\boldsymbol{\theta}) = \int_0^{\chi_\infty} d\chi \Phi_{,ij}(\boldsymbol{x}(\chi)) q(\chi), \tag{2.9}$$

where

$$q(\chi) \equiv 2\chi \int_\chi^{\chi_\infty} d\chi' \left(1 - \frac{\chi}{\chi'}\right) W\left(\chi'\right). \tag{2.10}$$

The naming convention here differs in literature, but most of them call $q(\chi)$ as the weighting function, and the window function in a photometric survey usually takes the form:

$$W\left(\chi'\right) = \frac{n_{\rm g}^i(z(\chi))}{\bar{n}_{\rm g}^i} \frac{dz}{d\chi}, \tag{2.11}$$

where $\bar{n}_{{\rm g}/\kappa}^i = \int dz\, n_{{\rm g}/\kappa}^i(z)$ is the angular number density of galaxies in the redshift bin i. We will summarize the notation from matter power spectrum to angular two-point correlation functions in the end, or see Ref [26] for a comprehensive summary. For now, let's continue on how angular correlation functions are related to two-point correlation functions. Then in Sec. 2.1.3 we would discuss how this is measured.

2.1.2 Two-Point Correlation Functions

The power spectrum of the gravitational potential in the momentum space is defined as:

$$k_i k_j k'_l k'_m \left\langle \tilde{\Phi}(\boldsymbol{k})\tilde{\Phi}^*\left(\boldsymbol{k}'\right)\right\rangle = (2\pi)^3 k_i k_j k_l k_m \delta^3\left(\boldsymbol{k}-\boldsymbol{k}'\right) P_\Phi(k). \tag{2.12}$$

In this section, we assume the normal Poisson equation in the Newtonian gauge

$$k^2\Phi = 4\pi G a^2 \sum_{\mathrm{a}} \left(\delta\rho_{\mathrm{a}}\right), \tag{2.13}$$

and thus the power spectrum of Newtonian potential is proportional to the matter power spectrum.

Under the small angle approximation (Limber approximation, see Ref [27, 28] for details), $l/\chi \; 1/(\chi\theta) \gg 1/\chi$, only modes with k_3 smaller than χ^{-1} contributes to angular correlation. Then the 3D power spectrum transforms to the 2D projected version, or the angular power spectrum:

$$\left\langle \tilde{\psi}_{ij}(\boldsymbol{l})\tilde{\psi}_{lm}(\boldsymbol{l})\right\rangle = (2\pi)^2\delta^2\left(\boldsymbol{l}-\boldsymbol{l}'\right) P^{\psi}_{ijlm}(\boldsymbol{l}), \tag{2.14}$$

with

$$P^{\psi}_{ijlm}(\boldsymbol{l}) = \int_0^{\chi_\infty} d\chi \frac{g^2(\chi)}{\chi^2}\frac{l_i l_j l_l l_m}{\chi^4} P_\Phi(l/\chi). \tag{2.15}$$

Noticing that $\gamma_1 = \left(\psi_{22}-\psi_{11}\right)/2$ and decomposing $\boldsymbol{l}$ to the radial coordinate l, ϕ_l we have:

$$P_{\gamma_1}\left(l,\phi_l\right) = \left(\sin^4\phi_l + \cos^4\phi_l - 2\sin^2\phi_l\cos^2\phi_l\right)\left[\frac{l^4}{4}\int_0^{\chi_\infty} d\chi \frac{q^2(\chi)}{\chi^6} P_\Phi(l/\chi)\right], \tag{2.16}$$

where ϕ_l is the angle between Fourier vector $\boldsymbol{l}$ and the first axis. One can show the bracket is equal to the power spectrum of the convergence field:

$$P_\kappa = \frac{l^4}{4}\int_0^{\chi_\infty} d\chi \frac{g^2(\chi)}{\chi^6} P_\Phi(l/\chi). \tag{2.17}$$

In the literature of weak lensing and most of the LSS surveys, the correlations are calculated and compared with measurements in real space, namely an angular scale in the sky θ. Here we summarize one example of cosmic shear. The Fourier transform can be algebraically complicated when relaxing the flat-sky assumption or with an angular scale binning. For that, see Ref [29–31].

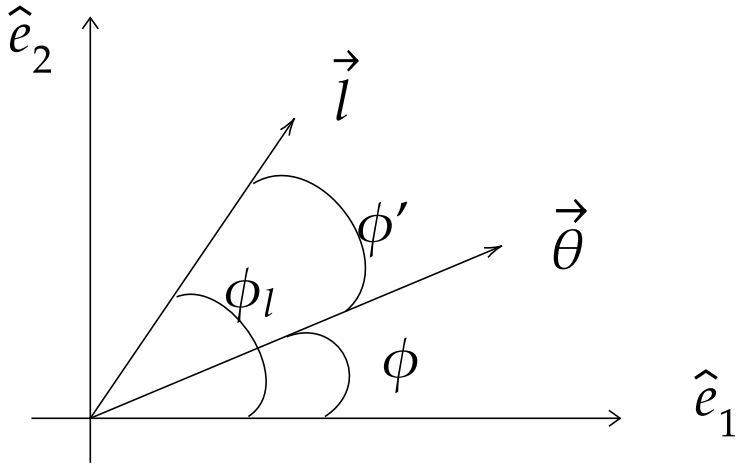


Figure 2.1: Illustration of different angle defined between real space angle $\boldsymbol{\theta}$, and Fourier vector $\boldsymbol{l}$. The choice of basis $\hat{e}_{1/2}$ is arbitraty.

The Fourier transform of Eq. 2.16 is:

$$\zeta_{\gamma_1}(\boldsymbol{\theta}) \equiv \int \frac{d^2l}{(2\pi)^2} e^{i\boldsymbol{l}\cdot\boldsymbol{\theta}} \cos^2(2\phi_l) \left[\frac{l^4}{4}\int_0^{\chi_\infty} d\chi \frac{g^2(\chi)}{\chi^6} P_\Phi(l/\chi)\right]. \tag{2.18}$$

The integral of the exponential function can be largely simplified by integrating over the difference between $\boldsymbol{l}$ and $\boldsymbol{\theta}$, and call it ϕ'. Then:

$$\zeta_{\gamma_1}(\boldsymbol{\theta}) = \int_0^\infty \frac{dl}{(2\pi)^2}\frac{l^5}{4}\int_0^\chi d\chi \frac{g^2(\chi)}{\chi^6} P_\Phi(l/\chi) \int_0^{2\pi} d\phi' e^{il\theta\cos\phi'} \left[\cos\left(2\left(\phi'+\phi\right)\right)\right]^2. \tag{2.19}$$

Expanding the trigonometric functions and using the equation of Bessel function integrals:

$$J_n(x) = \frac{i^{-n}}{\pi}\int_0^\pi d\theta e^{ix\cos\theta}\cos(n\theta), \tag{2.20}$$

we have:

$$\begin{aligned}\zeta_{\gamma_1}(\boldsymbol{\theta}) =& \frac{1}{16\pi}\int_0^\infty dl l^5 \int_0^{\chi_\infty} d\chi \frac{g^2(\chi)}{\chi^6} P_\Phi(l/\chi) \\ & \times \left\{\cos^2(2\phi)\left[J_0(l\theta)+J_4(l\theta)\right] + \sin^2(2\phi)\left[J_0(l\theta)-J_4(l\theta)\right]\right\}\end{aligned} \tag{2.21}$$

The first axis $\hat{e}_1$ is usually taken as the line that connects galaxy pairs of

measurement, namely $\phi = 0$. Thus:

$$\zeta_{\gamma_1}(\boldsymbol{\theta}) = \frac{1}{16\pi}\int_0^\infty dll^5 \int_0^{\chi_\infty} d\chi \frac{g^2(\chi)}{\chi^6} P_\Phi(l/\chi) \times \{J_0(l\theta) + J_4(l\theta)\} \tag{2.22}$$

Conventional Notations in Weak Lensing Survey

Using the relation that $P_m = 9\Omega_m^2 H_0^4 (1+z)^2 / (4k^4) P_\Phi$, and $k = l/\chi$, we see that Eq.2.21 has the same form of weight on χ. The usual 2PCF of shear-shear (cosmic shear) is decomposed into two parts $\xi_\pm$,defined in the literature as:

$$\xi^{ij}_{+/-}(\theta) = \int \frac{dll}{2\pi} J_{0/4}(l\theta) \int d\chi \frac{q^i_\kappa(\chi) q^j_\kappa(\chi)}{\chi^2} P_{\rm NL}\left(\frac{l+1/2}{\chi}, z(\chi)\right). \tag{2.23}$$

One caveat is that there's a correction to the k value evaluation in power spectrum, k is taken in $(l+0.5)/\chi$ instead of l/χ. For details of discussion, see Ref. [31]

Instead of a shear field, galaxy overdensity δ_g is also a tracer of matter distribution, being a scalar instead of the spin-2 field as the distortion tensor. For a scalar field,

$$x_i(\hat{\mathbf{n}}) = \int \frac{d^2 l}{(2\pi)^2} x_i(\mathbf{l}) e^{i\mathbf{l}\cdot\hat{\mathbf{n}}}, \tag{2.24}$$

and its auto-correlation and cross-correlation are called galaxy clustering and galaxy-galaxy lensing, usually denoted as $w(\theta)$ and $\gamma_t(\theta)$. The $w(\theta)$ here is not the same as the Fourier transform as given in the example above. Their relation to the matter power spectrum is similar to the cosmic shear $\xi_\pm$, with the difference in window function and Bessel function.

We omit the detail calculation here, but a simple observation is that instead of $\cos^2(\phi)$ as in the shear-shear case, there is only one $\cos(\theta)$ for cross-correlation and thus give $J_2(l\theta)$ according to Eq. 2.20. Similar to Eq. 2.23, we have:

$$w^i(\theta) = \int \frac{dll}{2\pi} J_0(l\theta) \int d\chi \frac{q^i_{\delta_{\rm g}}\left(\frac{l+1/2}{\chi}, \chi\right) q^j_{\delta_{\rm g}}\left(\frac{l+1/2}{\chi}, \chi\right)}{\chi^2} \times P_{\rm NL}\left(\frac{l+1/2}{\chi}, z(\chi)\right) \tag{2.25}$$

for galaxy clustering (position-position), and

$$\gamma_{\rm t}^{ij}(\theta) = \int \frac{dll}{2\pi} J_2(l\theta) \int d\chi \frac{q^i_{\delta_{\rm g}}\left(\frac{l+1/2}{\chi}, \chi\right) q^j_\kappa(\chi)}{\chi^2} \times P_{\rm NL}\left(\frac{l+1/2}{\chi}, z(\chi)\right) \tag{2.26}$$

for galaxy-galaxy lensing (shear-position).

The radial weight function, $q_{\delta_{\rm g}}$, for density fluctuation is similar as defined above, but with redshift binning and usually with a linear galaxy bias $b(k,z)$ that characterizes the mass difference between the galaxy and the actual halo:

$$q^i_{\delta_{\rm g}}(k,\chi) = b^i(k,z(\chi))\frac{n^i_{\rm g}(z(\chi))}{\bar{n}^i_{\rm g}}\frac{dz}{d\chi} \tag{2.27}$$

and for lensing efficiency:

$$q^i_\kappa(\chi) = \frac{3H_0^2\Omega_m}{2{\rm c}^2}\frac{\chi}{a(\chi)}\int_\chi^{\chi_{\rm h}} {\rm d}\chi' \frac{n^i_\kappa\left(z\left(\chi'\right)\right)dz/d\chi'}{\bar{n}^i_\kappa}\frac{\chi'-\chi}{\chi'}. \tag{2.28}$$

For how redshift or tomographic binning affect the weak lensing survey, see Ref. [32].

The above formulae are under the assumption of flat-sky and small angles. For the bin-averaged curved sky, the 2PCF in real space is related to the angular power spectrum by:

$$w^i_\theta(\bar{\theta}) = \sum_\ell \frac{2\ell+1}{4\pi}\overline{P_\ell}C^{ii}_{\delta\delta}(\ell)\,, \tag{2.29}$$

$$\gamma^{ij}_t(\bar{\theta}) = \sum_\ell \frac{2\ell+1}{4\pi\ell(\ell+1)}\overline{P^2_\ell}C^{ij}_{\delta{\rm E}}(\ell)\,, \tag{2.30}$$

$$\xi^{ij}_\pm(\bar{\theta}) = \sum_\ell \frac{2\ell+1}{2\pi\ell^2(\ell+1)^2}\overline{[G^+_{\ell,2}\pm G^-_{\ell,2}]}\left[C^{ij}_{EE}(\ell)\pm C^{ij}_{BB}(\ell)\right]\,,$$

where

$$P_\ell(\cos\theta)\to\bar{P}_\ell(\cos\theta) = \frac{[P_{\ell+1}(x)-P_{\ell-1}(x)]^{\cos\theta_{\rm min}}_{\cos\theta_{\rm max}}}{(2\ell+1)(\cos\theta_{\rm min}-\cos\theta_{\rm max})}. \tag{2.31}$$

is the bin-averaged Legendre polynomials. The analytical expressions for Legendre and associated Legendre polynomials $\overline{P_\ell}$ and $\overline{G^\pm_{\ell,2}}$ are calculated in [31]. The angular correlation $C^{ii}_{\delta\delta}(\ell)$, $C^{ij}_{\delta{\rm E}}$, and $C^{ij}_{EE/BB}(\ell)$ are shorthand as the second integral in Eqs. 2.23, 2.25, and 2.26. The E mode and B mode decomposition is similar to the idea introduced above and the definition can be found in the DES-Y3 methods paper [33].

2.1.3 Measurements and Estimators

The shear field can be traced by the ellipticity of galaxies. For an imaging survey, one can define the quadrupole moments as the integral over the intensity

of an image centered at θ_x, θ_y:

$$q_{ij} \equiv \int d^2\theta I_{\rm obs}(\theta)\theta_i\theta_j. \tag{2.32}$$

Since an circular image has $q_{xy} = 0$ and $q_{xx} = q_{yy}$, the ellipsity can be defined as:

$$\epsilon_1 \equiv \frac{q_{xx} - q_{yy}}{q_{xx} + q_{yy}}, \quad , \epsilon_2 \equiv \frac{2q_{xy}}{q_{xx} + q_{yy}}. \tag{2.33}$$

It can be shown that (See Ref. [25] Section 10.3), at the approximation of a small distortion tensor,

$$\epsilon_1 \simeq 2\gamma_1. \tag{2.34}$$

Thus, the ellipticity of galaxies can be the tracers of the shear field.

To really get a measurement of the two-point function, we need what's called an estimator. For simplicity, we introduce the estimator for galaxy clustering as an example. In the case of spin-2 fields (cosmic shear), things can be more complicated than a scalar (galaxy position). We refer the readers to [34] and references therein.

The two-point function that we wish to capture the clustering effect is the excess of the probability of finding galaxies over a random/Poisson distribution, namely:

$$dP = n[1 + w(r)]dV \tag{2.35}$$

where n is the mean number density of galaxies, as in Ref. [35]. In order to make the measurement or catalog that we have over a certain area of the sky, we need a "random" catalog that shares the same properties, for example, the sky coverage and redshift information, but the distribution is manifestly random. Then we can make measurements over the data catalog and random catalog, and the ratio reflects the correlation $w(r)$. The estimator of doing such measurements is not unique, and they have different systematic errors. The earliest estimator proposed is [36]:

$$\xi = \frac{n_R}{n_D}\frac{DD}{DR} - 1, \tag{2.36}$$

where n_R/D is the number density of random and data galaxies, and DD and DR is the count of galaxies between data-data and data-random catalog. Another estimator in the early days is [36]:

$$\xi = \frac{DDRR}{(DR)^2} - 1. \tag{2.37}$$

The most widely used estimator now is called Landy and Szalay estimator [37]:

$$\xi = \frac{1}{RR}\left[DD\left(\frac{n_R}{n_D}\right)^2 - 2DR\left(\frac{n_R}{n_D}\right) + RR\right]. \tag{2.38}$$

which has a small systematic error and is also insensitive to the measurement at the edge of the sky map.

As we can already see from the three estimators above, the computational cost is getting larger and larger. In the LZ estimator, we need to count each galaxy pair between data-data, random-random, and data-random, and the pair counts increase exponentially with the total galaxy numbers.

Making the measurement is a highly non-trivial task. The most common method (and probably the only method) in the community now is to use a tree algorithm (a popular code is called TreeCorr [34]). Tree-algorithm is a data structure that allows an extremely efficient of finding and calculating information of two points pair. For the n-point correlation function of particle number N, an effective tree algorithm can reduce the complexity of a brute-force approach $O(N^n)$ to roughly $O(N\log(N))$.

The calculation we present above does not have tomographic binning information. For a review, see Ref [38]. The two-point functions of galaxy clustering are shown in Fig 2.2, where we show the measurement provided by DES collaboration and the measurement using TreeCorr. The last piece that makes the measurement complete is the covariance matrix of the 2PCF, where its diagonal component gives the error that are included in Fig. 2.2 (in this example of $w(\theta)$ the error bar is kind of small to see). Unlike in the literature of CMB, the weak lensing analysis often use analytical modeling to calculate the non-gaussian part of the covariance matrix. The covariance matrix is defined as usual:

$$C_{ij} \equiv \left\langle \hat{P}_i \hat{P}_j \right\rangle - \left\langle \hat{P}_i \right\rangle \left\langle \hat{P}_j \right\rangle, \tag{2.39}$$

and since it is the product of the power spectrum, one would expect the covariance depends on the trispectrum, defined similarly as:

$$\left\langle \delta\left(\boldsymbol{k}_1\right) \ldots \delta\left(\boldsymbol{k}_4\right)\right\rangle_c = (2\pi)^3 \delta_{\mathrm{D}}\left(\boldsymbol{k}_{1234}\right) T\left(\boldsymbol{k}_1, \boldsymbol{k}_2, \boldsymbol{k}_3, \boldsymbol{k}_4\right). \tag{2.40}$$

During the past few decades, people have developed a complete theory to calculate each term and the part that follows the halo model. The covariance between each probe, for example, the off-diagonal term of cosmic shear and galaxy clustering, was also studied extensively. Unfortunately, the details of the calculation and validation of the covariance matrix are beyond the scope

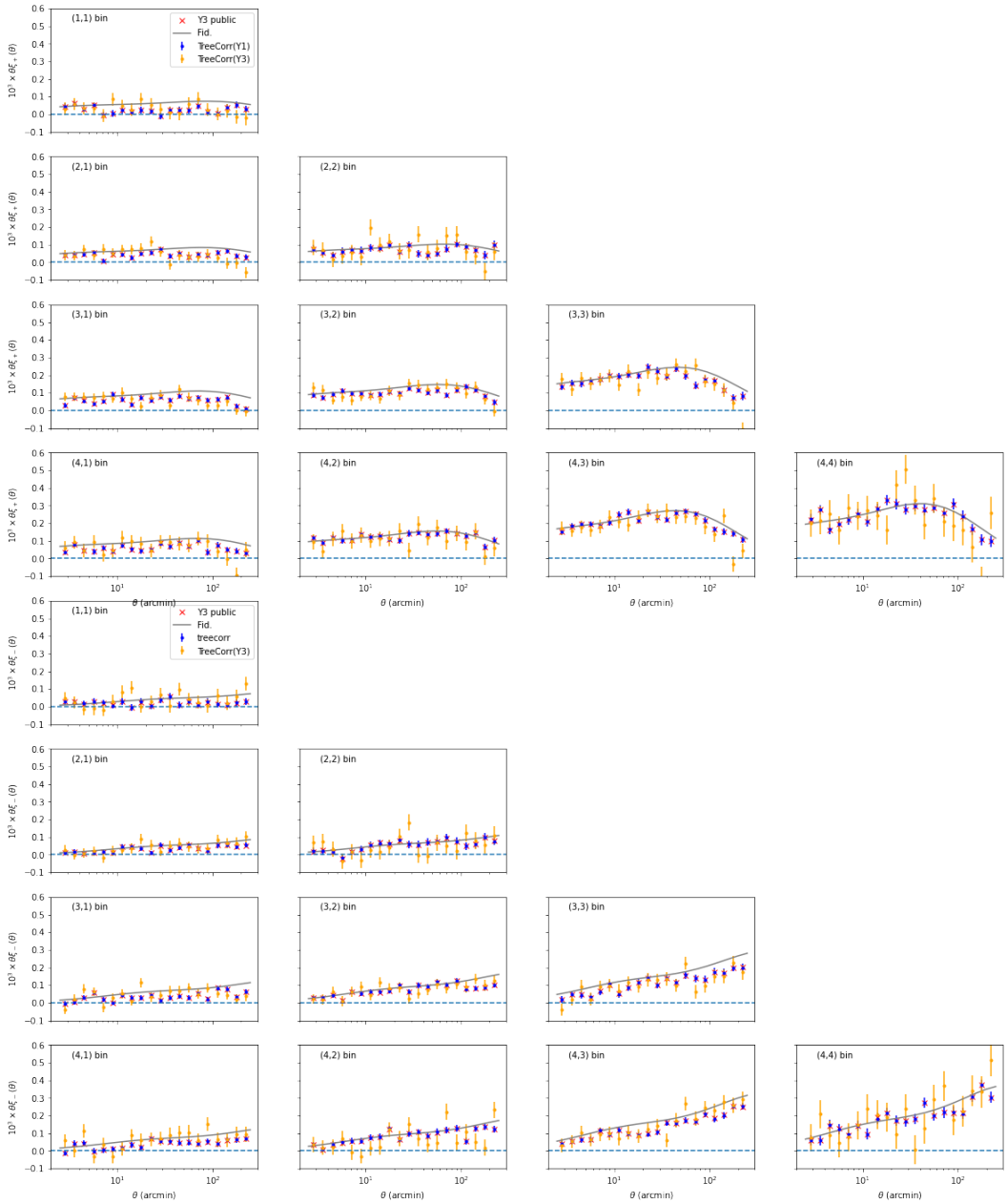


Figure 2.2: Weak lensing two-point correlation function measured from the catalog using TreeCorr.

of this thesis. For details, see [39] and the references within.

2.1.4 Systematics of 3x2pt Analysis

In this subsection, we briefly summarize the systematics that we need to consider in a DES-Y3-like survey. As the measurement becomes more precise, new techniques (mostly simulation) and more complicated modeling of the same effect will become necessary.

Galaxy Bias: The linear galaxy bias is parameterized by a scalar for each redshift bin, i.e. $b^i(k,z) = b^i$, for four redshift bins. It is possible to consider non-linear galaxy bias or scale-dependent bias. See Ref. [40] for the discussion and comparison within DES samples.

Apart from galaxy bias, Halo Occupation Distribution (HOD) is also a way to model the galaxy-halo relation via the probability of $N_{\rm g}$ galaxies in a halo of given mass M. We give a brief introduction here. For detailed derivation and simulation-based validation, see Ref [41–43]. Here we follow the work of [43] where the $N_{\rm g}$ is split into central galaxy number $N_{\rm cen}$, and that of satellite galaxy $N_{\rm sat}$, and their expectation values are modeled as:

$$\begin{aligned}\langle N_{\rm cen}(M)\rangle &= \frac{1}{2}\left[1+{\rm erf}\left(\frac{\log M-\log M_{\rm min}}{\sigma_{\ln M}}\right)\right]\\ \langle N_{\rm sat}(M)\rangle &= \Theta\left(M-M_0\right)\left(\frac{M-M_0}{M_1'}\right)^{\alpha_{\rm sat}}\end{aligned} \tag{2.41}$$

where erf is the error function and Θ a step function. So there are 5 free parameters. It is also possible to include an overall factor $f_{\rm c}$ in $\langle N_{\rm cen}(M)\rangle$ to model the incompleteness in the selectio of LRGs [44]. Thus the total galaxy occupation is modeled as:

$$\langle N_{\rm g}(M)\rangle = \langle N_{\rm c}(M)\rangle\left[f_{\rm c}+\langle N_{\rm s}(M)\rangle\right] \tag{2.42}$$

The galaxy-matter and galaxy-galaxy power spectrum is related to the matter power spectrum as a linear relation plus the integral of the occupation

probability above:

$$
\begin{aligned}
P_{\rm gm}(k,z) &= b_{\rm HOD}(z) P_{\rm lin}(k,z) \\
&\quad + \frac{\int dM \frac{dn}{dM} M u_{\rm m}(k,M) \left\langle N_{\rm c}(M)\right\rangle \left\langle N_{\rm s}(M)\right\rangle u_{\rm s}(k,M)}{\bar{\rho}\int dM \frac{dn}{dM}\left\langle N_{\rm g}(M)\right\rangle} \\
P_{\rm gg}(k,z) &= \left(b_{\rm HOD}(z)\right)^2 P_{\rm lin}(k,z) \\
&\quad + \frac{\int dM \frac{dn}{dM}\left\langle \left\{N_{\rm c}(M)\left[f_{\rm c}+N_{\rm s}(M)\tilde{u}_{\rm s}(k,M)\right)\right]\right\}^2\right\rangle}{\left(\int dM \frac{dn}{dM}\left\langle N_{\rm g}(M)\right\rangle\right)^2}
\end{aligned}
\tag{2.43}
$$

With HOD model, it is possible to push to small scales $R_{\rm min} = 0.1$Mpc/h, where a linear bias adopted by DES is of the order $R_{\rm min} \approx 10$Mpc/h [39]. The HOD model thus substantially increases the constraining power.

Intrinsic Alignment of Galaxy: The Tidal Alignment and Tidal Torquing (TATT) [45] is used to model the intrinsic alignment of galaxies for DES-Y3 data, which is a generalization to the previously used non-linear alignment model (NLA). Under this framework, the intrinsic shape of galaxies is written as a collection of independent terms that describe tidal alignment, tidal torquing, and density weighting:

$$
\gamma^I_{ij} = \underbrace{C_1 s_{ij}}_{\text{Tidal Alignment}} + \underbrace{C_{1\delta}\left(\delta \times s_{ij}\right)}_{\text{Density Weighting}} + \underbrace{C_2\left[\sum_{k=0}^{2} s_{ik}s_{kj} - \frac{1}{3}\delta_{ij}s^2\right]}_{\text{Tidal Torquing}} + \ldots . \tag{2.44}
$$

The TATT model contains five parameters: the amplitude A_i and power law index η_i, with some pivot redshift plus the effective source galaxy bias b_{TA}. The TATT model is reduced to NLA when $A_2 = b_{TA} = 0$. We also marginalized them by a conservative prior: $a_i, \eta_i \in (-5, 5), b_{TA} \in (0, 2)$, and we fix the pivot redshift at $z_0 = 0.62$.

Multiplicative shear calibration: Shear estimation can give a significant bias in cosmological analysis from week lensing [46]. DES-Y3 model the shear calibration with a marginalized parameter m^i for each redshift bin, which affects the cosmic shear and galaxy-galaxy correlation function by:

$$
\xi^{ij}_{\pm}(\theta) \quad \longrightarrow \quad \left(1+m^i\right)\left(1+m^j\right)\xi^{ij}_{\pm}(\theta). \tag{2.45}
$$

The priors used for m^i are calibrated with simulated data in DES-Y3 analysis [47]. As shown in [48], the cross-correlation with CMB lensing generates con-

straints from data only, and it is consistent with the priors from simulated data.

Photometric redshift uncertainties: The uncertainties in photometric redshift distribution for both source and lens galaxies are usually modeled by a shift in each redshift bin:

$$n_x^i(z) = \hat{n}_x^i\left(z - \Delta_{z,x}^i\right), \quad x \in \{\text{source}, \text{lens}\}. \tag{2.46}$$

In [49] we do not model the stretch in lens photo-z by an additional parameter σ_z^i as in the DES-Y3 key project.

An alternative way is to sample over a large number of realizations of the full posteriors [50]. A recent analysis using Bayesian resampling shows that the shift model is good enough for current data [51].

Impact of lensing magnification on lens galaxy density: Magnification of gravitational lensing affects the number of galaxies observed in a given area of sky. As detailed in [33], a parameter C_l^i is defined to describe the foreground mass effects on the observed number density projection of lens galaxies. Comparison of three calibration methods using BALROG image simulation, analytic perturbation of flux, and N-Body simulation BUZZARD v2.0 was made recently in Elvin-Poole et al. [52]. This effect is not considered in the DES-Y1 analysis.

Non-local effects in galaxy-galaxy lensing: For year 3 specifically, we use the marginalization approach developed in MacCrann et al. [53] to address the effect of lens mass on $\langle\delta_g\kappa\rangle$, where the data covariance is modified. The effect of lens mass is non-local; namely, it will propagate from small scale to large scale. A less stringent scale cut is thus required with this marginalization method. We use an informative prior of the point-mass parameter $B_i \in \mathcal{U}(-5, 5)$. Such systematics is not considered in DES-Y1, where different scale cuts are used.

2.2 Cosmic Microwave Background

2.2.1 A Very Brief Introduction to CMB

Regarding the focus of this thesis, we would not discuss the details of CMB physics, despite it being the most powerful tool in cosmology in terms of constraining power so far. However, we would try to provide some good references for beginners, discuss why we choose primary CMB as a supplement for LSS

study, and discuss CMB lensing in more detail in Sec 2.2.2.

Ref. [54] gives a good overall introduction to CMB physics. It also includes nice figures explaining different effects to the temperature anisotropy (SW + Doppler + ISW). The physics of recombination is more complicated and can be found in [55]. We outline the basic perturbation equations in Sec. 4.2. The Boltzmann equation with the collision term thus lies the physical foundations of recombination theory. If the theory itself is easy enough, the coding should change your idea, especially the line-of-sight integral, which is a key question in cosmology last century. There are also different approximation schemes under this calculation, and either of the two Boltzmann codes CAMB or CLASS requires a lot of effort to understand. We thus omit the discussions here in this thesis.

The state-of-the-art CMB likelihood, Planck 2018 is a powerful tool. However, two things need to be noted. First, it has two slight internal inconsistencies; one related to low-ℓ TT and another related to the lensing suppression of the TT power spectrum. Specifically, the suppression characterized by A_L is smaller than expected from the reconstructed lensing likelihood from the four-point function. Second, it shows inconsistency with the more recent ACT data, especially when early dark energy is present.

For the purpose of our study, we use low-ℓ EE polarization data ($\ell < 30$) in combination with the high-ℓ TTTEEE spectra truncated right after the first peak ($35 < \ell < 396$) as our primary CMB (CMBP). This choice removes late-time Integrated Sachs Wolfe information and also removes CMB lensing effects (by the truncation at $\ell = 396$). This choice is not conventional as most of the extension studies try to gain more constraining power by including more acoustic peaks. We show in [49] that it does not have tension with other priors, but still provides enough information, especially that related to inflation.

2.2.2 CMB Lensing and Cross-Correlations with Galaxy Weak Lensing

Similar to the shear field inferred by galaxy image distortion, we could similarly use the distortion of CMB and study its cross-correlation with galaxy shear. CMB lensing provides extra information mainly due to the different window function, which peaks around z 2 and ranges to z 10. This reflects that the source of CMB (photons from the last-scattering surface) is much further from us, which gives roughly $z = 2$ as the mid-point in the comoving distance.

In the work under preparation, we adopt a similar lensing likelihood modeling to the one used in [56]. We use the CMB lensing band-power $C_{L_b}^{\kappa_{\rm CMB}\kappa_{\rm CMB}}$ estimated using the minimum-variance estimator on the reference lensing con-

vergence reconstruction map in Planck Collaboration et al. [56]. Here L_b is the weighted L mode in the angular multipole L bins. The likelihood data (data vector, binning function and its correction, linear correction, covariance matrix, binning definition) can be downloaded from https://pla.esac.esa.int. The model vector prediction of $C_{L_b}^{\kappa_{\rm CMB}\kappa_{\rm CMB}}$ is evaluated as:

$$C_{L_b}^{\kappa_{\rm CMB}\kappa_{\rm CMB}} = \sum_L \mathcal{B}_i^L C_L^{\kappa_{\rm CMB}\kappa_{\rm CMB},{\rm th}}, \tag{2.47}$$

where $\mathcal{B}_i^L$ is the binning matrix for optimal band-power estimates provided by [56]. $C_L^{\kappa_{\rm CMB}\kappa_{\rm CMB},{\rm th}}$ is the theoretical expectation of the the quadratic estimator $\hat{C}_L^{\kappa_{\rm CMB}\kappa_{\rm CMB}}$, which is a biased estimation of $C_L^{\kappa_{\rm CMB}\kappa_{\rm CMB}}$. The bias is generally complicated to evaluate and is cosmology-dependent. We follow the method in [56] to linearize the bias and marginalize it over cosmological parameters. The actual recipe used to calculate the model vector is:

$$\begin{aligned} C_{L_b}^{\kappa_{\rm CMB}\kappa_{\rm CMB}} =& \sum_L \frac{L^2(L+1)^2}{4} \mathcal{B}_i^L \bar{C}_L^{\phi\phi,{\rm th}} \\ \approx& \sum_L \frac{L^2(L+1)^2}{4} \Big[\Big(\mathcal{B}_i^L + M_i^{\phi,L} \Big) \, C_L^{\phi\phi}\Big|_\theta \\ & - M_i^{\phi,L} \, C_L^{\phi\phi}\Big|_{\rm fid} + M_i^{X,\ell} \left(\hat{C}_\ell^X - C_\ell^X|_{\rm fid} \right) \Big], \end{aligned} \tag{2.48}$$

where $C_L^{\phi\phi}\Big|_\theta$, $C_L^{\phi\phi}\Big|_{\rm fid}$ are the theoretical CMB lensing potential power spectrum evaluated at cosmological parameters θ and the fiducial cosmology assumed in [56]. $M_i^{a,\ell}$ is the linear correction matrix defined in equation 31-32 in [56]. $\hat{C}_\ell^X$ and $C_\ell^X\Big|_{\rm fid}$ are primary CMB power spectra estimated values and predictions at the [56] fiducial cosmology. X here is summed over the eight lensing estimators (TT, EE, TE, TB, EB, ET, BT, and BE).

The only dependence on cosmology in equation 2.48 is coming from

$$C_L^{\kappa_{\rm CMB}\kappa_{\rm CMB}}|_\theta = \frac{L^2(L+1)^2}{4} \, C_L^{\phi\phi}\Big|_\theta \tag{2.49}$$

which is calculated as equation (2.23) but with weighting function

$$q_{\kappa_{\rm CMB}}(\chi) = \frac{3H_0^2\Omega_m}{2c^2} \frac{\chi}{a(\chi)} \frac{\chi_* - \chi}{\chi_*}, \tag{2.50}$$

where χ_* is the comoving distance to the last scattering surface. All the other terms are pre-computed at the fiducial cosmology or evaluated from data. The

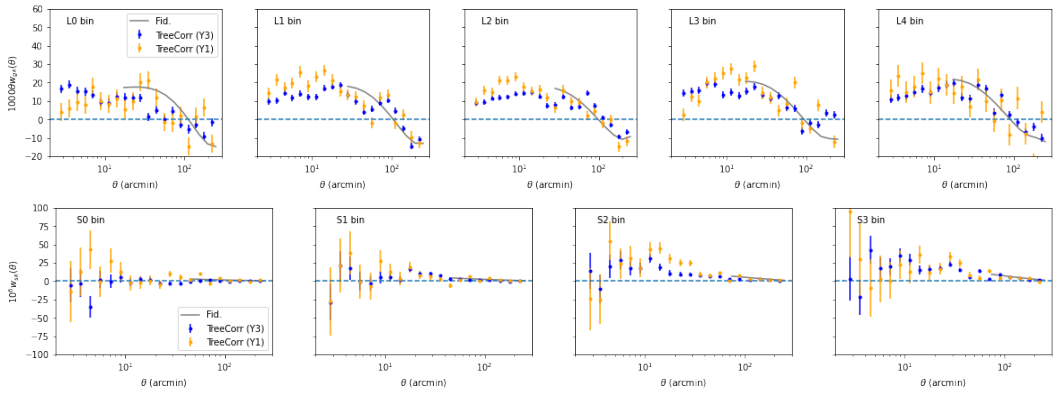


Figure 2.3: *Upper*: Glaxy position cross CMB lensing power spectrum. *Lower*: Glaxy shear cross CMB lensing power spectrum.

covariance matrix is estimated from FFP10 simulations(an updated version of FFP8 as detailed in Planck Collaboration et al. [57]) and with the Hartlap factor considered [58].

The measurement from the catalog is not trivial, given the footprint boundaries of DES-Y3 and Planck is very close in some regions. Figure 2.3 shows an example of this measurement. Cross-correlations with SPT and ACT have also been made by the collaboration [48].

2.3 BAO, SNIa, and BBN

Baryon Acoustic Oscillation (BAO) and Supernovae type Ia (SNIa) are both clean channels to measure the evolution of the geometry of the universe. They are called standard rulers and standard candles respectively. Since they are not the focus of this thesis, we refer the readers to other articles for further details. Both BAO and SNIa do not contain information about the baryon density Ω_b, and we introduce the astrophysical probe of Big Bang Nucleosynthesis to accommodate this missing information.

2.3.1 Baryon Accoustic Oscillation

Baryon Acoustic Oscillation is the imprint on matter distribution of the scale set of the sound horizon at radiation drag time. The sound horizon $r_{\rm drag}$ at baryon drag is a standard ruler that we can measure from the clustering of galaxies (the 2PCF is enhanced by 10% at the scale of $100h^{-1}$ Mpc). Fig.1 of Ref [59] provides a good illustration of how BAO feature forms. The line of sight direction and its transverse direction BAO feature constrains two

parameter combinations separately: $H(z)r_{\rm drag}$ and $D_M(z)/r_{\rm drag}$ where $D_M(z)$ is the comoving angular diameter distance. For a review of BAO theory and measurement, see Ref [60].

Although the BAO feature is measured from structure growth, it is in fact a distance relation measurement as the calculation doesn't assume any perturbation theory. In practice, the BAO constraints come from the comparison between the observed scale of BAO feature and the sound horizon $r_{\rm drag}$. Thus, as a distance measurement of the late universe, we consider BAO as pure geometry information. The BAO data set we use in Chapter 3 includes SDSS DR7 main galaxy sample [61] and the 6dF galaxy survey [62] at $z_{\rm eff} = 0.15$ and $z_{\rm eff} = 0.106$ respectively, and the SDSS BOSS DR12 optimally combined LOWZ and CMASS galaxy samples at $z = 0.38, 0.51, 0.61$ [63].

2.3.2 Supernovae Type Ia

Type Ia Supernovae (SNIa) are the most important probe of the local expansion rate. As a "standard candle", each SNIa gives an independent measurement of the magnitude-redshift relation. The apparent magnitude of a supernova is $m_{\rm th}(z) = 5\log_{10}\left(H_0 D_L(z)\right) + \mathcal{M}$, where $\mathcal{M}$ is a nuisance parameter account for the unknown absolute magnitude of the supernova. Thus, by marginalizing $\mathcal{M}$, SNIa luminosity measurement constrains the luminosity distance $D_L(z)$. As they don't involve any knowledge of the large-scale structure, we refer to them as geometry information. In Ref [49], we use the Patheon samples[64], which is a combination of Pan-STARRS1 MDS and other surveys, resulting in a total of 1048 SN Ia ranging from $0.01 < z < 2.3$. Note that an updated version of the new PHANTEON+ sample [65] is available, which includes SNIa observed with the DES survey.

2.3.3 Big Bang Nucleosynthesis

BIG Bang Nucleosynthesis, or BBN, is one of the most successful predictions of particle physics to the early universe. With the nuclear reaction rate measured on earth, the theory predicts the helium mass fraction of the universe to be about 25%. This prediction, together with that of deuterium, agrees with astrophysical measurement to very high precision. Although the ^{7}Li measurement is in a discrepancy of the current measurement [66], it does not affect the tremendous success of this theory that describes the universe as early as just a minute after the big bang. The precise measurement from astrophysics in turn allows us to constrain cosmological parameters. It also suggests that model constructors of the early universe do better not violates some basic assumptions of the BBN, such as at that early time the universe should be dominated

by radiation rather than some scalar field.

The detailed calculation involving deuterium and lithium requires some extra work, but the essence is the same as calculating the Helium abundance. We shall give a brief introduction to this calculation largely following the notes [2], and discuss one of the first measurement [67]. A more detailed calculation can be found at [25].

Protons and neutrons are in equilibrium when $T \gg$ MeV through interactions $\nu_e + n \leftrightarrow p + e^-$ and $e^+ + n \leftrightarrow p + \bar{\nu}_e$. At this time neutron decay can be ignored because of the neutron lifetime $\tau_n \simeq 15$ min. Since at chemical equilibrium $\mu_n + \mu_\nu = \mu_p + \mu_e$, the neutron-proton ratio can be written as:

$$\frac{n_n}{n_p} = \exp\left[-(m_n - m_p)/T + (\mu_e - \mu_\nu)/T\right] \tag{2.51}$$

Since at equilibrium $\mu_e/T \sim (n_{e^-} - n_{e^+})/n_\gamma = n_p/n_\gamma \sim \eta \ll 1$, the ratio at equilibrium is:

$$\left(\frac{n}{p}\right)_{\rm eq} = e^{-(m_n - m_p)/T} \tag{2.52}$$

The free-out temperature can be numerically shown to be T 0.8MeV (similar to the calculation of the freeze-out temperature of other relics). The freeze-out ratio is thus $\exp(-1.293/0.8) \approx 1/6$. Taking the neutron decay into account, this ratio is reduced to 1/7. Then the majority of the neutrons end up in ^{4}He, with the abundance:

$$X_4 = \frac{4n_H}{n_N} = \frac{4\,(n_n/2)}{n_n + n_p} = \frac{2(n/p)}{1 + (n/p)} \simeq 0.25 \tag{2.53}$$

A more detailed calculation shows this relation as a function of the baryon density Ω_b. The QSO light absorbed by the neutral hydrogen system provides a measurement of the deuterium since at a redshift as high as $z \approx 3$ almost no astrophysical process can change the deuterium abundance. As shown in Ref. [67], the steep decline of the $D(\gamma)$ function transfers a large error bar in D/H measurement to a relatively small error to Ω_b. A recent measurement gives [68]:

$$100\Omega_{\rm B}h^2 = 2.156 \pm 0.020 \tag{2.54}$$

[2] Week 3: Thermal History of the Universe

2.4 Discussion

There are other interesting probes that provide additional cosmological information at different redshifts and scales. For example, galaxy clusters, as the largest virialized system in the universe, is another channel of probing structure growth. Cluster number counts, or the one-point function, is very sensitive to late-time evolution history, but their systematics is also very hard to describe.

A lot of other interesting probes are beyond the scope of this thesis. There are probes that have been studied for decades, such as Lyman-α forest, ISM, and strong lensing system. As new technology arises, telescopes such as JWST can go much deeper than we used to do. In fact, at present time, JWST observed more giant galaxies with high redshifts than ΛCDM predicts, which could indicate another tension in cosmology, or some calibration issue with our most expensive toy ever built.

The near future of cosmology is indeed exciting, as a lot of new surveys are expected to take new data. LSST, DESI, Roman telescope, SPHEREx, and 21cm surveys, are all opening new channels for us to study the history of the universe. Apart from weak lensing, there are a lot of other interesting and important quantities to study, such as primordial non-gaussianity. New analytic tools are also emerging, for example, field-level inference and perturbation theory beyond first order (EFT and Hybrid-PT). All these questions are challenging but rewarding to explore.

The assumption of cold dark matter that this thesis trying not to violate, is also being challenged by multiple experiments. We still do not find any evidence about WIMP, we do not have a good description of axions, and yet we find interesting things like the Galactic Center GeV Excess (GCE). Tabletop experiment trying to detect dark matter beyond the WIMP region is thriving, and a lot of people are trying to bring the discussion of dark matter to the surveys that were originally built for dark energy.

I often regard the study of cosmology as an ant trying to figure out the structure of the earth. Right now we are pretty sure that the earth is composed of 70% of ocean and 30% of land. It is already quite an achievement for species that could not move beyond their very own territory. But where is the ocean coming from, and what do other places in the land look like, all these questions we are trying to answer are what makes the ant's life a little bit more interesting than the others.

Chapter 3

Growth-Geometry Split as a Model Independent Test

In this work, we use parameter splitting of $\Omega_{\rm m}^{\rm growth}$ and w to test the consistency between the background evolution and structure growth. In the standard model of ΛCDM, we have the same matter density that controls both how fast the universe expands and how fast the large-scale structure in the late universe forms. By using different data sets that contain either geometry or growth information, we can check the consistency inside ΛCDM and wCDM model, or more generally the smooth dark energy paradigm.

3.1 Growth and Geometry of the Cosmic Evolution

In this section, we discuss how geometry predicts growth in the ΛCDM model.

In ΛCDM and most of the modifications for the standard theory, the background evolution is controlled by certain quantities, such as the energy density of matter $\Omega_{\rm m}$, and the Hubble constant H_0. The universe is largely homogeneous and isotropic, which is confirmed by various observations, and thus most of the modified models do not change it. In CDM and smooth dark energy scenarios like quintessence, the evolution of linear growth structure is independent of scale and given by

$$\frac{d^2\delta_{\rm m}}{d\ln a^2} + \left[\frac{d\ln H}{d\ln a} + 2\right]\frac{d\delta_{\rm m}}{d\ln a} - \frac{3\Omega_{\rm m}H_0^2}{2a^3H^2}\delta_{\rm m} = 0, \tag{3.1}$$

where δ is the linear perturbation of matter ($\delta_{\rm m} \equiv \delta\rho_{\rm m}/\rho_{\rm m} \ll 1$). The evolution of δ is thus governed only by $\Omega_{\rm m}$ if the background of the geometry of the

model is fixed, i.e. with fixed $H(a)$.

The matter power spectrum can be written as the product of inflation, the transfer function of $\delta_{\rm m}$, and growth function:

$$P(z,k) = \frac{2\pi^2}{k^3}\frac{4}{25}A_{\rm s}\left(\frac{k}{k_{\rm norm}}\right)^{n_{\rm s}-1}\left(\frac{k}{H_0}\right)^4 T^2(k)\left(\frac{G(z)}{\Omega_{\rm m}(1+z)}\right)^2. \qquad (3.2)$$

The growth function $G(z)$ (and what's usually called the growth factor $D(z) \equiv a \times G(z)$) can be defined as it describes the redshift evolution of the matter power spectrum. Such a definition is equivalent to:

$$\frac{\Phi(a)}{\Phi\left(a_{\rm late}\right)} \equiv \frac{D_1(a)}{a} \quad (a > a_{\rm late}\,). \qquad (3.3)$$

The Poisson equation then gives

$$\delta_{\rm m}(a) = \delta_{\rm m}(0) \times D(a). \qquad (3.4)$$

Note that this is consistent with the assumption that in the late universe, all the modes enter the horizon, and dark matter is pressureless. Since there's no pressure to smooth out the inhomogeneities, the growth of the matter power spectrum is uniform in all scales.

By Substituting Eq. 3.4 into Eq. 3.1 we have the evolution equation of growth function:

$$G'' + \left(4 + \frac{H'}{H}\right)G' + \left[3 + \frac{H'}{H} - \frac{3}{2}\Omega_{\rm m}(z)\right]G = 0, \qquad (3.5)$$

where the prime denotes the derivative with respect to $\ln a$. The initial condition is taken to be $z_{\rm ini} = 1000$ in the matter dominated era, and $G_{\rm ini} = 1$, and $G'_{\rm ini} = -\frac{3}{5}(1-w)\Omega_{\rm DE}(z_{\rm ini})$ [69].

The *Report of the Dark Energy Task Force* [70] gives a review of different geometry and growth probes. The main geometry probes are BAO and SNIa, and the main growth probes are Weak Lensing and Cluster number counts. CMB and its secondaries, as introduced in Sec. 2.2 have both geometry and growth effects.

3.2 Split Growth and Geometry

3.2.1 Analysis Choices

Parameter splitting is widely used in cosmology studies. [71] tested how baryon number density affects ionization by splitting $\Omega_{\rm b}$, and found they are consistent. In [72] the authors split $\Omega_{\rm m}$ into three parameters that represent different aspects of type Ia supernova. [73] studies Early Dark Energy with LSS data and splits the primordial amplitude $A_{\rm s}$ into one from CMB and an effective one from Effective Field Theory(EFT) of LSS, and points out that there's a discrepancy between the current data between BOSS and CMB. There are also several existing works in studying geometry and growth by splitting Ω_m and w. Our analysis is most similar to the DES-Y1 paper [74], aiming to test if the information on cosmological evolution (geometry) is inconsistent with the information from DES and other external LSS probes. The Kilo-Degree Survey(KiDS) group also performed such analysis for their data set [75]. Other groups performed a more general test using all the data available up to date, such as [76–78]. Tests [79] and forecasts [69, 80] focusing on falsifying smooth dark energy scenarios were also done with various data set combinations. Since we assume a flat universe, tests of matter density are equivalent to the test of dark energy.

In our paper [49], we split the matter density $\Omega_{\rm m}$ and also w to test the consistency between geometry and growth. Since $P(z,k) \propto G^2(z)$, we can define the split matter power spectrum to be:

$$P^{\rm split}(k,z) = P^{\rm geo}(k,z) \times \frac{G^2_{\rm growth}(z)}{G^2_{\rm geo}(z)}, \tag{3.6}$$

such that $P^{\rm split}(k,z)$ follows $G^{\rm growth}(z)$ that is disentangled from eq 3.2[1]. It reduced to normal $P^{\rm geo}(k,z)$ if $\Omega_{\rm m}, w^{\rm growth} = \Omega_{\rm m}, w^{\rm geo}$. Models that introduce clustering of dark energy in general break this relation in a way that dark energy affects structure growth in addition to background expansion, as shown explicitly with some modified gravity model [81, 82]. Thus, the growth geometry split serves as a model-independent test of the smooth dark energy paradigm. In this work, we study the case with a constant dark energy equation of state. It can be generalized to marginalized background expansion $w(z)$ by Figure of Merit method [80, 83].

[1]There is a technical difference when we implement the split formalism into the weak lensing pipeline CosmoCov. For details, see [49]

3.2.2 Non-linearities, Neutrinos, and Comparison to Other Split Formalism

To account for non-linearities in the split power spectrum, we use the EUCLID EMULATOR[2]. We test in [49] that at power spectrum level HALOFIT and EUCLID EMULATOR are differed within 5%, and they don't affect inferring standard cosmological parameters in a DES-Y3-like survey. However, such a difference at the power spectrum level transfers as $\chi 2 \approx 20$ in an LSST-Y1-like survey. For this reason, we should either use the updated HMCODE, or EUCLID EMULATOR to account for non-linearities in the next-generation surveys. In the growth-geometry split, it is straightforward to use the emulator by replacing the parameters with growth counterparts.

Massive Neutrinos being non-relativistic today but still moving very fast will in general give a scale-dependent modification to the matter power spectrum. On small scales where the mean free path of neutrinos is large, the overdensity of cold dark matter and baryons do not retain neutrinos. On a larger scale, where neutrino don't travel far compared with cold dark matter and baryons, neutrinos do contribute to the gravitational potential. An approximation is given by [84]:

$$P(k,z) = \begin{cases} \left(\frac{G(z)}{G(0)}\right)^2 P(k,0) & \text{for } aH < k < k_{\rm nr} \\ \left(\frac{G(z)}{G(0)}\right)^{2p} P(k,0) & \text{for} \quad k \gg k_{\rm nr} \end{cases} \tag{3.7}$$

where $p \approx 1 - 3\Omega_\nu/5\Omega_{\rm m}$, and k_{nr} is the characteristic scale that neutrinos become non-relativistic:

$$k_{\rm nr} \approx 0.018 \Omega_{\rm m}^{1/2} \left(\frac{\rm m}{1{\rm eV}}\right)^{1/2} h{\rm Mpc}^{-1} \tag{3.8}$$

Ref. [85, 86] give an analytical function that also describes the scales in the transition region of 3.7.

In terms of the splitting matter power spectrum, we do not need to use the analytical equations above, since we first get the linear power spectrum from Boltzmann code CAMB, and the scale-dependent part is taken into account by numerical integration. We only need to include the factor that makes the growth function source term excluding neutrinos. So 3.5 becomes:

$$G'' + \left(4 + \frac{H'}{H}\right) G' + \left[3 + \frac{H'}{H} - \frac{3}{2}\Omega_m(z)\,(1 - f_\nu)\right] G = 0, \tag{3.9}$$

[2]https://github.com/miknab/EuclidEmulator2

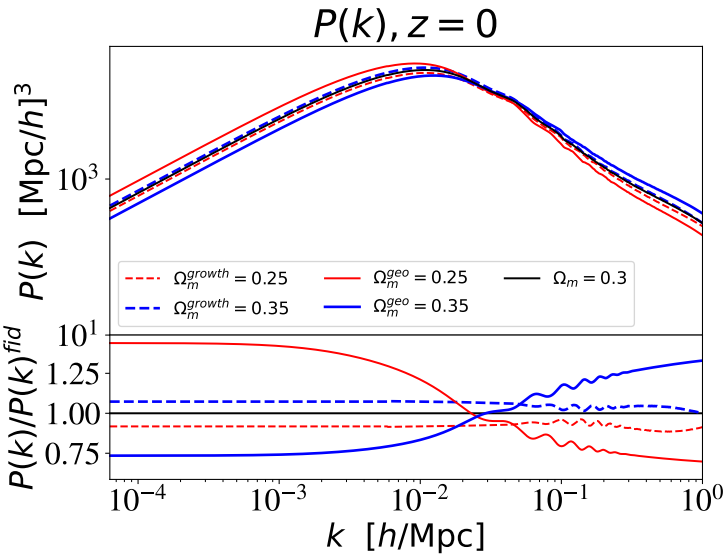


Figure 3.1: The different effects of geometry and growth parameters on power spectrum. When changing one parameter, we keep the other at the value $\Omega_{\rm m}$ at 0.3.

where $f_\nu = \dfrac{\Omega_\nu}{\Omega_{\rm m}}$, and the rest of the Hubble parameter still contains the contribution from massive neutrino, as in [86]. The same equation is also used in Boltzmann code CLASS (and CAMB) to compute the growth function.

The methodology and data set selection aim to separate geometry and growth is not unique. Apart from the growth split using similar methods we adopted in this paper, there are other approaches that target different model paradigms and redshift. For example, in [87], the authors do the splitting of CMB from the source function, so different $\Omega_{\rm m}^{\rm growth}$ would give a very different CMB power spectrum, and thus constrains the growth parameter with CMB information only. Also, they treat matter power spectrum to only depend on growth parameters, which is very different from our splitting formalism, where the shape of $P(k)$ is determined by geometry parameters. Their method is more like completely separating background geometry and standard perturbation theory, while our approach focuses more on the late time structure evolution. The method used in [88, 89] is similar to ours but uses parameter split on the growth index γ, which is a single parameter that approximately describes the growth history at low redshift.

Efforts to fully reconstruct the growth function $G(z)$ were also explored with both current data and future forecasts. In the DES-Y3 extensions to ΛCDM paper[90], one model is binned σ_8, i.e. floating σ_8 with different redshift

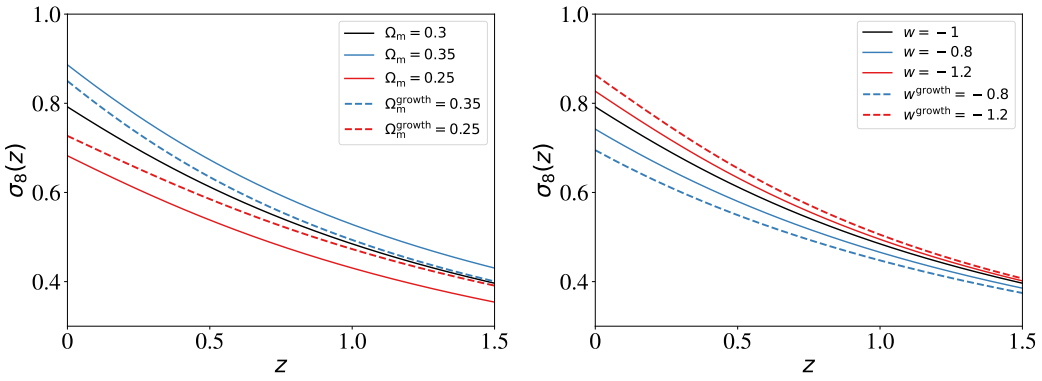


Figure 3.2: σ_8 change under the split parameter change. The solid line shows the change of growth and geometry parameter Ω_m or w simultaneously, same as in the unsplit case, whereas the dashed line is changing the growth parameter only and keeping the geometry parameter the same. It can be seen that the change of growth parameter Ω_m^{growth} results in a smaller change of $\sigma_8(z)$, whereas w^{growth} gives a larger change compared with their geometry parameter counterparts.

region, and they found a small deviation on the highest redshift bin ($z \approx 0.8$). The idea is similar in [91], but with reconstruction on the growth function $D(z)$ instead of σ_8, and a forecast on 6x2pt with CMB lensing analyze this method with synergies between the Nancy Grace Roman Space Telescope and CMB lensing data [92]. However, the constraining power of current data does not allow us to fully reconstruct the growth history of structures.

3.2.3 Effects of the Split

The result of the split matter power spectrum and consequently the σ_8 are shown in Fig. 3.1 and Fig. 3.2. The split formalism allows growth parameters Ω_m^{growth} and w^{growth} to only control the late time evolution where large scale structure evolves, namely how $P(k, z)$ evolves with z, while Ω_m^{geo} changes the matter power spectrum shape by Poisson equation:

$$k^2\Phi(k, z) = 4\pi G\delta\rho_m, \tag{3.10}$$

where Φ is the gravitational potential fluctuation. Thus the overall effect of Ω_m^{geo} is a suppression on the large scale where $P(k) \propto k$, and a boost on the smaller scale, where weak lensing mainly probes. On the other hand, the growth parameters only gives an overall scaling as to eq 3.6, until the non-linearity breaks the scale-independent relation.

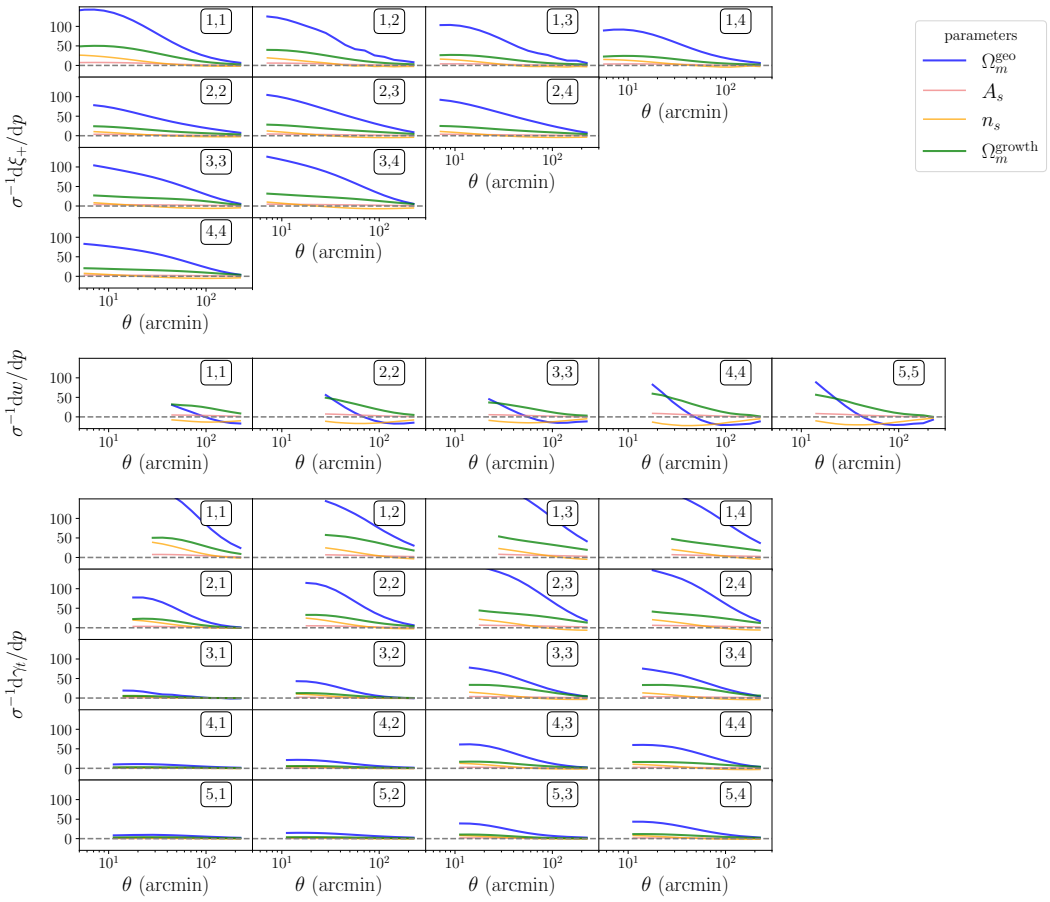


Figure 3.3: Parameter derivative of 2PCF. The derivative is taken around the fiducial value and approximated with 0.1% for all parameters. Both the data and theoretical prediction shown above are after the standard scale cut and using the Y3 modeling method.

The meta-parameter $\Omega_{\rm m}^{\rm growth}$ and $w^{\rm growth}$ affects the summary statistics (data-vector) also through the intrinsic alignment (IA) model. This choice is not unique, and in [49] we mainly follow the DES-Y1 analysis [74] and we defer the comparison of choices to future investigation.

To show the effects of growth parameters on the 2PCF of 3x2pt, we calculate the parameter derivative normalized with the variance. In fig 3.3, we plot the change of 2PCF with respect to four parameters, inflationary parameters $A_{\rm s}$, $n_{\rm s}$, and geometry and growth $\Omega_{\rm m}$. Here σ is defined to be the uncertainty of the 2PCF at the angle (i.e. the square root of the diagonalized element of the covariance matrix): $\sigma^2 \equiv \mathrm{Diag(Cov)}$.

We do not further normalize here the derivative with the standard deviation

of the parameter as in Obied et al. [93], due to the different constraining power we have from the geometry priors.

The result reflects the change in the split matter power spectrum. The change of primordial amplitude $A_{\rm s}$ gives an overall scaling, and the tilt parameter $n_{\rm s}$ has a tiny but scale-dependent effect. The change of $\Omega_{\rm m}^{\rm geo}$ dominates all 2PCF. The growth parameter $\Omega_{\rm m}^{\rm growth}$ gives similar scaling as $A_{\rm s}$ but the effects are larger, as it changes directly the growth function $G(z)$, and also controls other effects such as intrinsic alignment. The plot also shows their relative change along different redshifts, a direct reflection of fig 3.2. The difference is larger when we change $\Omega_{\rm m}^{\rm geo}$ compared with $\Omega_{\rm m}^{\rm growth}$. Also, the behavior for different redshift bins breaks the degeneracy between $A_{\rm s}$ and $\Omega_{\rm m}^{\rm growth}$, as the parameter derivative of $A_{\rm s}$ is mostly the same for each redshift bin. Similar effects also exist for cosmic shear $\xi_{\pm}$ and galaxy-galaxy lensing γ. This is where our constraining power of growth parameters comes from using DES weak lensing and clustering data.

3.3 Results with DES-Y1/Y3

In this section, we summarize the results of [49] and some future planned analyses. The baseline conclusion is we find no inconsistency between geometry and growth in cosmic shear analysis, and we attribute the tension in 2x2pt to residual systematics in the DES-Y3 REDMAGIC galaxy sample rather than to new physics. For a detailed discussion of the full results, see [49].

3.3.1 Baseline Results

LCDM Results

As the main probe target for most of the current and future LSS surveys, the 3x2pt is expected to give the most constraining power on the growth history of the universe, as we show in the noiseless synthetic data vector [49]. As shown in the left panel of fig 3.4, we find geometry and growth are consistent in both Y1 and Y3 3x2pt data.

However, we notice some preference of lower $\Omega_{\rm m}$ in different combinations of 2PCF for Y3 data specifically. As shown in the right panel of fig 3.4, except cosmic shear + galaxy-galaxy lensing, other 2PCF combinations along with cosmic shear only give a trend that $\Omega_{\rm m}^{\rm growth} < \Omega_{\rm m}^{\rm geo}$. In the case of $w(\theta) + \gamma_t$ (2x2pt), we find a slight tension that $\Delta\Omega_{\rm m} < 0$. The result is, however, consistent in the Y3KP that REDMAGIC lens samples 2x2pt gives a smaller S_8, as shown in figure 11 of Abbott et al. [6].

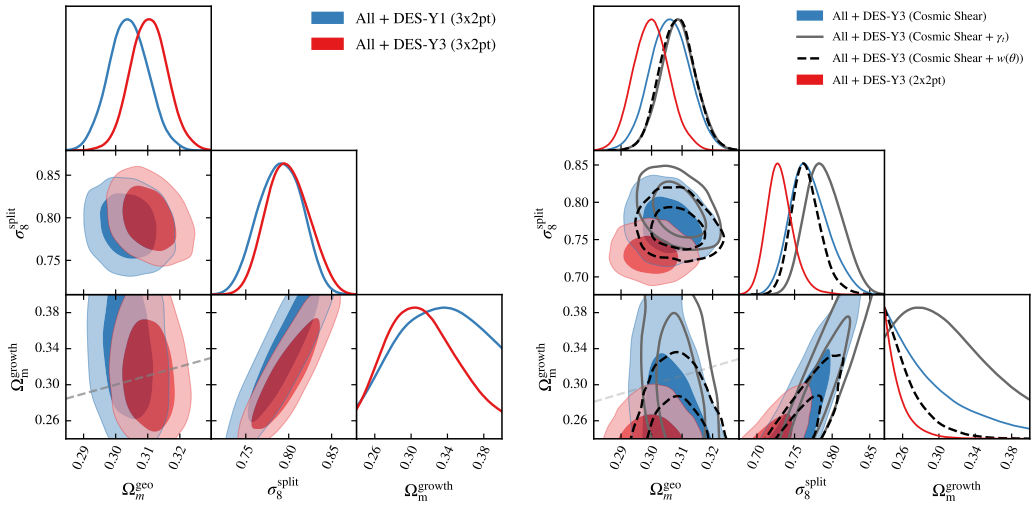


Figure 3.4: Cosmological constraints on split ΛCDM. On the left is 3x2pt with Y1 and Y3 data, and on the right is Y3 data with different combinations of 2PCF and cosmic shear only. The dashed grey line on each plot corresponds to $\Omega_{\rm m}^{\rm growth} = \Omega_{\rm m}^{\rm geo}$.

The combination of different priors on geometry information provides us with information to break the degeneracy between constraints on growth information and the primordial power spectrum. As can be seen in most dashed and dotted lines in figure 11 of [49], CMB gives a prior on the primordial parameter $A_{\rm s}$ and $n_{\rm s}$, while BAO+SN+BBN give priors on $\Omega_{\rm m}^{\rm geo}$. In most cases, the 2 sets of priors are consistent. For example, DES+BAO+SN+BBN gives a large posterior on $A_{\rm s}$ and $n_{\rm s}$, allowing most of the information on these two parameters to come from CMB. The only exception is Y3 2x2pt, where DES+BAO+SN+BBN itself already gives a tight constraint on $A_{\rm s}$ and the value is not in agreement with that given by CMB prior. This could be related to the fact that Y3 2x2pt itself prefers a lower growth today, since the same likelihood with CMB prior that gives a higher $A_{\rm s}$ still prefers a lower $\sigma_8^{\rm split}$ and $\omega_{\rm m}^{\rm growth}$. On the other hand, the Y1 counterpart does not show the same trend, and the 2x2pt combinations are more consistent with each other.

wCDM Results

The degeneracy between $w^{\rm growth}$ and $\Omega_{\rm m}^{\rm growth}$ can be seen from eq 3.5, or from fig 3.2. In fact, most all of the previous studies on the growth geometry split literature finds no constraining power in the $w^{\rm growth}$ itself. We quantify this

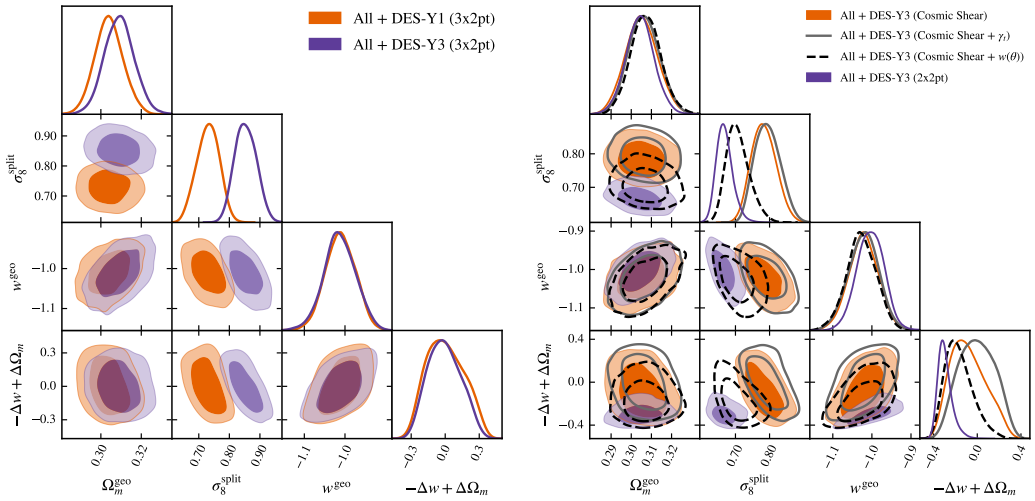


Figure 3.5: The cosmological constraints on wCDM. We also show the combination of the difference between growth and geometry, i.e. $\Delta w \equiv w^{\rm growth} - w^{\rm geo}$ and $\Delta\Omega_{\rm m} \equiv \Omega_{\rm m}^{\rm growth} - \Omega_{\rm m}^{\rm geo}$

degeneracy with principal component analysis (PCA). PCA is commonly used in data science to reduce the dimension of parameter space and to find the best-constrained parameter combination. Based on our synthetic DES data chains, we create a principal component and find the following combination of $\Delta w \equiv w^{\rm growth} - w^{\rm geo}$ and $\Delta\Omega_{\rm m} \equiv \Omega_{\rm m}^{\rm growth} - \Omega_{\rm m}^{\rm geo}$ is best constrained in our growth split formalism:

$$\mathrm{PC1} = -0.7071\Delta w + 0.7071\Delta\Omega_{\rm m}. \tag{3.11}$$

The results are as expected since, intuitively, more matter or less dark energy(dark energy being more phantom) produces more structure, and this result confirms that the two parameters are positively correlated with the same weights. Since the weight on the two parameters is the same, we just show the combination $-\Delta w + \Delta\Omega_{\rm m}$ in figure 13 of [49].

3.3.2 Tensions

To evaluate the tension, we use the parameter difference method [94, 95]. Given two chains θ_1 and θ_2 and their corresponding posteriors $\mathcal{P}_1(\theta_1)$ and $\mathcal{P}_2(\theta_2)$ and begin by computing the difference between these two chains, denoted with $\Delta\theta = \theta_1 - \theta_2$. Using this difference chain we can write $\mathcal{P}_2(\theta_2) = \mathcal{P}_2(\theta_1 - \Delta\theta)$. By marginalizing over θ_1, we get the parameter difference pos-

terior

$$\mathcal{P}(\Delta\theta) = \int_{V_\Pi} \mathcal{P}_1(\theta_1)\mathcal{P}_2(\theta_1 - \Delta\theta)d\theta_1, \tag{3.12}$$

where V_Π is the subset of the domain covered by the prior. As $\theta_1 \to \theta_2$, the means $\mu_1 \to \mu_2$ thus $\mu \to 0$. Thus the volume of the regions with $\mathcal{P}(\Delta\theta) > \mathcal{P}(0)$ approaches 0. We can approximate the tension using

$$\Delta = \int_{\mathcal{P}(\Delta\theta)>\mathcal{P}(0)} \mathcal{P}(\Delta\theta)d\Delta\theta. \tag{3.13}$$

This volume is interpreted as a probability of parameter shift, denoted Δ. If Δ comes from a Gaussian distribution, the number of standard deviations from 0 is given by

$$n_\sigma = \sqrt{2}\text{Erf}^{-1}(\Delta) \tag{3.14}$$

To estimate the posterior, we use Masked Autoregressive Flows (MAFs) [94, 96]. The flow is generated by a series of Masked Autoencoders for Density Estimation (MADEs). Each made receives a masked input

$$x_{1:i-1} = (x_1, \ldots, x_{i-1}, 0, \ldots, 0) \tag{3.15}$$

and the resulting point is given by

$$y_i = T(x_{1:i-1}) + S(x_{1:i-1})x_i \tag{3.16}$$

where T and S are invertible functions parameterized by neural networks. The loss function is the negative log probability of y from a Gaussian. Due to the autoregressive property, the Jacobian is triangular and thus the determinant is tractable to compute even for a large number of dimensions. Thus we can estimate the posterior as a reparameterization of a Gaussian and thus find the log probablity of arbitrary points.

Before training the neural network, we follow the implementation in [94] to apply a linear transformation to $\Delta\theta$ given from the Gaussian approximation for $\mathcal{P}(\Delta\theta)$

$$\Delta\theta' = C^{-1}(\Delta\theta - \mu) \tag{3.17}$$

with C the covariance and μ the mean of $\mathcal{P}(\Delta\theta)$. This enhances the convergence rate of the gradient descent in the neural networks.

To compute the integral in eq. 3.13 we use Monte Carlo integration. Using the MAF we randomly sample from the posterior and calculate the log probability. The fraction of generated points that land in the region $\mathcal{P}(\Delta\theta) > \mathcal{P}(0)$

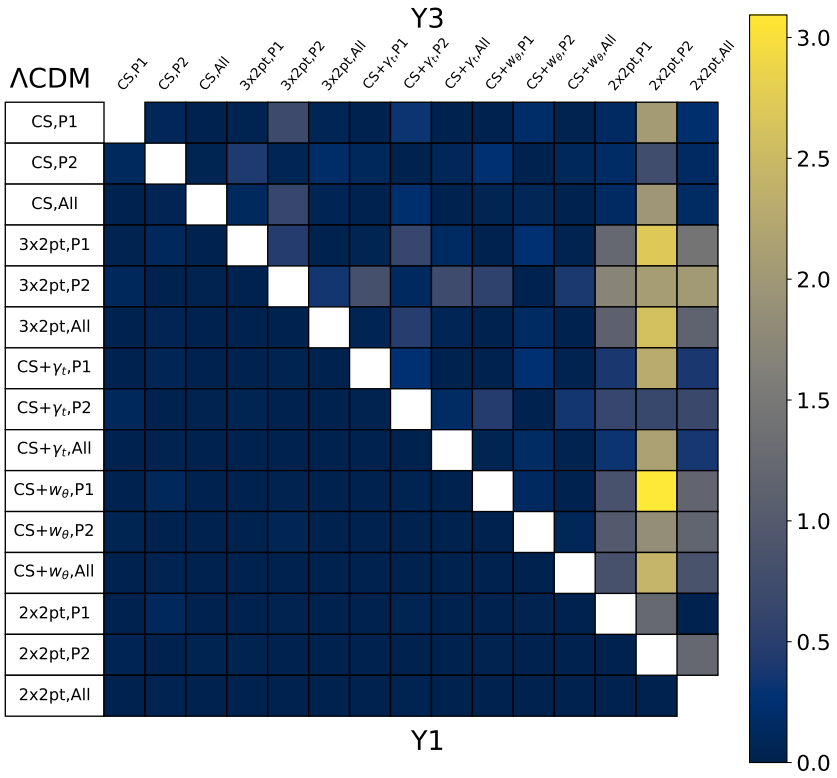


Figure 3.6: Internal Tension of split LCDM cosmology under DES-Y1/Y3 with different geometry priors.

are counted. The estimate of the error is given by the Clopper-Pearson interval for a binomial distribution.

The reported tension n_σ is summarized in Fig 3.6. As can be seen from the color bar, only the Y3 2x2pt with BAO+SNIa+BBN prior is in tension with other data set combinations.

3.4 Discussion

In a work under preparation, we investigate the limit of this growth geometry splitting formalism with an LSST-Y1-like survey. We forecast the difference in constraining power between cosmic shear and 3x2pt. We also show the mapping between a generalized $w(z)$ function and the meta-parameter split of Ω_m and $\Omega_m + w$. The key question we are trying to answer is as follows: the formalism is designed to test any breakdown between geometry-growth relation (or the breakdown of GR and smooth dark energy), but such a split

is performed only under a constant equation of state. Would this split give Geometry $\neq$ Growth if the cosmology has a very general equation of state? As we would show, if the DE EoS follows $w_0 - w_a$, such formalism picks up inconsistency only if the dark energy model is non-smooth (e.g. anisotropic stress). However, if the background evolution is generalized to binned w, the formalism fails to tell if Geometry $\neq$ Growth is from the change of the background or other physics.

That question aside, there are still some interesting points that we would like to study with current DES-Y3 data in the near future. We summarize some of the possibilities below:

Priors and external data: we have demonstrated the importance of restricting the primordial power spectrum parameters with external CMB data. Expanding the allowed range on the CMB temperature and polarization power spectra without adding CMB lensing information that constrains growth parameters will demand either the implementation of either delensing techniques [97, 98] or marginalization over lensing principal component parameters [99]. Of course, we won't need these calculations when combining DES-Y3 3x2pt with CMB lensing in the so-called 6x2pt multi-probe analysis. The wCDM split would also benefit from extra information on $w^{\rm geo}$ from the observed DES Type IA supernova included in the new PHANTEON+ sample [65]. DES-Y3 constraints on growth parameters in wCDM split are severely prior limited; overcoming that will also require additional information on large-scale structure evolution. We also plan to implement the growth-geometry split in the galaxy two-point functions in the SDSS BOSS survey via Lagrangian perturbation theory [100].

Small scales: we have adopted standard DES-Y1 and DES-Y3 scale cuts in this analysis, following the DES collaboration leading papers; however, DES has once explored methods to add small-scale data in both Cosmic Shear and 2x2pt two-point correlation functions [40, 101]. The infrastructure for such an increase in the number of data points adopted in a growth-geometry study is present in COSMOLIKE. Current quadratic bias can model the 2x2pt data vector up to $k_{\rm max} \approx 0.3$ h/Mpc, and newly developed hybrid effect field theory approaches could expand the range of applicability even more to $k_{\rm max} \approx 0.7$ h/Mpc [102]. We first plan to expand 2x2pt towards smaller scales using Halo Occupation Distribution [39, 103, 104].

Lens galaxy samples: the highest priority follow-up study involves an in-depth comparison between REDMAGIC and MAGLIM lensing galaxy samples. The REDMAGIC induced behavior on the DES-Y3 2x2pt correlation function

is likely responsible for the observed shifts in the growth parameters towards $\Delta\Omega_{\rm m} \neq 0$ in ΛCDM and $\Delta\Omega_{\rm m} - \Delta w \neq 0$ in wCDM splits. The cross-correlation between 2x2pt and cosmic shear considerably minimizes these shifts, which justified our choice of fixing $X_{\rm lens} = 1$. However, the question of how the split parameters correlate with $X_{\rm lens}$ is unanswered. We also plan to add one $X_{\rm lens}$ per redshift bin and include the highest MagLim bins 5 and 6 not incorporated in the DES fiducial analysis. Finally, there have been recent a-posteriori, data-driven changes to RedMagic lens sample. We plan to investigate how post-blinding changes in the DES-Y3 pipeline and data products affect the split parameters [40].

Additional cross-correlations: we plan to combine DES-Y1 and KiDS-1000 cosmic shear data to improve its constraints. This is an important cross-check against DES-Y3 as the RedMagic lens sample seems better behaved on DES-Y1 [105, 106]. The absence of overlapping sky between KiDS-1000 and DES-Y1 greatly simplifies the analysis, dispensing the need for cross-covariances. We intend to employ the cross-correlation between DES-Y1 and DES-Y3 3x2pt against Planck and ACT lensing data. We also plan to add in the DES-Y1 cross-correlation between cluster positions and galaxy shapes and positions. We also plan to add the cluster position autocorrelation and number counts. The DES collaboration already studied the introduction of these 2PCF using CosmoLike infrastructure [107].

These improvements are part of an ambitious research effort involving constraining the growth geometry split parameters with state-of-the-art weak lensing and galaxy clustering data. They are also the backbone infrastructure work for the final DES-Y6 release, emphasizing theories that have not been assessed in DES-Y3 analysis on extended cosmological models [90]. The Cobaya-Cosmolike Architecture contains several adaptations that solved critical problems that halted past DES progress in constraining many-parameter extensions to ΛCDM, the need for faster pipelines without losing modeling generality being the primary one.

The many single and multi-core optimizations we implemented in CosmoLike allowed us to study the growth-geometry split without employing the Multinest [108] and Polychord [109] nested sampling methods that require hundreds of CPU cores to provide results in a reasonable time. We explored multiple external data set combinations and redid the DES-Y1 official analysis [74] with several improvements, including adopting the latest Planck 2018 CMB data, the non-limber calculation on large-scale galaxy clustering and the full-sky computation of the two-point real 3x2pt correlation functions. There

is still much work to be done in probing exotic models with the current generation of observatories. This manuscript is a step towards a comprehensive beyond ΛCDM research that fully employs the information available in the DES-Y1 and DES-Y3 data.

Chapter 4

Models of Dark Energy I: Fluids

4.1 Problems of ΛCDM

The standard ΛCDM model describes the current data extremely well. The model uses the cosmological constant Λ to account for the current accelerating expansion of the Universe. However, there are two "problems" with the cosmological constant explanation:

- Fine-tuning [13]: we do not have an explanation of why the cosmological constant is such small.
- Coincidence problem: the initial condition for what we observed today is extremely constrained. Why the dark energy and dark matter energy density is so similar today? This question is not natural without an anthropic argument [110].

To see the fine-tuning problem, let us do some crude estimation. The order of the energy density as observed today is:

$$\rho_\Lambda \approx \frac{\Lambda m_{\rm pl}^2}{8\pi} \approx \frac{H_0^2 m_{\rm pl}^2}{8\pi} \approx 10^{-47}{\rm GeV}^4 \approx 10^{-123} m_{\rm pl}^4, \tag{4.1}$$

However, the typical vacuum energy of a field theory of mass m valid up to a cut-off scale $k_{\rm max} \gg m$ is

$$\rho_{\rm vac} = \int_0^{k_{\rm max}} \frac{4\pi k^2 \, {\rm d}k}{(2\pi)^3} \frac{1}{2} \sqrt{k^2 + m^2} \approx \frac{k_{\rm max}^4}{16\pi^2}. \tag{4.2}$$

If the cut-off scale is Planck scale $m_{\rm pl}$, then:

$$\rho_{\rm vac} \simeq 10^{74}{\rm GeV}^4, \tag{4.3}$$

which is 121 orders of magnitude larger than the observed value! Remind the readers that the hierarchy problem in the particle physics community often refers to the question of why electro-weak force is 10^{24} times stronger than gravity. A problem of even 100 orders more severe sounds a bit hopeless.

Both problems can only be partially solved by including the dynamics of the "Dark Energy" component. For example, in the tracker quintessence model, an attractor causes the energy density to track the equation of state (EoS) so that the evolution is insensitive to the initial energy density. However, it does require fine-tuning to make sure the dark energy component overtakes the matter component at the present time [111].

The quintessence model is very interesting in the sense that there are various kinds of potentials (freezing, thawing) motivated by particle physics. Some of them can solve the problem in the ΛCDM model and provide guidance for future observation.

However, the EoS of quintessence cannot go cross -1. It would be interesting to study the case where the EoS can be smaller than -1. Although this would violate the weak energy condition, a stable model is not impossible to construct [112]. It is also important to study this case because the data now actually favors $w < -1$. In fact, the parameter fitting from Planck 2013 data favors a less than -1 value of w, but the new 2018 result does not. On the other hand, the SNIa data do favor a smaller value of Ω_m in ΛCDM model, and this tension can be relieved by faster fall away than the cosmological constant, i.e., $w < -1$.

In any case, we should keep an open mind to studying dark energy models beyond vacuum energy.

4.2 Eulerian Perturbation Theory

In this section, we briefly introduce the Eulerian Perturbation Theory, the cornerstone of modern cosmology. We only discuss the basics of metric perturbation, Boltzmann equation/fluid equations, and the simple case of cold dark matter. For a nice review, see [55]. We do not discuss the interesting behaviors of photons and recombination. Although in the time of 2020s two Boltzmann codes CAMB [113, 114] and CLASS [115] largely do the hard work for us, it would still be beneficial to understand some intuitive relations between perturbation theory predictions to the observables like CMB. See [54] for a review.

Most of these discussions, including this section, focus on two gauges: Synchronous gauge, and Newtonian gauge. The synchronous gauge is favored in the Boltzmann code due to its numerical stability (it would not require a large

number divided by a tiny number). The Newtonian gauge, on the other hand, does not have off-diagonal terms and could be easier when working with extension models. Transforming back and forth between two gauges while focusing on gauge-invariant terms is extremely useful. A general gauge transformation and other non-standard assumptions can also be very useful for extension models. The PPF formalism discussed in Sec. 4.3.1, for example, relies on another gauge. For a more in-depth review, see [116]. The lecture notes by Wayne Hu [1] are also good resources for both introduction and more advanced explanation.

4.2.1 Metric Perturbation

A perturbative FLRW metric is:

$$ds^2 = a^2(\tau)\left\{-(1+2A)d\tau^2 - 2B_i d\tau dx^i + \left[(1-2D)\delta_{ij} + 2E_{ij}\right] dx^i dx^j\right\} \quad (4.4)$$

where the space-space component is separated into trace part D and the traceless component E_{ij}.

The total degree of freedom is 1+3+1+5 = 10. But four of them correspond to the choice of (τ, x^i) is arbitrary. Thus, one can remove four degrees of freedom by specifying some of the quantities to be zero. The procedure is called gauge choice, exactly like the case in Electrodynamics. Below we introduce two commonly used gauges.

The conformal Newtonian gauge (longitudinal gauge), or simply Newtonian gauge, is chosen such that the time-space component vanished:

$$ds^2 = a^2(\tau)\left\{-(1+2\psi)d\tau^2 + (1-2\phi)dx^i dx_i\right\}, \quad (4.5)$$

where we follow the notation of [55]. Other notations might have $\psi = \Psi$ and $\phi = -\Phi$, with a minus sign on the special part. Note that the Newtonian case is restricted to the scalar mode by construction. That is why it only has 2 degrees of freedom instead of 6. The general form with vector and tensor degrees of freedom is called the Poisson gauge.

Synchronous gauge, as the name suggests, has a time slicing such that:

$$ds^2 = a^2(\tau)\left\{-d\tau^2 + \left(\delta_{ij} + h_{ij}\right) dx^i dx^j\right\} \quad (4.6)$$

where h_{ij} is a general metric perturbation that we can decompose into scalar, vector, and tensor modes. We shall only focus on the scalar modes in Fourier

[1] http://background.uchicago.edu/ whu/

space, where we define:

$$h_{ij}(\boldsymbol{x},\tau) = \int d^3k e^{i\boldsymbol{k}\cdot\boldsymbol{x}} \left\{ \hat{k}_i\hat{k}_j h(\boldsymbol{k},\tau) + \left(\hat{k}_i\hat{k}_j - \frac{1}{3}\delta_{ij}\right) 6\eta(\boldsymbol{k},\tau) \right\}, \quad \boldsymbol{k} = k\hat{k} \tag{4.7}$$

The problem with the synchronous gauge is that the initial condition hypersurface is arbitrary, which gives a residual degree of freedom. Usually, we follow an observer in the comoving frame of cold dark matter and set the initial velocity of the observable to zero.

The gauge transform follows the usual procedure, we write down the general coordinate transform and impose the invariance of the line element. We omit the detailed calculation which can be found in [55]. The result in $k-$space is:

$$\begin{aligned} \psi(\boldsymbol{k},\tau) &= \frac{1}{2k^2}\left\{ \ddot{h}(\boldsymbol{k},\tau) + 6\ddot{\eta}(\boldsymbol{k},\tau) + \frac{\dot{a}}{a}[\dot{h}(\boldsymbol{k},\tau) + 6\dot{\eta}(\boldsymbol{k},\tau)] \right\} \\ \phi(\boldsymbol{k},\tau) &= \eta(\boldsymbol{k},\tau) - \frac{1}{2k^2}\frac{\dot{a}}{a}[\dot{h}(\boldsymbol{k},\tau) + 6\dot{\eta}(\boldsymbol{k},\tau)]. \end{aligned} \tag{4.8}$$

4.2.2 Einstein Equation and Perfect Fluids

We present here the fluid equations in synchronous gauge. Firstly, after specifying the metric, the Einstein equation for each component gives:

$$\begin{aligned} k^2\eta - \frac{1}{2}\frac{\dot{a}}{a}\dot{h} &= 4\pi G a^2 \delta T^0_0(\mathrm{Syn}), \\ k^2\dot{\eta} &= 4\pi G a^2(\bar{\rho}+\bar{P})\theta(\mathrm{Syn}), \\ \ddot{h} + 2\frac{\dot{a}}{a}\dot{h} - 2k^2\eta &= -8\pi G a^2 \delta T^i_i(\mathrm{Syn}), \\ \ddot{h} + 6\ddot{\eta} + 2\frac{\dot{a}}{a}(\dot{h}+6\dot{\eta}) - 2k^2\eta &= -24\pi G a^2(\bar{\rho}+\bar{P})\sigma(\mathrm{Syn}). \end{aligned} \tag{4.9}$$

where we define the velocity dispersion and anisotropic stress (shear term of the energy-momentum tensor) as:

$$(\bar{\rho}+\bar{P})\theta \equiv ik^j\delta T^0_j, \quad (\bar{\rho}+\bar{P})\sigma \equiv -\left(\hat{k}_i\hat{k}_j - \frac{1}{3}\delta_{ij}\right)\Sigma^i_j, \tag{4.10}$$

where $T^i_j = (\bar{P}+\delta P)\delta^i_j + \Sigma^i_j$. Note that the shear term is related to Π used in section 4.3.1 with $\sigma = 2\Pi\bar{P}/3(\bar{\rho}+\bar{P})$, or:

$$\sigma = \frac{2}{3}\frac{\bar{P}\Pi}{(1+w)\bar{\rho}} \equiv \frac{2}{3}\frac{\bar{\rho}\pi}{(1+w)\bar{\rho}}, \tag{4.11}$$

where the latter π is a different definition thourgh $P\Pi = \rho\pi$ that is used in CAMB-fluid module.

For a perfect fluid, the energy-momentum tensor has the form:

$$T^{\mu}_{\nu} = Pg^{\mu}_{\nu} + (\rho + P)U^{\mu}U_{\nu}, \tag{4.12}$$

where U^{μ} is the four-velocity and the three-velocity related to $\theta = ik^{j}v_{j}$. Then the conservation equation of the perturbed part, as a result of the Einstein equation, gives the fluid equations:

$$\begin{aligned} \dot{\delta} &= -(1+w)\left(\theta + \frac{\dot{h}}{2}\right) - 3\frac{\dot{a}}{a}\left(\frac{\delta P}{\delta\rho} - w\right)\delta, \\ \dot{\theta} &= -\frac{\dot{a}}{a}(1-3w)\theta - \frac{\dot{w}}{1+w}\theta + \frac{\delta P/\delta\rho}{1+w}k^2\delta - k^2\sigma, \end{aligned} \tag{4.13}$$

where the perturbation of pressure is usually set via effective sound speed:

$$c_s^2 = \frac{\delta P}{\delta\rho}. \tag{4.14}$$

Since we did not assume any property for the fluid, being whether dust or radiation, this equation holds for all components (under the assumption of GR).

In the special case of cold dark matter, the fluid equation 4.13 for density and velocity perturbations is a closed system. In synchronous gauge where we use CDM itself to remove the residual degrees of freedom, the evolution of CDM is reduced to one single equation:

$$\dot{\delta}_c = -\frac{1}{2}\dot{h} \tag{4.15}$$

this simple solution, however, only exists because of the assumption that dark matter is cold.

4.2.3 Distribution Function and Phase Space

Let us consider a universe composed of CDM, baryon, neutrino, and photon. We have four sets of fluid equations 4.13 plus two independent Einstein equations 4.9 (since we used energy conservation to get fluid equations, only two of the four of them are independent). But since neutrino and photon have non-vanishing shear components, we have 12 parameters to solve, That is even before considering the collision terms between photon and baryon. Thus, we

need more equations to describe the system. Fortunately, we do know the distribution function at the zeroth order (Fermi-Dirac for fermion and Bose-Einstein for boson), and the Boltzmann equation provides a link of the collision terms.

The distribution function in phase space is defined such that $f(\boldsymbol{x},\boldsymbol{p})d^3xd^3p$ is the probability that there exists a particle in the infinitesimal phase space volume d^3xd^3p. For point particles, the distribution function can be written as:

$$f(\boldsymbol{x},\boldsymbol{p}) = \sum_n \delta^{(3)}\left(\boldsymbol{x}-\boldsymbol{x}_n\right)\delta^{(3)}\left(\boldsymbol{p}-ma\boldsymbol{v}_n\right) \tag{4.16}$$

For photons and neutrinos at first order

$$f_0 = f_0(\epsilon) = \frac{g_s}{h_{\rm P}^3}\frac{1}{e^{\epsilon/k_{\rm B}T_0}\pm 1} \tag{4.17}$$

where $\epsilon = a\left(p^2+m^2\right)^{1/2} = \left(P^2+a^2m^2\right)^{1/2}$, and T_0 the temperature today.

The energy-momentum tensor, in any metric and gauge specification, is defined as:

$$T_{\mu\nu} = \int dP_1dP_2dP_3(-g)^{-1/2}\frac{P_\mu P_\nu}{P^0}f\left(x^i,P_j,\tau\right) \tag{4.18}$$

and thus it integrates into the mass density, momentum density, and kinetic tensor as:

$$\begin{aligned}
\rho(\boldsymbol{x},t) &= \frac{m}{a^3}\int d^3p f(\boldsymbol{x},\boldsymbol{p}),\\
\pi^i(\boldsymbol{x},t) &= \frac{1}{a^4}\int d^3p p^i f(\boldsymbol{x},\boldsymbol{p}),\\
\sigma^{ij}(\boldsymbol{x},t) &= \frac{1}{ma^5}\int d^3p p^ip^j f(\boldsymbol{x},\boldsymbol{p}).
\end{aligned} \tag{4.19}$$

The Boltzmann equation with a collision term gives:

$$\frac{Df}{d\tau} = \frac{\partial f}{\partial\tau}+\frac{dx^i}{d\tau}\frac{\partial f}{\partial x^i}+\frac{dq}{d\tau}\frac{\partial f}{\partial q}+\frac{dn_i}{d\tau}\frac{\partial f}{\partial n_i} = \left(\frac{\partial f}{\partial\tau}\right)_C, \tag{4.20}$$

with $q_j \equiv ap_j$. The only part that we need to calculate is the $dq/d\tau$ term, which is simple in the synchronous gauge. From the geodesic equation:

$$\frac{dP^0}{d\lambda}+\Gamma^0{}_{\alpha\beta}P^\alpha P^\beta = 0. \tag{4.21}$$

we have:

$$\frac{dq}{d\tau} = -\frac{1}{2}q\dot{h}_{ij}n_in_j \tag{4.22}$$

The Boltzmann equation is thus:

$$\frac{\partial f}{\partial \tau} + i\frac{q}{\epsilon}(\boldsymbol{k}\cdot\hat{n})f + \frac{d\ln f}{d\ln q}\left[\dot{\eta} - \frac{\dot{h}+6\dot{\eta}}{2}(\hat{k}\cdot\hat{n})^2\right] = \left(\frac{\partial f}{\partial \tau}\right)_C . \tag{4.23}$$

Note that we have mixed metric perturbation and distribution function perturbation here. The $f(x,p,t)$ can be perturbed, and we can separate the zeroth order and first-order terms.

Equation 4.23 can also be derived using canonical variables, which is simpler in the Newtonian gauge. The geodesic equation is a bit more complicated due to non-zero 00 terms. We summarize the result below and kindly leave it as an exercise for the reader (for reference, see [25]):

$$\frac{\partial f}{\partial t} + \frac{\hat{p}^i}{a}\frac{\partial f}{\partial x^i} - p\frac{\partial f}{\partial p}\left[H + \frac{\partial \phi}{\partial t} - \frac{\hat{p}^i}{a}\frac{\partial \psi}{\partial x^i}\right] = \left(\frac{\partial f}{\partial \tau}\right)_C . \tag{4.24}$$

The phase space analysis is not very relevant in the context of this thesis (CDM). It is, however, very useful for photons and neutrinos (see [55]) and necessary for Effective Field Theory of Large Scale Structure (EFTofLSS) [117], or in general, any calculation going to loop order.

4.3 Dark Energy as a Non-Smooth Fluid

4.3.1 Anisotropic Stress of Dark Energy

In this section, we discuss two ways of studying late-time dark energy anisotropic stress. The first one involves PPF formalism, and the latter is a direct fluid description.

PPF Formalism and Effective Anisotropic Stress

The Post-Friedmann Framework(PPF) is often used to study dark energy perturbations when the equation of state $w = -1$ (crossing the phantom divide) [118]. In the usual framework, a fluid obeys the conservation equation:

$$u' = (3w-1)\,u + k_H\frac{\delta p}{\rho} + (1+w)\,k_H A, \tag{4.25}$$

where prime is the derivative with respect to $\ln a$, $w = \rho/p$ the equation of state, $k_H = k/aH$. A denotes the gravitational potential in any gauge, and u the velocity such that $T^0_i \equiv (\rho \mathbf{u})_i$. A divergence appears in the relative fluid

velocity $v = u/(1+w)$ when $w = -1$. More generally, $w = -1$ will result in instability of perturbation evolution [119].

While certain two-field models are possible for dark energy to go cross the phantom divide [119], the PPF formalism provides a way that keeps the microstructure as in fluid description, which enables us to study properties that vanished in the scalar field, such as anisotropic stress. As detailed in [120], a general minimal coupled dark energy model requires two closure relations: one gives anisotropic stress and another relates pressure perturbation and density of dark energy itself.

The PPF formalism replaces the second closure relation with the relation between pressure perturbation of fluid dark energy and density of matter(or all the components other than dark energy) on large scale. It is possible to do this by noticing the real degrees of freedom of dark energy is the transition scale such that well below and above this scale dark energy fluid is smooth. The small-scale perturbation is given by an effective sound speed c_Γ.

The PPF formalism is motivated by the Einstein equation:

$$\begin{aligned} k^2\Phi &= 4\pi G a^2 \sum_{\mathrm{a}} \left(\delta\rho_{\mathrm{a}} + 3Ha\left(\rho_{\mathrm{a}} + P_{\mathrm{a}}\right)\frac{\theta_{\mathrm{a}}}{k^2}\right) \\ k^2(\Phi+\Psi) &= -8\pi G a^2 \sum_{\mathrm{a}} P_{\mathrm{a}}\Pi_{\mathrm{a}} \end{aligned} \tag{4.26}$$

where θ is the divergence of velocity $\theta = ik^i v_i$, and Π the scalar part of anisotropic stress $\Pi = -\frac{3}{2}\left(\frac{k_i k_j}{k^2} - \frac{1}{3}\delta_{ij}\right)\Pi^{ij}$.

The usual μ and σ formalism in studying modified gravity has a correspondence in these equations. Combining the above equations gives the generalized Poisson equation:

$$k^2(\Phi - \Psi) = 4\pi G a^2 \left(\delta\rho_T^{rest} + \delta\rho_{de}^{rest} + P_{de}\Pi_{de} + P_T\Pi_T\right) \tag{4.27}$$

where the subscript T stands for components other than dark energy.

To introduce the alternative closure relation as described above, one can introduce two functions on large-scale and small-scale limits:

$$\begin{aligned} &\frac{4\pi G}{H^2}\left(\rho_{de} + P_{de}\right)\frac{\theta_{de} - \theta_T}{k_H} = -\frac{1}{3}k_H\theta_T f_\zeta(a) \quad (k_H \ll 1) \\ &\Phi_- = \frac{4\pi G a^2}{k^2}\frac{\delta\rho_T^{rest} + P_T\Pi_T}{1+f_G} \quad (k_H \gg 1); \quad \Phi_- \equiv \frac{\Phi - \Psi}{2} \end{aligned} \tag{4.28}$$

and a dynamical parameter that interpolates between the two limits:

$$\Gamma = -\frac{4\pi G a^2}{k^2}\left(\delta\rho_{de}^{rest} + P_{de}\Pi_{de}\right) \tag{4.29}$$

As described above, this parameter describes the anisotropic stress of dark energy as the first closure relation:

$$k^2\left(\Phi_- + \Gamma\right) = 4\pi G a^2\left(\delta\rho_T^{rest} + P_T\Pi_T\right) \tag{4.30}$$

To satisfy the scale limit relation 4.28, Γ follows the evolution equation:

$$\left(1 + c_\Gamma^2 k_H^2\right)\left[\Gamma' + \Gamma + c_\Gamma^2 k_H^2\left(\Gamma - f_G\Phi_-\right)\right] = S \tag{4.31}$$

where:

$$\begin{aligned} S =& \frac{g' - 2g}{g+1}\Phi_- + \frac{4\pi G}{(g+1)k^2}(g\left[(P_T\Pi_T)' + P_T\Pi_T\right] \\ & - \left[\left(g + f_\zeta + g f_\zeta\right)\left(\rho_T + P_T\right) - \left(\rho_{de} + P_{de}\right)\right]\frac{\theta_T}{H}) \end{aligned} \tag{4.32}$$

and $g = \dfrac{\Phi - \Psi}{\Phi + \Psi}$, and $'$ denotes the derivative with respect to $\ln a$.

There are three functions that need to be specified in this formalism. f_G describes the evolution of the gravitational constant, which in our case is usually 0. f_ξ describes the large-scale behavior and g describes the anisotropy of the fluid.

Both of the functions $g(a,k)$ and $f_\xi(a,k)$ as a function of time and scale can be derived from the first principal, such as $f(R)$ gravity.

Here we study a phenomenological model such that $g \to 0$ at small scales and become scale independent on large-scale:

$$g(a,k) = \frac{g_{SH}(a)}{1 + (c_g k_H)^2} \tag{4.33}$$

where the superhorizon g_{SH} evolves as:

$$g_{SH}(a) = g_0\ a^{1.5}. \tag{4.34}$$

As shown in [121], f_ξ does not affect anisotropic stress very much, and we take it to be the same as superhorizon $f_\xi = g_{SH}$.

In this formalism of effective anisotropic stress using PPF, there are then two free parameters: g_0 that describes the anisotropic stress today, and c_g the scale when the anisotropic stress vanishes. It is worth noticing that this formalism is not unique. In fact, the PPF formalism above is not unique, but the evolution equations and the relations to the perturbations in the absence of $g(a,k)$ are implemented in the public version of CAMB/CLASS.

Apart from PPF formalism, we also implemented a fluid description as in [122]:

$$\pi_{de} \equiv e_\pi a^n \Delta_m \tag{4.35}$$

with $\Delta = \delta + 3\mathcal{H}(1+w)v/k$ the perturbation in the comoving gauge. The drawback of this description is that it cannot have $w = -1$. However, taking the limit $w \to -1$ is a good approximation.

Most of the current constraints rely on CMB [122, 123]. The anisotropic stress of dark energy gives an extra ISW effect with positive $g(a,k)$, specifically:

$$\begin{aligned} -k^2 \mathrm{ISW}_{\mathrm{stress}} =& 8\pi G a^2 \sum_A p_A \dot{\Pi}_A - 8\pi G a H \left[4 \sum_A p_A \Pi_A \right. \\ & \left. + \sum_A (3\rho_A - p_A)\,\Pi_A - \sum_A \frac{\mathrm{d}\ln w_A}{\mathrm{d}\ln a} p_A \Pi_A \right]. \end{aligned} \tag{4.36}$$

4.3.2 Modifications to the 2PCF in Galaxy Shear and Overdensity

With anisotropic stress of dark energy, the 2PCF used in the usual 3x2 analysis need to be modified to the extra distortion that light experience on the way from the source to the observer. As explained in Sec. 2.1, the transverse displacement of a source at $\chi\theta^i$ follows from the geodesic equation:

$$\frac{d^2}{d\chi^2}(\chi\theta^i) = \Phi_{,i} - \Psi_{,i} \tag{4.37}$$

without assuming no anisotropic stress in the late universe $\Phi + \Psi = 0$. From here, the Limber approximation still holds, which gives the angular power spectrum for cosmic shear as:

$$C^{ij}_{\kappa\kappa}(\ell) = \int dz \frac{H(z)}{\chi^2(z)} q^i_\kappa(z) q^j_\kappa(z) P_{\mathrm{WW}}\left(\frac{l+1/2}{\chi(z)}, z\right), \tag{4.38}$$

which reduces to the usual form of the matter power spectrum in the absence of anisotropic stress via the Poisson equation. Notice that our definition of $P_{\mathrm{WW}}(k,z)$ is not really the correlation between Weyl potential, but the rescaled with the k^2 and time dependant factor in the Poisson equation, namely:

$$P_{\mathrm{WW}}(k,z) = \langle \frac{\Phi_ H^2 k_H^2}{8\pi G}, \frac{\Phi_ H^2 k_H^2}{8\pi G} \rangle. \tag{4.39}$$

Similarly defined is also the angular power spectrum of cosmic shear and

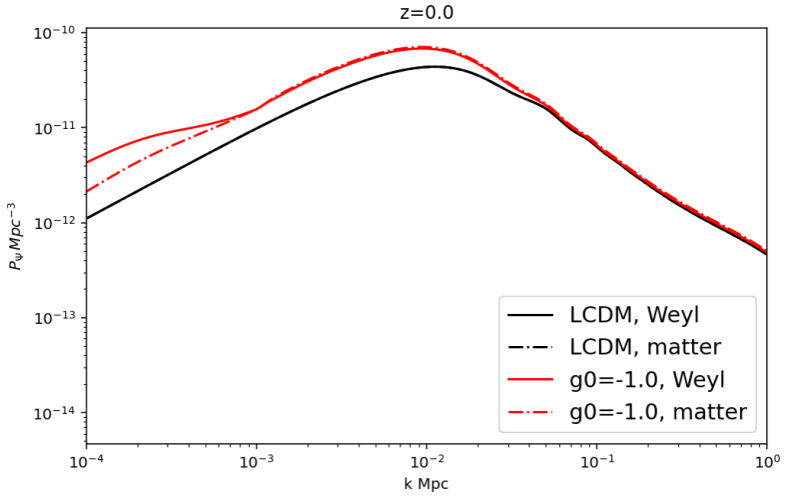


Figure 4.1: The power spectrum of Wely-Wely and matter-matter under LCDM and PPF-anisotropic-stress model.

galaxy over density:

$$C^{ij}_{\kappa\delta_g}(\ell) = \int dz \frac{H(z)}{\chi^2(z)} q^i_\kappa(z) q^j_{\delta_g}(z) P_{\rm WM}\left(\frac{l+1/2}{\chi(z)}, z\right), \tag{4.40}$$

with the power spectrum between the rescaled Weyl potential and matter over density $P_{\rm WM}$. The angular power spectrum of galaxy clustering is not modified, as it does not evolve the travel of light. The cosmic shear with Intrinsic Alignment also follows this discussion. The observed shear of the galaxy is the sum of light distortion and IA: $\langle \epsilon + I, \epsilon + I \rangle$. The matter power spectrum of the term. $\langle \epsilon, \epsilon \rangle$ is replaced with $P_{\rm WW}$, and the matter power spectrum in the cross term is replaced with $P_{\rm WM}$. This is consistent with the (μ, σ) or (μ, η) parameterization of modified gravity [124].

Figure 4.1 shows the Weyl-Weyl and matter-matter under LCDM and PPF-anisotropic-stress model as discussed above. As can be seen from the figure, under LCDM, there is no difference between the matter and Weyl power spectrum. However, when an anisotropic stress term is present, it does not only change the total power spectrum as an effective sound speed, but it also creates the difference between Weyl and matter. Since this is not the scale that weak lensing survey mainly probes, the difference between using Weyl and matter is small. The choices above is consistent with DES-Y3 extension model analysis [90].

Chapter 5

Models of Dark Energy II: Scalars

5.1 Basics: A general scalar field

The discussion of this section follows mainly with [15, 125], with an effort to follow the notations close to recent literature.

We start with a general scalar field, which is sometimes referred to k-essence following the k-inflation theories. It reduced to the usual quintessence when the kinetic term vanishes. The advantage of k-essence dynamics over a tracker quintessence model is that it doesn't require a fine-tuning of initial conditions or mass parameters in some specific cases.

The action of a general scalar field is:

$$S = \int \mathrm{d}^4x\sqrt{-g}\left[\frac{1}{2\kappa^2}R + P(\phi, X)\right] + S_m, \tag{5.1}$$

where $X \equiv \dot{\phi}^2/2$, S_m is the matter action, and R is the Ricci scalar. This action is a subset of the Hordeski Theory [126, 127].

$P(\phi, X)$ represents the scalar field, which is reduced to the canonical case (quintessence) if it takes the form:

$$P(\phi, X) = \frac{1}{2}\dot{\phi}^2 - V(\phi). \tag{5.2}$$

There are various models with different kinds of $P(\phi, X)$. An incomplete summary of models is presented in Table. 5.1.

There are a lot of other k-essence models. For example, in [128] there's a discussion of the purely kinetic model with $P = F(X)$.

Name of Model	**Form of P**
Low energy effective String	$K(\phi)X + L(\phi)X^2$
Ghost Condensate	$-X + e^{\kappa\lambda\phi}X^2/M^4$
Tachyon field	$-V(\phi)\sqrt{-\det\left(g_{\mu\nu} + \partial_\mu\phi\partial_\nu\phi\right)}$
Dirac–Born–Infeld (DBI)	$-f(\phi)^{-1}\sqrt{1-2f(\phi)X} + f(\phi)^{-1} - V(\phi)$

Table 5.1: An incomplete summary of k-essence models.

For any general k-essence model, the field equation is given by the action 5.1:

$$R_{\mu\nu} - \frac{1}{2}g_{\mu\nu}R = \kappa^2\left(\frac{\partial P(\phi,X)}{\partial X}\nabla_\mu\phi\nabla_\nu\phi + P(\phi,X)g_{\mu\nu} + T^{\text{other}}_{\mu\nu}\right), \tag{5.3}$$

from which we can read the energy density and pressure as:

$$\begin{aligned}\rho_\phi &= 2X\frac{\partial P}{\partial X} - P,\\ p_\phi &= P(\phi,X).\end{aligned} \tag{5.4}$$

For any general k-essence model, the extrema of $P(\phi,X)$ with respect to X has an EoS same as the cosmological constant: $\rho+p = 2X\partial p/\partial X = 0$. The Friedman equations are:

$$\begin{aligned}H^2 &= \frac{\kappa^2}{3}\left(\rho_B+\rho_\phi\right) = \frac{\kappa^2}{3}\left(\rho_B + 2X\frac{\partial p}{\partial X} - p\right)\\ \ddot{a} &= -\frac{\kappa^2}{6}\left(\rho_B + 3p_B + \rho_\phi + 3p_\phi\right),\\ \dot{\rho}_B &= -3H\left(1+w_B\right)\rho_B\\ 0 &= \ddot{\phi}\left(\frac{\partial p}{\partial X} + \dot{\phi}^2\frac{\partial^2 p}{\partial X^2}\right) + 3H\frac{\partial p}{\partial X}\dot{\phi} + \frac{\partial^2 p}{\partial X\partial\phi}\dot{\phi}^2 - \frac{\partial p}{\partial\phi}\end{aligned} \tag{5.5}$$

where the subindex B denotes the background. One can check that the appropriate choice of action reduces the equations to the quintessence case.

For the convenience of coding, we also use this form of the Klein-Gordon Equation:

$$(P_{,X} + \frac{P_{,XX}\phi'^2}{a^2})\phi'' + 2\mathcal{H}\phi' + (P_{,X\phi} - \frac{\mathcal{H}\phi'}{a^2})\phi'^2 - a^2P_{,\phi} = 0, \tag{5.6}$$

where the prime denotes derivatives with respect to the conformal time.

5.1.1 Separable Lagrangian

There exists a lot of literature discussing the behavior of a separable Lagrangian $P(\phi, X) = V(\phi)F(X)$. The dynamics of the field and attractor properties are discussed in [15]. For $P = V(\phi)F(X)$, the EoS is:

$$w_\phi = \frac{F}{2XF_X - F} \tag{5.7}$$

where we used $p_\phi = P$, and $\rho_\phi = V(\phi)\left[2XF_{,X} - F\right]$. The sound speed is defined as following [129]:

$$c_s^2 \equiv \frac{(\partial p/\partial X)}{(\partial \rho/\partial X)} = \frac{F_{,X}}{F_{,X} + 2XF_{,XX}} \tag{5.8}$$

Notice that the sound speed here is different from the sound speed defined in eq 68 of [55]. The sound speed here appears as the coefficient of k^2/a^2.

5.1.2 Field Redefinition

It is very useful to do the following field redefinition for a general action of form $P = K(\phi)X + L(\phi)X^2$ to:

$$\phi_{\text{new}} = \int^{\phi_{\text{old}}} d\phi \frac{L(\phi)^{1/2}}{|K(\phi)|^{1/2}} \tag{5.9}$$

where $\phi \equiv \phi_{\text{new}}$, $X \equiv X_{\text{new}} = (L/|K|)X_{\text{old}}$, and $f(\phi) \equiv K^2\left(\phi_{\text{old}}\right)/L\left(\phi_{\text{old}}\right)$. Which then gives:

$$\begin{aligned} p &= f(\phi)\left(-X + X^2\right) \\ \rho &= 2X\frac{\partial p}{\partial X} - p = f(\phi)\left(-X + 3X^2\right) \end{aligned} \tag{5.10}$$

In this way, we can use Eq. 5.10 to analyze a range of general models, and it's easier both in coding and phase space analysis. For example, we can rewrite the diatonic ghost field $P = -X + c_1 e^{\lambda\phi}X^2$ to $P = c_2 e^{-\lambda\phi}(-X + X^2)$. Thus, the scalars of this form also follow our discussion of the separable Lagrangian.

5.2 Properties of k-essence

We discuss in this section the stability condition of a k-essence field, which leads to the requirement of building an attractor model. We provide dilatonic ghost field as an example.

5.2.1 Stability

It is useful to define $F(X) = g(y)/y$, with $y = X^{-1/2}$. Thus, in terms of the new variable y:

$$w_\phi = -\frac{g(y)}{yg'(y)}, \quad c_s^2 = \frac{g(y) - yg'(y)}{y^2 g''(y)} \tag{5.11}$$

The positivity of energy density requires $[2XF_{,X} - F] > 0$, or:

$$-g' > 0 \tag{5.12}$$

The stability only requires $c_s^2 > 0$ in classical fluctuations. However, we require both the numerator and the denominator to be positive for the stability of quantum fluctuations [112]:

$$\begin{aligned} y^3 g'' &> 0 \\ g(y) - yg'(y) &> 0 \end{aligned} \tag{5.13}$$

Causality also requires the sound speed to be less than 1:

$$g(y) - yg'(y) \leq y^2 g''(y) \tag{5.14}$$

More discussions need to be made for whether a superluminal propagation would break causality structure or not [130].

5.2.2 Attractors

The tracker field [131] is an idea to solve the coincidence problem by which the dark energy field follows the energy density of other components. The tracker field often has an attractor-like solution to allow the scalar field to have a wide range of initial conditions. Note that this is not the only solution to the coincidence problem or fine-tuning problem. We present here the conditions in the case of the k-essence field.

Conditions for an Attractor

The conservation law (the third equation in eq 5.5) in terms of variable y is:

$$\frac{dy}{dN} = \frac{3}{2}\frac{(w_\phi(y) - 1)}{r'(y)}\left[r(y) + \sigma\frac{K_{,\phi}}{2K^{3/2}}\sqrt{\frac{\rho_\phi}{\rho_{tot}}}\right], \tag{5.15}$$

where

$$r(y) \equiv \left(-\frac{9}{8}g'\right)^{1/2} y\,(1 + w_\phi) = \frac{3}{2\sqrt{2}}\frac{(g - g'y)}{\sqrt{-g'}}. \tag{5.16}$$

and $\sigma \equiv \text{sign}(d\varphi/dN)$.

For a tracking solution of the matter-dominated era, we require:

$$w_\phi(y) = -\frac{g}{yg\prime} = w_m, \tag{5.17}$$

and we see from Eq. 5.15 that we should have $P = g(y)/\phi^2 y$ as a scaling solution for the matter-dominated era.

In this case, the evolution equation 5.15 reduced to:

$$\begin{aligned} \frac{\mathrm{d}y}{\mathrm{d}N} &= \frac{2\sqrt{-6g'(y)}}{yg''(y)}\left[r(y) - \sqrt{\Omega_\phi}\right] \\ \frac{\mathrm{d}\Omega_\phi}{\mathrm{d}N} &= 3\Omega_\phi\left(1-\Omega_\phi\right)\left(w_{rm} - w_\phi\right) \\ \frac{\mathrm{d}w_{rm}}{\mathrm{d}N} &= w_{rm}\left(3w_{rm} - 1\right) \end{aligned} \tag{5.18}$$

where:

$$r(y) \equiv \frac{\sqrt{6}}{4}\frac{g(y) - yg'(y)}{\sqrt{-g'(y)}}, \quad \Omega_\phi \equiv \frac{\rho_\phi}{3H^2}, \quad w_{rm} \equiv \frac{\rho_r}{3\left(\rho_r + \rho_m\right)} \tag{5.19}$$

In order to find the attractors, let us expand the field derivative and energy density with perturbations: $y(N) = y_m + \delta y$, and $\Omega(N) = \Omega_m + \delta\Omega$. Substituting into first two equations of 5.18 and take derivative gives:

$$\frac{d^2\delta y}{dN^2} + \frac{3}{2}\left(1 - w_m\right)\frac{d\delta y}{dN} + \frac{9}{2}\left(1 - r_m^2\right)\left(1 + w_m\right)\left(c_S^2 - w_m\right)\delta y = 0 \tag{5.20}$$

where the index "m" denotes the evaluation at y_m.

This second-order differential equation has two exponential solutions. It's easy to see the condition for both solutions to be exponentially decay given $|w_m| < 1$ is:

$$c_s^2 = \frac{g(y) - yg'(y)}{y^2 g''(y)} > w_m \tag{5.21}$$

So an attractor can be easily made by imposing a small second derivative of $g(y)$.

Trackers and Fixed point

In this section, we assume the action of the form $P = g(y)/\phi^2 y$

A. Radiation Era

Similar to the scaling solution of the matter-dominated era, for radiation tracker $w_\phi = w_r m = 1/3$, we have:

$$y_r g'(y_r) = -3g(y_r), \tag{5.22}$$

and $\Omega_\phi(y_r) = r^2(y_r) < 0.045$ from BBN bound. The bound is constrained well as detailed in 2.3.3. If the energy density is too much smaller, then there would not be enough DE at the onset of the matter-dominated era, and DE would not overtake matter today.

B. Matter Era

The calculation can be similarly carried to the matter-dominated era. We omit the calculation procedure and summarize the conclusions below. For details, see Ref. [15].

There are two kinds of fixed points in this model:

- de Sitter Fixed Point: $w_{rm} = 0$, and $\Omega_\phi = r^2(y_m) \approx 0$, which gives $w_\phi = -1$
- Dust Fixed Point: $w_{rm} = w_\phi = 0$, but $\Omega_\phi(y_m) \neq 0$.

C. Acceleration Era

There exists a k-essence acceleration attractor that the equation will finally reach: $w_{rm} = 0$, and $-1 < w_\phi < 1$, and $\Omega_\phi(y_k) \approx 1$

In general, if $r(y_0) > 1$ for some y_0 so there exits an attractor such at $r(y_S) = 0$ (also called the **S**-attractor). Due to continuity of $r(y)$, there exits a k-attractor y_k such that $y_0 < y_k < y_S$.

5.2.3 Dilatonic Ghost Condensate: A Example

The phase space analysis of dilatonic ghost field in CLASS units [1] is easier by defining the following combinations:

$$x_1 = \frac{\phi'}{\sqrt{2}aH}, \quad x_2 = \frac{e^{\lambda\phi}\phi'^2 c_1}{2a^2 H_0^2}, \quad x_3 = \frac{\sqrt{\rho_r}}{H} \tag{5.23}$$

[1] CLASS adopts a non-standard unit system such that $H^2 = \sum \rho_{\text{CLASS}}$. This definition makes the density to be $1/3$ of the physical density, and thus some terms in the field equations differ by a factor. One should pay extra attention when implementing the equations to CLASS.

The fixed points can be determined by:

$$w_{\text{eff}} = -1 - \frac{2\dot{H}}{3H^2} = -x_1^2 + x_1^2 x_2 + \frac{1}{3}x_3^2, \quad w_\phi = \frac{P_\phi}{\rho_\phi} = \frac{1 - x_2}{1 - 3x_2} \tag{5.24}$$

If we have $P = -X + e^{\lambda\phi}X^2 c1/H_0^2$, and thus the saddle points are the same as in [125]:

- Radiation point: $(x_1, x_2, x_3) = (0, 1/2, 1)$
- Matter point $(x_1, x_2, x_3) = (0, 1/2, 0)$
- acceleration point $(x_1, x_2, x_3) = \left(-\sqrt{6}\lambda f_-(\lambda)/4, 1/2 + \lambda^2 f_+(\lambda)/16, 0\right)$

where:

$$f_\pm(\lambda) \equiv 1 \pm \sqrt{1 + 16/\left(3\lambda^2\right)} \tag{5.25}$$

5.2.4 Phantom Behavior

As discussed in [132], the power model with some value can lead to phantom behavior, i.e., with $w < -1$. However, k-essence, although more general than quintessence, can still not pass the $w = -1$ point; the equation of state can only always be greater than or smaller than -1. The models that have this feature is called "quintom"; they often require two scalar fields or vector field.

Also, the $w < -1$, in general, suffers from the quantum and classical instability [112], although phenomenological, it seems the only way to solve the H_0 tension with a late-time modification is to allow phantom. We do not further discuss this question in this thesis.

5.3 Perturbations in k-essence

5.3.1 Perturbation Equations In Newtonian Gauge

In this section, we derive the perturbation equations for a general scalar field.

In order to follow Ref. [133] which derived the equations in Newtonian gauge, we rewrite the metric in Newtonian gauge as $ds^2 = (-1 + 2\Phi)dt^2 + \delta_{ij}a^2(t)(1 + 2\Psi)dx^i dx^j$, and flip the definition of the action with $K(\phi, X) \equiv -P(\phi, X)$.

The first-order perturbed Einstein equation, including the generalized k-essence action part, is then:

$$
\begin{aligned}
-6H^2\Phi - 2\frac{k^2}{a^2}\Psi - 6H\dot{\Psi} =& \kappa^2 \left\{ \left(P_{,X} - \dot{\phi}^2 P_{,XX} \right) \left(\dot{\phi}^2 \Phi + \dot{\phi}\delta\dot{\phi} \right) \right. \\
& - \left(-P_{,\phi} + \dot{\phi}^2 P_{,X\phi} + 2\dot{\phi} P_{,X} \partial_0 \right) \delta\phi \\
& \left. -2\Phi\dot{\phi}^2 P_{,X} - \delta\rho \right\}, \\
2\partial_i (H\Phi + \dot{\Psi}) =& \kappa^2 \left\{ -\dot{\phi} P_{,X} \partial_i \delta\phi + (\rho + p)\delta u_i \right\}, \\
k^2(\Phi - \Psi) =& 0, \\
\left(\frac{k^2}{a^2} + \frac{\partial_i \partial_i}{a^2} - 2H\partial_0 - 4\dot{H} - 6H^2 \right) \Phi - & \left(\frac{k^2}{a^2} + \frac{\partial_i \partial_i}{a^2} + 2\partial_0 \partial_0 + 6H\partial_0 \right) \Psi \\
=& \kappa^2 \left\{ P_{,X} \left(\dot{\phi}^2 \Phi + \dot{\phi}\delta\dot{\phi} \right) + P_{,\phi}\delta\phi + \delta p \right\},
\end{aligned}
\tag{5.26}
$$

which reduced to equation 23 of [55] in Fourier mode if P vanishes and assuming vanished shear terms. Otherwise, the third equation would have the shear stress contribution on the right-hand side.

The perturbative equations of matter given by continuity equation at first order $T^{\mu\nu}_{\ \ ,\mu}$ is:

$$
\begin{aligned}
\delta\dot{\rho} + 3H(\delta\rho + \delta p) + a^{-2}\partial_i \left\{ (\rho + p)\delta u_i \right\} + 3\dot{\Psi}(\rho + p) = 0 \\
a^{-3}\partial_0 \left\{ a^3 (\rho + p)\delta u_i \right\} + \partial_i \delta p - (\rho + p)\partial_i \Phi = 0
\end{aligned}
\tag{5.27}
$$

which reduces to equation 30 of [55].

The generalized part is the scalar field evolution equation:

$$
\begin{aligned}
\left(\dot{\phi}^2 P_{,XX} + P_{,X} \right) \delta\ddot{\phi} = & -3\dot{\phi} P_{,X} \dot{\Psi} + \\
& \left(-\dot{\phi} P_{,X} \partial_0 - \dot{\phi}^3 P_{,XX} \partial_0 - 6H\dot{\phi} P_{,X} - 2\ddot{\phi} P_{,X} - 2\dot{\phi} \dot{K}_{,X} \right. \\
& \left. -3H\dot{\phi}^3 P_{,XX} - 3\dot{\phi}^2 \ddot{\phi} P_{,XX} - \dot{\phi}^3 \dot{P}_{,XX} + \dot{\phi}^2 P_{,\phi X} \right) \Phi \\
& - \left(3HP_{,X} + \dot{P}_{,X} + 3H\dot{\phi}^2 P_{,XX} + 2\dot{\phi}\ddot{\phi} P_{,XX} + \dot{\phi}^2 \dot{P}_{XX} \right) \delta\dot{\phi} \\
& + \left(-P_{,X} \frac{k^2}{a^2} - 3H\dot{\phi} P_{,X\phi} - \dot{\phi} \dot{P}_{,X\phi} - \ddot{\phi} P_{,X\phi} + P_{,\phi\phi} \right) \delta\phi
\end{aligned}
\tag{5.28}
$$

5.3.2 Subhorizon approximation

In the subhorizon approximation, $H^2, H\partial_0, \partial_0^2 \ll k^2/a^2$. If we further adopt $\delta p = 0$, then from equation 5.28, we have:

$$|\Psi| \gg |\delta\phi/\phi|. \tag{5.29}$$

Then from the first equation of 5.26, we have the desired Poisson equation:

$$2\frac{k^2}{\kappa^2 a^2}\Psi = \delta\rho \tag{5.30}$$

Thus, the scalar dark energy sector $P(\phi, X)$ does not contribute in the subhorizon scale, and the perturbation equations should remain the same as in the ΛCDM model.

However, here we actually adopt two approximations. First, the small scale $H^2 \ll k^2/A^2$. Second, $\partial_0\Psi \simeq H\Psi$, which is only valid if the propagation speed of metric perturbation is much smaller than the speed of light.

5.3.3 Perturbation Equations in Synchronous Gauge

We use the following Synchronous Gauge convention:

$$ds^2 = a^2(\tau)\left[-d\tau^2 + (\delta_{ij} + 2H_L\delta_{ij} + 2H_{Tij})\, dx^i dx^j\right]. \tag{5.31}$$

For quintessence, it is easy to write done

$$\delta\rho = \frac{1}{a^2}\left(\dot{\phi_0}\dot{\delta\phi}\right) + V'(\phi_0)\,\delta\phi, \tag{5.32}$$

following the definition $\rho = -1/2 g^{uv}\phi_{,u}\phi_{,v} + V$.

In k-essence with the synchronous gauge, $\delta g^{00} = 0$, we can perturb density and pressure 5.4 as:

$$\begin{aligned}
\delta p &= P_{,X}\delta X + P_{,\phi}\delta\phi \\
\delta\rho &= -\delta P + 2\delta X P_{,X} + 2X P_{,XX}\delta X + 2X P_{,X\phi}\delta\phi \\
&= P_{,X}\delta X - P_{,\phi}\delta\phi + 2X P_{,XX}\delta X + 2X P_{,X\phi}\delta\phi
\end{aligned} \tag{5.33}$$

where $\delta X = \frac{1}{a^2}\phi'\delta\phi'$.

To determine the perturbative equations of motion, we start with the non-

perturbative equation of motion:

$$P_{,\phi} + \nabla_\mu \left(P_{,X}\partial^\mu\phi\right) = 0, \tag{5.34}$$

one can check that this is the same as the last equation of 5.5.

The perturbative equations before specifying the metric is:

$$0 = P_{,\phi\phi}\delta\phi + P_{,\phi X}\delta X + \nabla_\mu \left(\delta P_{,X}\partial^\mu\phi + P_{,X}\partial_\alpha\phi\delta g^{\alpha\mu} + P_{,X}\partial^\mu\delta\phi\right) + \delta\Gamma^\mu_{\mu\lambda}P_{,X}\partial^\lambda\phi \tag{5.35}$$

In synchronous gauge, the non-zero Christoffel Symbol includes

$$\begin{aligned}\Gamma^\mu_{0\nu} &= \mathcal{H}\delta^\mu_\nu \\ \delta\Gamma^\mu_{0,\nu} &= \frac{1}{2}(g^{ij}\delta g_{ij,0} + \delta g^{ij}g_{ij,0}) = 1/2(3\frac{1}{a^2}(2a^2H_L' + 4aa'H_L) - \frac{2H_L}{a}2aa' \times 3) \\ &= 3H_L'\end{aligned} \tag{5.36}$$

For the convenience of coding, instead of arranging the terms as in the Klein-Gordan equation, we first write the equation of motion as:

$$A\varphi'' + B + C + +D + E(h,\eta) = 0 \tag{5.37}$$

where:

$$\begin{aligned}\varphi &= \delta\phi \\ A &= -P_{,XX}\phi'^2/a^4 - P_{,X}/a^2 \\ B &= +P_{,XX}\frac{\phi'^2}{a^2}\varphi'' + (\nabla_\mu(\delta P_{,X}\partial^\mu\phi)) \\ C &= +P_{,X}\varphi''/a^2 + \nabla_\mu(P_{,X}\partial^\mu\delta\phi) \\ D &= P_{,\phi\phi}\delta\phi + P_{,\phi X}\delta X + \nabla_\mu(P_{,X}\partial_\alpha\phi\delta g^{\alpha\mu}) \\ E &= \delta\Gamma^\mu_{\mu\lambda}P_{,X}\partial^\lambda\phi\end{aligned} \tag{5.38}$$

The reason for writing in this way is to separate the φ'' term and make it easy

to track. After specifying the metric, we have:

$$\begin{aligned}
B &= -4\mathcal{H}\phi'(\delta P_{,X})/a^2 + \delta P_{,X}\phi'(+\frac{2a'}{a^3}) + B^* = B^* - 2\mathcal{H}\phi'(\delta P_{,X})/a^2 \\
C &= (-P_{,XX}X' - P_{,X\phi}\phi' - 4\mathcal{H}P_{,X})\varphi'/a^2 - P_{,X}\frac{k^2}{a^2}\varphi + 2P,_X\frac{\varphi' a'}{a^3} \\
&= -2\frac{\mathcal{H}}{a^2}P_{,X}\varphi' - \frac{\varphi'}{a^2}(P_{,XX}X' + P_{,X\phi}\phi') - P_{,X}\frac{k^2}{a^2}\varphi \\
D &= P_{,\phi\phi}\varphi + P_{,\phi X}\delta X \\
E &= -3H_L' P_{,X}\phi'/a^2 \\
\delta P_{,X} &= P_{,XX}\delta X + P_{,X\phi}\varphi \\
(\delta P_{,X})' &= P_{,XXX}X'\delta X + P_{,XX\phi}\phi'\delta X + P_{,XX}\delta X' \\
&\quad + P_{,X\phi X}X'\varphi + P_{,X\phi\phi}\phi'\varphi + P_{,X\phi}\varphi' \\
\delta X &= \frac{1}{a^2}\phi'\varphi' \\
(\delta X)' &= \frac{\phi'}{a^2}\varphi'' + \frac{\phi''\varphi'}{a^2} - \frac{2a'\phi'\varphi'}{a^3} \\
X' &= \frac{\phi'\phi'' - \mathcal{H}\phi'^2}{a^2} \\
B^* &= +\delta P_{,X}(-\frac{\phi''}{a^2}) - \frac{\phi'}{a^2}(\delta P_{,X})' + P_{,XX}\frac{\phi'^2}{a^2}\varphi'' \\
&= -\frac{\phi'}{a^2}(P_{,XXX}X'\delta X + P_{,XX\phi}\phi'\delta X + P_{,X\phi X}X'\varphi + P_{,X\phi\phi}\phi'\varphi + P_{,X\phi}\varphi' \\
&\quad + P_{,XX}(\frac{\phi''\varphi'}{a^2} - \frac{2a'\phi'\varphi'}{a^3})) + \delta P_{,X}(-\frac{\phi''}{a^2})
\end{aligned} \tag{5.39}$$

Note that B* is defined in the first line so that the calculation can be simplified. The equation written in this form is easier to track if one do all the calculations by hand. It's tedious but should be clear.

To make the equation more familiar with the quintessence Klein Gordon equation, we define:

$$\tilde{A}\varphi'' + \tilde{B}\varphi' + \tilde{C}\varphi + \tilde{D} = 0 \tag{5.40}$$

where:

$$
\begin{aligned}
\varphi &= \delta\phi \\
\tilde{A} &= P_{,XX}\phi'^2/a^2 + P_{,X} \\
\tilde{B} &= 2\mathcal{H}P_{,X} + P_{,XXX}\frac{X'\phi'^2}{2} + P_{,XX\phi}\frac{\phi'^3}{a^2} + P_{,XX}(+3\frac{\phi'\phi''}{a^2} - \frac{\mathcal{H}\phi'^2}{a^2}) + P_{,X\phi}\phi' \\
\tilde{C} &= -a^2 P_{,\phi\phi} + P_{,X}k^2 + P_{,XX\phi}X'\phi' + P_{,X\phi}\phi'' + P_{,\phi\phi X}\phi'^2 + 2\mathcal{H}P_{,X\phi}\phi' \\
\tilde{D} &= 3H_L' P_{,X}\phi'
\end{aligned}
\tag{5.41}
$$

In order to get $(P+\rho)\theta$, it's easier to work on the energy-momentum tensor (within synchronous gauge):

$$
\begin{aligned}
T_{ab} &= Pg_{ab} + P_{,X}\partial_a\phi\partial_b\phi \\
\delta T_{ab} &= P_{,X}\delta X g_{ab} + P_{\phi}\varphi g_{ab} + P_{,XX}\delta X\partial_a\phi\partial_b\phi \\
&\quad + P_{,X\phi}\varphi\partial_a\phi\partial_b\phi + P_{,X}\partial_a\phi\partial_b\varphi P_{,X}\partial_b\phi\partial_a\varphi \\
\delta T_{i0} &= P_{,X}\phi' k_i\varphi \\
(\rho+p)\theta &\equiv k_i\delta T_0^i = P_{,X}\frac{k^2}{a^2}\phi'\varphi
\end{aligned}
\tag{5.42}
$$

The above equations have been checked with the Mathematica program X-PAND and implemented in CLASS-GSF.

Figure 5.1 shows the effect of the dilatonic ghost field [134] on the linear matter power spectrum. At redshift zero, the effect is strongly correlated with other variables, but in the evolution history, such a model is distinguishable from the cosmological constant due to the change of expansion history.

5.4 Discussion

One of the largest missing parts of studying the non-perfect fluid and scalar dark energy model is the non-linearity calculation.

Non-linearity in the standard LCDM model is usually calculated with halo model-inspired code such as Halofit or HMcode [135]. They both provide fitting formulas that aim to relate the cosmological parameters with N-body simulation. Nonstandard but smooth dark energy models are also considered with the so-called Casarini prescription [136]. The essential step is to emulate the effective comoving distance under the modified expansion history to that of the wCDM case. We also adopt this method in our study of Early+Late

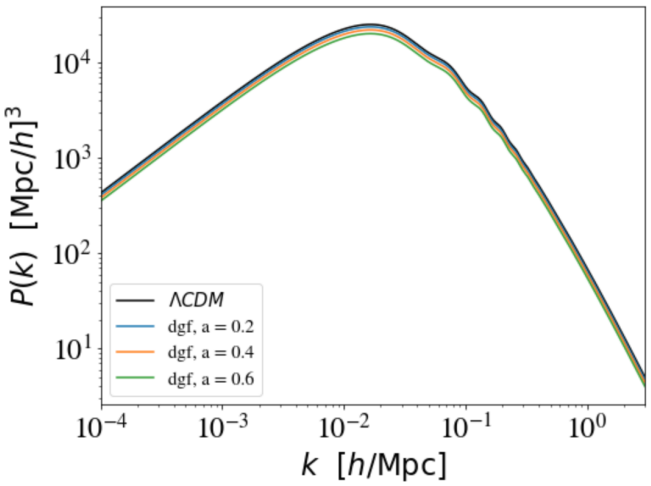


Figure 5.1: Effects of a Dilatonic Ghost Field on the linear matter power spectrum. a is the amplitude of the second-order derivative term.

dark energy.

In recent years people have developed emulators of the non-linear boost factor built on high-resolution N-body simulation. A good example is the EuclidEmulator [137]. The cosmological parameters are restricted to a relatively small range where they trained and validated the emulator. In our study of growth and geometry split, we adopt this method [49]. The EuclidEmulator provides some minimal extension scenarios such as $w_0 - w_a$ and the massive neutrino model, but this method cannot be generalized into an arbitrary expansion rate similar to Casarini's prescription.

The inclusion of non-smooth dark energy or modified gravity makes the non-linear calculation difficult. There is recent progress in emulating non-linearities within the Hordeski effective theory called Hi-Cola [138]. In theory, people can do similar Cola simulations on specific models, and such work will be essential as future surveys dramatically increase the constraining power only if the observable is in the non-linear regime. Unfortunately, this discussion is beyond the scope of this thesis.

Chapter 6

The Hubble Tension and Early Dark Energy

The Hubble tension refers to a discrepancy in measurements of the expansion rate of the universe. It remains the most serious problem of the ΛCDM model. For a recent review, see Ref.**??**. In this chapter, we introduce the Hubble tension with a focus on the CMB inferred value. We then discuss two possible solutions and our effort to see how late time expansion could change the early dark energy predictions [139].

6.1 Hubble Tension

6.1.1 Hubble Constant Inferred from CMB

The relation that links the CMB measurement to the local expansion rate is:

$$\theta_* = \frac{r_*}{D(z_*)} \tag{6.1}$$

where the subscript * means the time and corresponding quantity. In CMB, this is where the optical depth of Thomson scattering reaches unity, i.e, the last scattering surface. θ_* is the angular size of the sound horizon, which can be inferred from the spacing between acoustic peaks, and is extremely well constrained by CMB measurement. r_* is the sound horizon at recombination or the comoving distance that a sound wave can travel from the Big Bang to the recombination. D_* is the comoving distance from the observer to the last scattering surface.

Similar to the recombination, the BAO obeys the same rule:

$$\theta_{\perp}^{\mathrm{BAO}}\left(z_{\mathrm{obs}}\right) \equiv \frac{r_{\mathrm{d}}}{D\left(z_{\mathrm{obs}}\right)}, \tag{6.2}$$

thus the method below would be valid for both CMB and BAO measurement.

The sound horizon at CMB is:

$$r_{\mathrm{s}}^{\star} = \int_0^{t_\star} \frac{dt}{a(t)} c_s(t) = \int_{z_\star}^{\infty} \frac{dz}{H(z)} c_s(t) \tag{6.3}$$

where $c_s(t)$ is the sound speed of the photon-baryon fluid. The comoving distance is:

$$D(z_*) = \int_0^{z_*} c dz / H(z) \tag{6.4}$$

where the redshift dependence of the Hubble parameter is model dependent, and in ΛCDM model the Friedman equation gives:

$$H(z) = \sqrt{\Omega_r H_0^2 (1+z)^4 + \Omega_m H_0^2 (1+z)^3 + \Omega_\Lambda H_0^2} \tag{6.5}$$

Given a cosmological model, all the parameters except $H(z)$ can be inferred from observation or calculated by theory. Thus, Eq. 6.1 allows us to determine the Hubble constant on all redshift values. And below is how each parameter is determined.

First, the sound photon-baryon sound speed c_s depends on the ratio of baryon to photon density. Photon and neutrino density $\Omega_r h_0^2$ can be measured precisely with present-day CMB temperature and standard models of BBN. Thus, c_s dependence reduced to baryon density $\omega_b \equiv \Omega_b h_0^2$.

Second, the total matter density and baryon density can be determined from the shape of the CMB spectrum, and this is indeed how we measure the CDM density $\Omega_{\mathrm{cdm}} = \Omega_m - \Omega_b$. A detailed review can be found in section 4 of [140], or section 2 of [54]. To fully understand the theory we need to look closely at the analytical functions of CMB anisotropy. The basic idea is that Ω_m is related to the early Integrated Sachs-Wolfe (ISW) effect and can be inferred from the envelope of the power spectrum, while Ω_b affects the scale of odd-even damping peaks.

The closure relation $\Omega_m + \Omega_r + \Omega_\Lambda = 1$ completes the last corner to determine H_0. And we can immediately see from here that there are several places we can try to alter in order to give a different H_0 value. One direction is to change relation 6.5. We need to be careful with the observational constraints when trying to test any model beyond ΛCDM.

6.1.2 Tension between Local Measurement and Possible Solutions

Another way, or rather Hubble's way, of measuring the Hubble constant is the local distance ladder. One only needs the local distance and speed if the object is close enough such that the two qualities are proportional. Usually, the speed can be easily measured with the spectrum redshift, but distance is tricky. That is where we need the so-called standard candle (or standard siren in case of the gravitational wave), such that the intrinsic brightness is known, and the distance can be inferred by measuring its apparent brightness. As introduced in Sec 2.3.2, SNIa is such an object. In reality, this observation is usually calibrated using Cepheid variable stars [141, 142].

The two kinds of unrelated measurement, CMB and local distance ladder, are in the tension of about 5σ [16, 143, 144]. Specifically, CMB predicts $H_0 = (67.4 \pm 0.5)\text{kms}^{-1}\text{Mpc}^{-1}$, while SH0ES team predicts $H_0 = 73.04 \pm 1.04$ km $\text{s}^{-1}\text{Mpc}^{-1}$.

In this thesis, we do not discuss the possible systematics that may bias the results. For this possibility, see [145] for example. Rather, we discuss the possibility that such tension might hint new physics that we need to add to our standard model of ΛCDM. For a detailed review of possible solutions, see [146].

The first and most obvious solution is the change of the dark energy equation of state, which changes the expansion history needed for CMB measurement through Eq. 6.5. There are two challenges to this solution. First, this modification would require a phantom behavior $w < -1$; as can be seen from Eq. 6.5 and 6.1, one need to increase $D(z)$ and thus decrease $H(z)$. The theoretical difficulty of phantom behavior is discussed in Sec. 5.2.4. Second, such a model would be very difficult to solve the save distance relation of BAO inference Eq. 6.2, which is the same thing, but the redshift is at $z \approx 1$.

Other solutions without changing the expansion history are also studied. For example, one can modify the standard physics process of recombination, namely a higher temperature that reduces the baryon drag epoch z_d. Another possibility is to modify the distance duality relation. All these solutions, together called pre-recombination solutions, face their theoretical and experimental challenges [146**?**].

Instead of decreasing matter density at late time, one can also increase the density at the early time (and early time only, namely, it diffuses away faster than the other components). By early here, we mean the time before recombination. One can do this with some neutrino coupling or study phenomenologically with a scalar field, which is usually called "Early Dark Energy (EDE)" [147]. We shall discuss this in more detail next section.

6.2 Models of Early Dark Energy

Following the discussion of scalar fields in Chapter 5, we assume a potential of the form:

$$V = V_0(1 - \cos(\phi/f))^n \quad , \quad V_0 \equiv m^2 f^2 \tag{6.6}$$

which has a local minimum of $V \sim \phi^{2n}$. The oscillation at the local minimum gives an equation of state

$$w_\phi = \frac{n-1}{n+1}. \tag{6.7}$$

For reasons discussed in [148], we usually take $n = 3$ as an example, but in principle, they can all do the work of early dark energy as long as it diffuses away faster than that of matter component.

"Rock'n Roll" EDE [149] is another similar potential that mimics the minimum behavior and is only designed to study Hubble tension:

$$V(\phi) = V_0 \left(\frac{\phi}{M_{\rm pl}}\right)^{2n}, \tag{6.8}$$

but such a scalar field does not oscillate.

Scalars of other forms can also realize early dark energy. For instance, there are Acoustic EDE [150], New EDE [151], Chameleon EDE [152], Chain EDE [153], and a lot more type that has coupling to the other components of the universe [154].

All these models behave very similarly at the background level but differ at the perturbation level. In this section, we only discuss the background behavior and its potential to solve or alleviate the Hubble tension. On the other hand, as we would also show later, such a simple extension may worsen the S_8 tension [155].

Figure 6.1 shows the fractional density of early dark energy fluid $f_{\rm ede} \equiv \rho_{\rm ede}/\rho_{\rm total}$. In order to restore cosmological concordance, such a quality needs to reach a maximum of 10% at redshift around matter-radiation equality.

This requirement, however, is not favored if one does not add a prior on the H_0 parameter. Specifically, Planck CMB data do not predict a non-zero $f_{\rm ede}$. While the ACT data does [156], such a preference vanished when people add the full multiple Planck data into ACT data. It is not clear if this means there is an inconsistency between Planck and ACT temperature anisotropy at $\ell > 650$.

When the late-time large-scale structure data are added, the evidence for non-zero early dark energy drops below 2σ [155]. In the original literature and a lot of other analyses, this likelihood is simply added as a prior on S_8. As

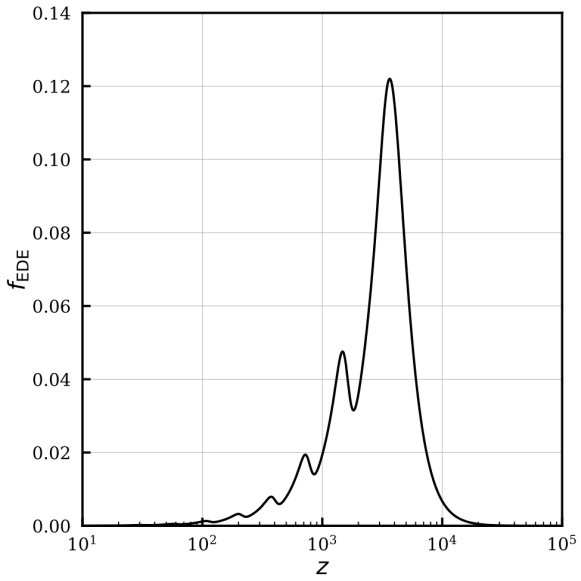


Figure 6.1: The relative density of early dark energy fluid. A peak value of about 10% around $z = 3000$ is the preferred value in resolving the Hubble tension. The figure is retrieved by class-ede

shown in Fig. 6.2, we found the same conclusion when the S_8 prior is replaced by weak lensing observable 3x2pt. This effect is mainly due to the shift of Ω_m in the presence of EDE and via the early ISW effect. A new component in the energy budget means Ω_m should be smaller, which leads to a larger Ω_c to compensate for the CMB measurement. This finally means more clustering in the late universe and worsens the S_8 tension [6]. A natural question is then: can this problem be solved when we allow the late-time dark energy to have a varying equation of state? We discuss this possibility in Sec. 6.4.

6.3 Interacting Neutrinos

Before discussing our result of marginalizing early-dark energy constraints over a late-time smooth dark energy behavior, we show in this section another intriguing solution to the Hubble tension: Strong Interacting Neutrinos (SIμ).

Assuming a simple toy model of neutrino self-interaction, with rate $\Gamma_\nu \propto G_{\rm eff}^2 T_\nu^5$, the posterior of $G_{\rm eff}$ under CMB temperature spectrum is characterized by two islands. First a moderately interactive $G_{\rm eff} \sim 10^{-4}{\rm MeV}^{-2}$ MIμ, and a strong interacting case $G_{\rm eff} \sim 10^{-1.5}{\rm MeV}^{-2}$, SI$\mu$. Such distribution is due to

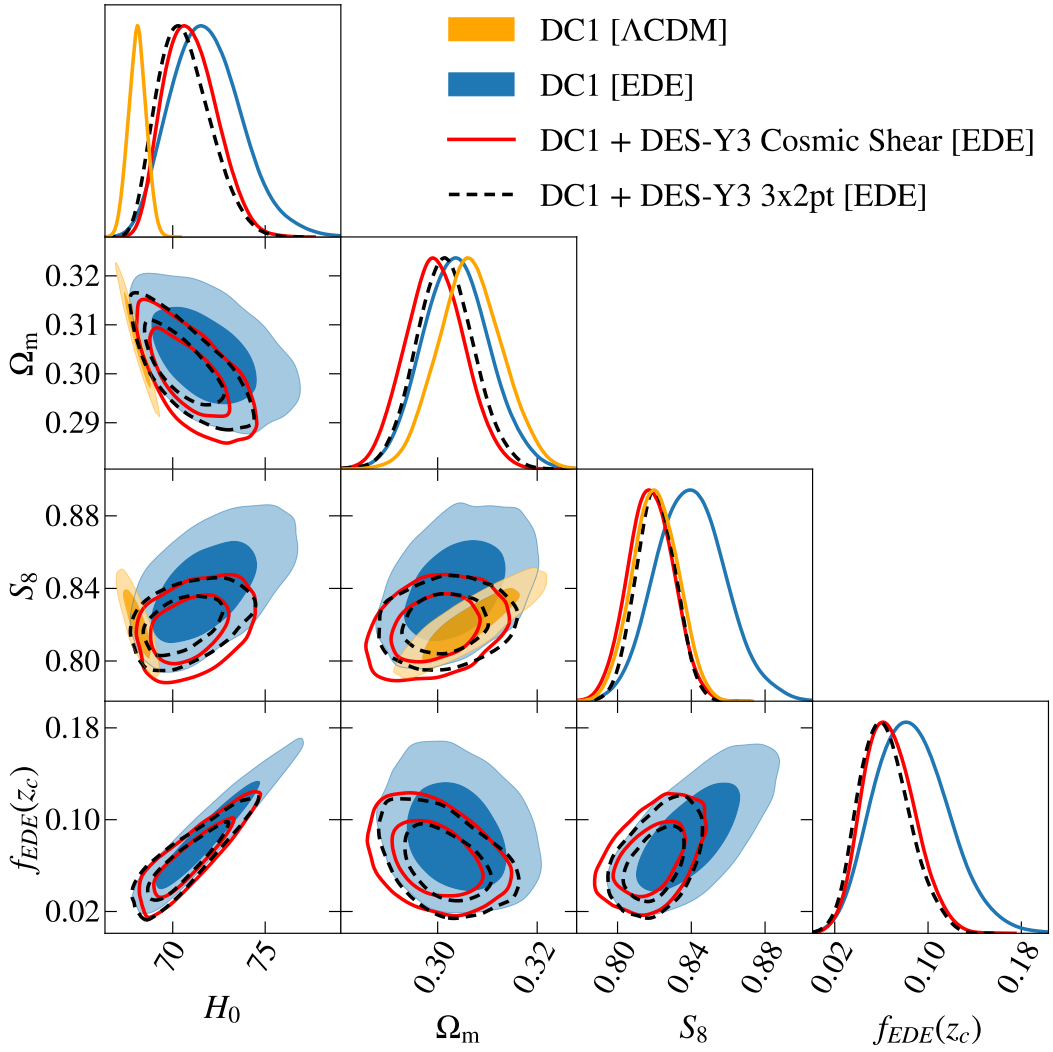


Figure 6.2: Posterior distribution of LCDM+EDE model. Here DC1 stands for dataset combination 1: CMB (ACT+Planck) + BAO + SNe + CMB-lensing

the degeneracy with parameters θ_*, A_s, and n_s [157].

With SNμ prefers a higher value of $N_{\rm eff}$, it solves the Hubble tension in the same way as early dark energy. However, this solution is disfavored by the Planck polarization data [158–160]. When replacing Planck with ACT+WMAP, SNμ is compatible with data at $2-3\sigma$ level [161], pointing another inconsistency between Planck and ACT at high multiple (this time for polarization at $700 < \ell < 1000$).

Recently, a "step" model was proposed to give a distinguishable high-ℓ and low-ℓ behavior [162, 163]. In this model, the radiation coupling is mediated by a complex scalar which becomes non-relativistic. The dark radiation undergoes a "step" where it receives energy from the mediator. The process is very similar to photon gains energy from electron-positron annihilation. The high-ℓ and low-ℓ modes behave differently depending on whether they enter the horizon before or after the step occurs. The detailed study of its effect on the perturbation of photon fluid shows that it improves the CMB fit alone compared with the standard SNμ case.

We do not go further than these simple discussions in this thesis. We just want to emphasize that there exist other possibilities of the pre-recombination solutions to the Hubble tension other than early dark energy. Considering the potential type of Eq. 6.6, we should keep an open eye on these interesting ideas.

6.4 Early + Later Dark Energy

In this section, we present the methodology and results of [139]. The question we are trying to answer is, if the presence of Early Dark Energy does not restore cosmological concordance with Λ being dark energy, does a very general time-varying dark energy fluid solve this problem? A spoiler before all the analysis is: no.

We consider a piecewise dark energy equation of state:

$$w(z) = \begin{cases} w_0, & \text{if } 0 \le z < z_1 \\ \dots & \\ w_{n-1}, & \text{if } z_{n-1} \le z < z_n \\ w_n = -1, & \text{if } z \ge z_n. \end{cases} \tag{6.9}$$

We test three different binning choices:

- $z_i = \{0.7, 1.4, 2.1\}$,
- $z_i = \{0.5, 1.0, 1.5, 2.0, 3.0\}$,

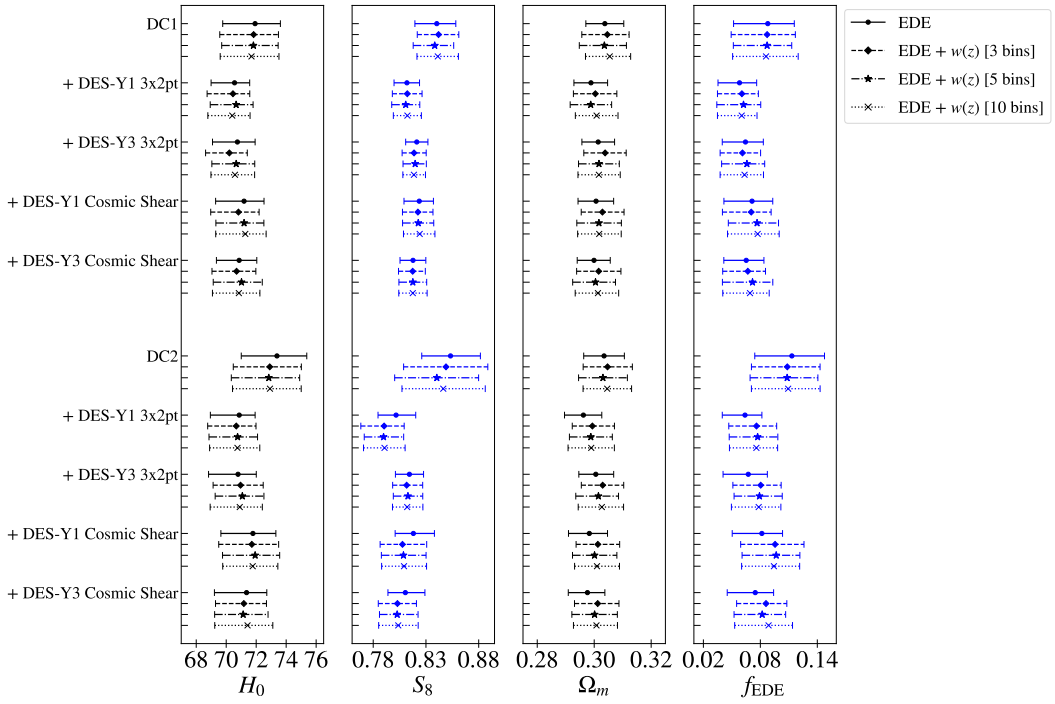


Figure 6.3: 1D Posterior distribution of wCDM+EDE with a piecewise w under different data set combinations. DC1 stands for dataset combination 1: CMB (ACT+Planck) + BAO + SNe + CMB-lensing. DC2 includes every data set as in DC1 except CMB-lensing.

- $z_i = \{0.3, 0.6, 0.9, 1.2, 1.5, 1.8, 2.1, 2.4, 2.7, 3.0\}$.

This choice is made such that at the second bin it could escape from the constraints of SNIa. The current SNIa does not provide much information for $z > 0.7$. We could test a smooth transition between each bin such as a tanh function type transition, but this model is sufficient to model the non-standard expansion history at the late universe and its effect on EDE constraints.

The main results are summarized in Fig. 6.3. DC1 contains CMB + BAO + SNe + CMBL, while DC2 does not have CMB lensing (CMBL). By comparing solid and dashed lines in the last column of $f_{\rm EDE}$, we could conclude that when no CMB lensing is included, the varying $w(z)$ could indeed increase the value of $f_{\rm EDE}$, although the increment is marginal. When CBML is added, however, the varying $w(z)$ basically does not do anything to the prediction of EDE parameters. This is not surprising as CMB lensing has a much longer window function and peaks at a much higher redshift $z \approx 2$. The detailed discussion can be found in the paper [139], including the tension evaluation and a comparison between different EDE models. Since the binned $w(z)$ rep-

resents a very general dark energy scenario in the smooth paradigm, this work shows that in order to solve the Hubble tension by reducing the sound horizon near recombination, we must also change the mechanisms for the clustering of matter to compensate for S_8.

6.5 Discussion

Hubble tension is one of the most discussed questions in cosmology in recent years. When I first heard such tension, the *sigma* is about 4, and now it grows to about 5.2σ. People have also realized it is very difficult to solve the tension, even by introducing some completely new component. The origin of the component is also suspicious, as the potential of the scalar field is not natural. There are new independent ways to measure the Hubble constant such as TRGB and through the time delay of a strong lensing system. New ways of measurement cannot reach the accuracy compared to SNIa yet. For some of them, we should not simply assume they will eventually one day be accurate enough. However, they do provide new perspectives and the measurement is with completely different systematics.

The problem of Hubble tension is also related to other cosmological tensions, as introduced in Sec. 6.4. Statistical tools such as tension metrics also need to be investigated to ensure the robustness of conclusions either against or for any solutions to the tension. Although the appearance of such tension does break the simpleness of the ΛCDM model, we should be excited about it as it may represent a chance of finding new physics.

Chapter 7

Emulator with Deep Learning to Boost Cosmological Inference

In this chapter, we summarize the attempt to create a machine-learning-based algorithm that emulates directly from the cosmological and astrophysical parameters to the data vector of 3x2pt. The bayesian process of cosmological parameter inference usually takes about 10^6 theoretical computation, which includes complicated integrals that takes a lot of computational resources. For the future survey, such a problem would become more severe with the need for more accuracy. For example, the DES analysis of the growth-geometry split takes months due to different prior and two-point function combinations. Such an analysis would be impossible without the help of computational resources at the University of Arizona. If we want to do an LSST forecast, the estimated time will go as high as more than a year, and we would possibly lose the potential to do an interesting analysis.

With an emulator, as we will show at the end of the chapter, an LSST Bayesian inference can be made in a few minutes and a few hours with external data. Due to trivial parallelization, the time to generate data vectors for training is only a few hours on the cluster at Stony Brook University.

In this section, we mainly present the result and validation of the emulator for LSST-Y1 3x2pt with the entire parameter space, where the cosmological parameters have the same bound as the EuclidEmulator [137]. We use another approach to generate the training samples. The result of this work is to be published soon. In Sec. 7.1, we introduce the basic ideas of neural networks, with a focus on the Transformer model [164]. In Sec. 7.2, we discuss the design of our emulator for both LSST. In Sec. 7.3.1, we show the validation and results of cosmological inference with the Emulator approach.

7.1 Neural Network

A Neural Network (NN) is usually comprised of an input layer, several hidden layers, and an output layer. Each layer has a certain number of nodes (or neurons), and each node of different layers is connected with *weights* and a nonlinear *activation function*. The key difference between a Neural Network and a simple linear algebra operation is that there exists a lot of algorithms designed for the Network to learn and improve with training data.

Some key ideas in training a Neural Network include *loss function*, *back-propagation*, and *stochastic gradient descent*. The proof of why the algorithm can "learn" from data is beyond the scope of this thesis. For a review, see [165].

For our use of machine learning in training an emulator, we use the standard algorithm for backpropagation and stochastic gradient descent, Adam Optimizer [166]. The main component we need to modify is the *loss function* and preprocessing of data. As we show in Sec. 7.2, these designs are made according to our knowledge of physics.

The Network Model we use is called Transformer [164], which is probably the most influential idea in machine learning in the past few years. As the name suggests, "Attention is all you need", the groundbreaking idea is to use a self-attention mechanism to replace complicated nonlinear functions. The self-attention has enough representational power in terms of non-linearities, such that it brings the community to reconsider "simple" models. Transformer is also the building block of ChatGPT [1]. The huge improvement when adding the TransformerBlock to existing architectures is what makes it widely used in a variety of deep learning problems.

7.2 Emulator Design

In this section, we summarize the pre-processing and hyperparameter choices. We start by emphasizing that, there is no one-fit-for-all choice in deep learning. The optimization process requires a lot of trials and experiments, but we hope a working example could help to build some intuition in designing a cosmology emulator.

7.2.1 Latin HyperCube

Latin HyperCube Sampling (LHS) is broadly used in emulator training due to its space-filling property. In a 2-D grid, the Latin Square fills the space if and only if there is one sample in each row and each column. Latin HyperCube

[1] https://openai.com/blog/chatgpt

generates this idea into multi-dimensions. An Orthonormal Sampling is a minimal extension to the LHS that ensures each subspace is sampled with the same density. In this work, we use PyODE [2] to sample the Latin hypercube on the full prior.

The validation is also performed over the entire prior, which greatly generalized the use of the emulator to not only the high-likelihood region. This is essential when the emulator is used not only around the fiducial point, such as doing tension calibration. Since a cube has a much larger volume, the required number of training points is also much larger. However, due to the fact that this computation is trivially parallelizable, the generation of training data vectors can be completed in a few hours.

We do not train the emulator with parameters that only give a linear addition or multiplication of the data vector. For 3x2pt we have multiplicative shear calibration acting on the data vector as:

$$\begin{aligned} \xi_{\pm}^{ij} &\to \left(1+m^i\right)\left(1+m^j\right)\xi_{\pm}^{ij} \\ \gamma_t^{ij} &\to \left(1+m^j\right)\gamma_t^{ij} \end{aligned} \tag{7.1}$$

and for linear galaxy bias:

$$\begin{aligned} w^i &\to b_{(i)}^2 w^i \\ \gamma_t^i &\to b_{(i)}\gamma_t. \end{aligned} \tag{7.2}$$

Thus, we can manually add these two systematics after the result given by the neural network. This greatly reduces the input dimension and makes the training much easier. However, we emphasize that linear galaxy bias b_i is $\mathcal{O}(1)$ parameter, and thus the error propagates to a larger value as the sampled bias is larger than the fiducial bias. For this reason, we only retain the sampling near the fiducial galaxy bias.

7.2.2 Loss Function and Data Pre-Processing

We define the loss function to be directly the average $\Delta\chi^2$ between Emulator and Cocoa:

$$L(\boldsymbol{w}) = \left\langle \left(\mathcal{D}_{\rm NN} - \mathcal{D}_{\rm model}\right) \mathbf{C}^{-1} \left(\mathcal{D}_{\rm NN} - \mathcal{D}_{\rm model}\right)^T \right\rangle, \tag{7.3}$$

which is the closest choice to the standard of whether the emulator is accurate enough. By taking into the covariance of the data vector, the emulator can be extra accurate for the data points with a small error bar, and can also be less accurate with more noisy data points.

[2] https://pythonhosted.org/pyDOE/index.html

The input parameters include cosmological parameters and astrophysical parameters of different magnitudes. We normalize them according to the prior range such that they are all between $[0, 1]$:

$$\tilde{\boldsymbol{\theta}} = \frac{\boldsymbol{\Theta} - \boldsymbol{\Theta}_{\rm min}}{\boldsymbol{\Theta}_{\rm max} - \boldsymbol{\Theta}_{\rm min}} \tag{7.4}$$

For the pre-processing of data vectors, we first make the change of basis:

$$\bar{\boldsymbol{y}} \to \boldsymbol{y}\mathbf{Q} \tag{7.5}$$

where $\mathbf{Q}$ is the eigenvectors of the covariance matrix:

$$\mathbf{C} \equiv \mathbf{Q}\boldsymbol{\Lambda}\mathbf{Q}^{-1} \tag{7.6}$$

we then normalize the data vector in the new basis as:

$$\mathcal{D} = \frac{\bar{\boldsymbol{y}} - \bar{\boldsymbol{y}}_{\rm mean}}{\sigma_y} \tag{7.7}$$

where $\bar{\boldsymbol{y}}_{\rm mean}$ is the mean of the data vectors and $\sigma_d = \sqrt{\rm diag[\mathbf{C}]}$ is the standard deviation.

This pre-processing of the data vector is equivalent to Cholesky decomposition. The two-step procedure makes the PCA truncation straightforward, but we keep all the principal components in this study. We find the above pre-processing of input and output data significantly increases the training accuracy.

7.2.3 Transformer: Attention is all you need

We use the state-of-the-art Nearaul Network design Transformer [164], which is also the building block of ChatGPT. We find this design gives orders of magnitude increase in performance, which allows us to train the 3x2pt data vector across the entire parameter space.

The transformer model is designed to address some of the limitations of recurrent neural networks (RNNs) and convolutional neural networks (CNNs) in processing sequential data, such as language and time series data, and in our case the emulation between cosmological parameters and data vectors. The key innovation of the transformer model is the self-attention mechanism. Self-attention is a way of computing a weighted sum of a sequence of input vectors, where the weights are determined by the similarity between each input vector and a query vector. The query vector is typically a learned parameter of the

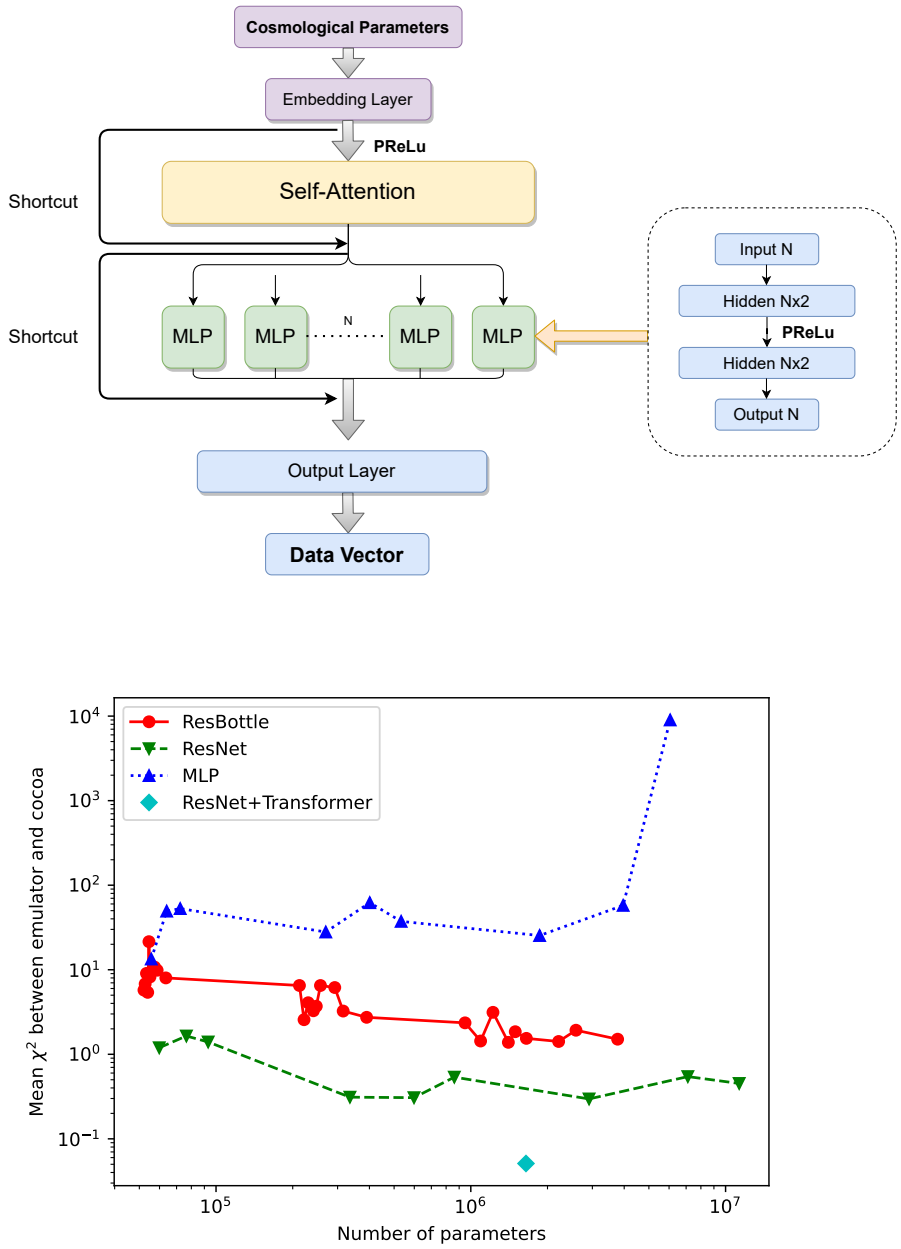


Figure 7.1: Architecture of the Neural Network using transformer block. *Upper panel*: In this work, our input dimension is 18 for LCDM and 20 for wCDM. The output dimension of the 3x2pt data vector is 1560. We use the 16 embedding vectors with each of them having a dimension of 128. The total trainable parameters are about 3.5 million. *Lower panel*: the comparison of different network designs for the tension metric calibration project. The x-axis is the total trainable parameters. The transformer block provides orders of magnitude increase in accuracy.

model. To compute the attention weights, the input sequence is transformed into three types of vectors: query vectors, key vectors, and value vectors. The query vectors are used to compute the similarity between each input vector and the query vector. The key vectors are used to represent the input vectors, and the value vectors are the vectors that will be weighted by the attention weights. The attention weights are computed by taking the dot product between the query vector and each key vector and then applying a softmax function to normalize the weights. The self-attention mechanism allows the transformer model to process sequential data more efficiently than RNNs and CNNs because it can capture long-range dependencies between elements of the sequence without requiring the computation of a large number of sequential operations. In our case, the long-range similarities between each tomographic bin are also well captured by this mechanism.

The design is plotted in Fig. 7.1. We use the 16 embedding vectors with each of them having a dimension of 128. The total trainable parameters are about 3.5 million. After the self-attention layer and the multi-head MLP layers, we also apply the layer norm, which is a generalization to the conventional batch norm. Again, we do not claim this architecture is the best for all emulators, but we do see a massive improvement over the residual network and fully connected MLP as used in previous emulator work [167, 168].

Besides using the original transformer block, we also find that self-attention can boost the accuracy of existing networks. In a work under preparation, we replace the embedding layer with three residual blocks. We find the self-attention mechanism allows us to train the emulator with a high temperature $T = 64$. This allows us to do the calibration of the tension metric with noise-injected data vectors. The comparison of different network models aiming for this problem is shown in Fig. 7.1.

7.3 Usage of the Emulator

7.3.1 Validations of the Emulator

The validation result is shown in Fig. 7.2. With 800,000 training points, we are able to reach the accuracy of $\chi^2 \approx 0.3$ after the standard scale cut. More significantly, the emulator can be used with the entire prior. This is tested with a shifted data vector as shown in the lower panel of Fig. 7.2. The shifted data vector with anisotropic stress is generated as described in Sec. 4.3.1.

The emulator dramatically saves the MCMC chain running time. A standard LSST-Y1 with CMB priors without a good parameter covariance to start with could take over a month, whereas the same MCMC chains with emulators

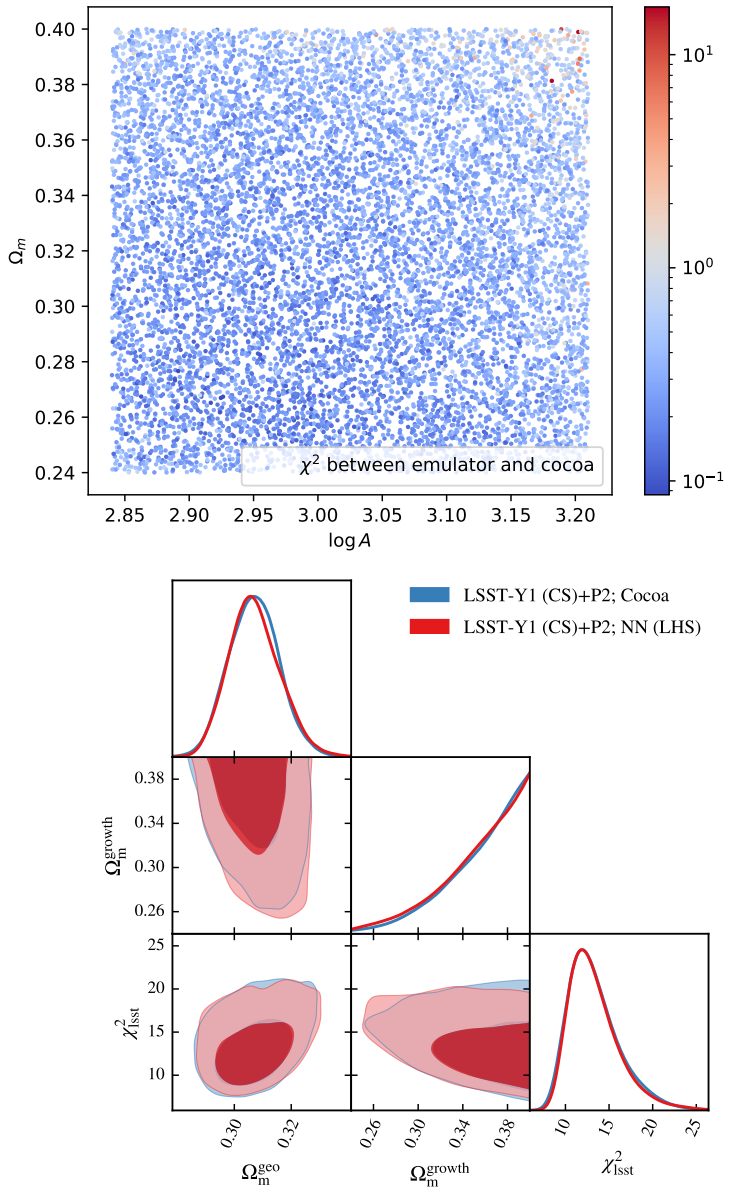


Figure 7.2: *Upper Panel*: The χ^2 difference between the emulator and CosmoLike. The average χ^2 is about 0.3 after the standard scale cut. *Lower Panel*: The posterior comparison of the MCMC chains using Emulator and Cocoa. As should be expected from the χ^2 plot, there is no difference even near the boundary of the prior range. Note that this is actually a less stringent test since even a larger χ^2 difference at each point could produce the same posterior distribution.

finished within two days. The difference in time is even larger when running the chains without external data since in that case we do not need to call the Boltzmann code.

7.3.2 Mapping the growth geometry split to other expansion history

In this section, we present an example where the investigation of such a problem is only possible with the help of an emulator.

The split formalism of growth and geometry probe is designed to test if geometry predicts growth as expected in ΛCDM and wCDM, and thus serve as a model-independent test of smooth dark energy paradigm. Given the split is performed only by assuming a constant dark energy equation of state, how would the growth parameters behave if the true underlying cosmology is with smooth but dynamic dark energy?

To answer this question, we create a mapping between split ΛCDM and non-split w0waCDM. The result is shown in Fig. 7.3. We first take a chain constraining $w_0 w_a$ cosmology with Planck2018+BAO+SNIa [2], then for each point, we generate a data vector. We run the minimizer assuming split growth and geometry but maintain $w = -1$ for each data vector. In this way, we quantize what is the limit of the split ΛCDM formalism if the underlying background evolution is $w_0 w_a$ instead of $w = -1$. The lower panel of Fig. 7.3 shows that the results are centered around the line of growth = geometry, and thus the formalism would not give a bias result even if we did not assume a correct background evolution.

More discussion of this mapping idea will be included in the paper to be published soon. Here we first discuss why the calculation is impossible without the help of the emulator. The 3x2pt calculation of Cocoa/Cosmolike could take up to 3 seconds. Each minimizer needs around 5000 evaluations with the Py-BOBYQA minimizer integrated in Cobaya. In order to make a plot that well describes the 2σ region, we need at least 5000 such minimizations. That together requires $3 \times 5000 \times 5000\,\mathrm{sec} = 868\mathrm{days}$. This is too slow, even with the help of MPI parallelization. With the help of the emulator, each evaluation is about 100 times faster, and we can easily finish the calculation within a day.

7.4 Discussion

The demand to create an emulator first came from the study of scale cut, which requires hundreds of MCMC chains [167]. The emulator trained there used an iterative method that requires much fewer points than we have. As a result,

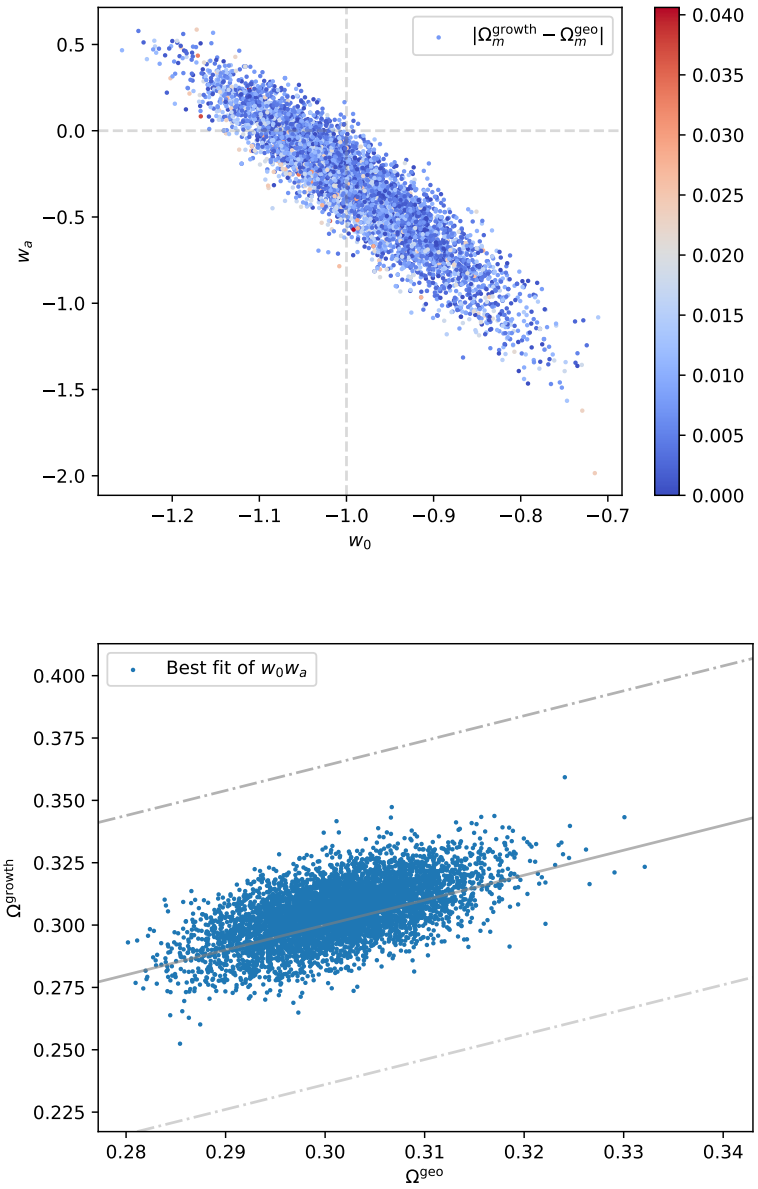


Figure 7.3: The mapping between w0wa cosmology and the split ΛCDM geometry and growth parameters. We do the minimizer for each point of the w0wa chain to find the maximum likelihood correspondence of the split parameters. The upper and lower panel shows the same result in different projections. The plot shows that even in the case we keep the $w = -1$ in studying the growth geometry split with the underlying cosmology to vary following w0wa, the formalism would not give significant detection of growth $\neq$ geometry.

the emulator can only be used within a small region near the center. For the study of tension metric, the noise injection could shift the contours well outside the validated region. We soon find that the state-of-the-art transformer model helps the training process dramatically and enables us to train the emulator for the entire parameter space.

However, we still face difficulties when the prior is too large. For example, we have not yet validated the emulator on the DES Δz prior, which is about 10 times larger than the LSST-Y1 prior. In that regard, the training strategy based on chain sampling with high temperatures can be generalized to more cases. Extra effort is still needed if the emulator is designed for real data, even if the emulator passes the above test. Since the posterior can shift well beyond the fiducial point, error propagation, like the galaxy bias, can be severe. A possible solution is to include these parameters in training as well. Although it may not be possible with the survey accuracy now, an emulator could be a helpful tool for future surveys that has a much more stringent prior on nuisance parameters and are more computationally difficult.

Bibliography

[1] Planck Collaboration, N. Aghanim, Y. Akrami, F. Arroja, M. Ashdown, J. Aumont, C. Baccigalupi, M. Ballardini, A. J. Banday, R. B. Barreiro, N. Bartolo, S. Basak, R. Battye, K. Benabed, J. P. Bernard, M. Bersanelli, P. Bielewicz, J. J. Bock, J. R. Bond, J. Borrill, F. R. Bouchet, F. Boulanger, M. Bucher, C. Burigana, R. C. Butler, E. Calabrese, J. F. Cardoso, J. Carron, B. Casaponsa, A. Challinor, H. C. Chiang, L. P. L. Colombo, C. Combet, D. Contreras, B. P. Crill, F. Cuttaia, P. de Bernardis, G. de Zotti, J. Delabrouille, J. M. Delouis, F. X. Désert, E. Di Valentino, C. Dickinson, J. M. Diego, S. Donzelli, O. Doré, M. Douspis, A. Ducout, X. Dupac, G. Efstathiou, F. Elsner, T. A. Enßlin, H. K. Eriksen, E. Falgarone, Y. Fantaye, J. Fergusson, R. Fernandez-Cobos, F. Finelli, F. Forastieri, M. Frailis, E. Franceschi, A. Frolov, S. Galeotta, S. Galli, K. Ganga, R. T. Génova-Santos, M. Gerbino, T. Ghosh, J. González-Nuevo, K. M. Górski, S. Gratton, A. Gruppuso, J. E. Gudmundsson, J. Hamann, W. Handley, F. K. Hansen, G. Helou, D. Herranz, S. R. Hildebrandt, E. Hivon, Z. Huang, A. H. Jaffe, W. C. Jones, A. Karakci, E. Keihänen, R. Keskitalo, K. Kiiveri, J. Kim, T. S. Kisner, L. Knox, N. Krachmalnicoff, M. Kunz, H. Kurki-Suonio, G. Lagache, J. M. Lamarre, M. Langer, A. Lasenby, M. Lattanzi, C. R. Lawrence, M. Le Jeune, J. P. Leahy, J. Lesgourgues, F. Levrier, A. Lewis, M. Liguori, P. B. Lilje, M. Lilley, V. Lindholm, M. López-Caniego, P. M. Lubin, Y. Z. Ma, J. F. Macías-Pérez, G. Maggio, D. Maino, N. Mandolesi, A. Mangilli, A. Marcos-Caballero, M. Maris, P. G. Martin, M. Martinelli, E. Martínez-González, S. Matarrese, N. Mauri, J. D. McEwen, P. D. Meerburg, P. R. Meinhold, A. Melchiorri, A. Mennella, M. Migliaccio, M. Millea, S. Mitra, M. A. Miville-Deschênes, D. Molinari, A. Moneti, L. Montier, G. Morgante, A. Moss, S. Mottet, M. Münchmeyer, P. Natoli, H. U. Nørgaard-Nielsen, C. A. Oxborrow, L. Pagano, D. Paoletti, B. Partridge, G. Patanchon, T. J. Pearson, M. Peel, H. V. Peiris, F. Perrotta, V. Pettorino, F. Piacentini, L. Polastri, G. Polenta, J. L. Puget, J. P. Rachen, M. Reinecke, M. Re-

mazeilles, C. Renault, A. Renzi, G. Rocha, C. Rosset, G. Roudier, J. A. Rubiño-Martín, B. Ruiz-Granados, L. Salvati, M. Sandri, M. Savelainen, D. Scott, E. P. S. Shellard, M. Shiraishi, C. Sirignano, G. Sirri, L. D. Spencer, R. Sunyaev, A. S. Suur-Uski, J. A. Tauber, D. Tavagnacco, M. Tenti, L. Terenzi, L. Toffolatti, M. Tomasi, T. Trombetti, J. Valiviita, B. Van Tent, L. Vibert, P. Vielva, F. Villa, N. Vittorio, B. D. Wandelt, I. K. Wehus, M. White, S. D. M. White, A. Zacchei, and A. Zonca. Planck 2018 results. I. Overview and the cosmological legacy of Planck. , 641:A1, September 2020. doi: 10.1051/0004-6361/201833880.

[2] Planck Collaboration, N. Aghanim, Y. Akrami, M. Ashdown, J. Aumont, C. Baccigalupi, M. Ballardini, A. J. Banday, R. B. Barreiro, N. Bartolo, S. Basak, R. Battye, K. Benabed, J. P. Bernard, M. Bersanelli, P. Bielewicz, J. J. Bock, J. R. Bond, J. Borrill, F. R. Bouchet, F. Boulanger, M. Bucher, C. Burigana, R. C. Butler, E. Calabrese, J. F. Cardoso, J. Carron, A. Challinor, H. C. Chiang, J. Chluba, L. P. L. Colombo, C. Combet, D. Contreras, B. P. Crill, F. Cuttaia, P. de Bernardis, G. de Zotti, J. Delabrouille, J. M. Delouis, E. Di Valentino, J. M. Diego, O. Doré, M. Douspis, A. Ducout, X. Dupac, S. Dusini, G. Efstathiou, F. Elsner, T. A. Enßlin, H. K. Eriksen, Y. Fantaye, M. Farhang, J. Fergusson, R. Fernandez-Cobos, F. Finelli, F. Forastieri, M. Frailis, A. A. Fraisse, E. Franceschi, A. Frolov, S. Galeotta, S. Galli, K. Ganga, R. T. Génova-Santos, M. Gerbino, T. Ghosh, J. González-Nuevo, K. M. Górski, S. Gratton, A. Gruppuso, J. E. Gudmundsson, J. Hamann, W. Handley, F. K. Hansen, D. Herranz, S. R. Hildebrandt, E. Hivon, Z. Huang, A. H. Jaffe, W. C. Jones, A. Karakci, E. Keihänen, R. Keskitalo, K. Kiiveri, J. Kim, T. S. Kisner, L. Knox, N. Krachmalnicoff, M. Kunz, H. Kurki-Suonio, G. Lagache, J. M. Lamarre, A. Lasenby, M. Lattanzi, C. R. Lawrence, M. Le Jeune, P. Lemos, J. Lesgourgues, F. Levrier, A. Lewis, M. Liguori, P. B. Lilje, M. Lilley, V. Lindholm, M. López-Caniego, P. M. Lubin, Y. Z. Ma, J. F. Macías-Pérez, G. Maggio, D. Maino, N. Mandolesi, A. Mangilli, A. Marcos-Caballero, M. Maris, P. G. Martin, M. Martinelli, E. Martínez-González, S. Matarrese, N. Mauri, J. D. McEwen, P. R. Meinhold, A. Melchiorri, A. Mennella, M. Migliaccio, M. Millea, S. Mitra, M. A. Miville-Deschênes, D. Molinari, L. Montier, G. Morgante, A. Moss, P. Natoli, H. U. Nørgaard-Nielsen, L. Pagano, D. Paoletti, B. Partridge, G. Patanchon, H. V. Peiris, F. Perrotta, V. Pettorino, F. Piacentini, L. Polastri, G. Polenta, J. L. Puget, J. P. Rachen, M. Reinecke, M. Remazeilles, A. Renzi, G. Rocha, C. Rosset, G. Roudier, J. A. Rubiño-Martín, B. Ruiz-Granados, L. Salvati, M. Sandri, M. Savelainen,

D. Scott, E. P. S. Shellard, C. Sirignano, G. Sirri, L. D. Spencer, R. Sunyaev, A. S. Suur-Uski, J. A. Tauber, D. Tavagnacco, M. Tenti, L. Toffolatti, M. Tomasi, T. Trombetti, L. Valenziano, J. Valiviita, B. Van Tent, L. Vibert, P. Vielva, F. Villa, N. Vittorio, B. D. Wandelt, I. K. Wehus, M. White, S. D. M. White, A. Zacchei, and A. Zonca. Planck 2018 results. VI. Cosmological parameters. , 641:A6, September 2020. doi: 10.1051/0004-6361/201833910.

[3] B. Flaugher, H. T. Diehl, K. Honscheid, T. M. C. Abbott, O. Alvarez, R. Angstadt, J. T. Annis, M. Antonik, O. Ballester, L. Beaufore, G. M. Bernstein, R. A. Bernstein, B. Bigelow, M. Bonati, D. Boprie, D. Brooks, E. J. Buckley-Geer, J. Campa, L. Cardiel-Sas, F. J. Castander, J. Castilla, H. Cease, J. M. Cela-Ruiz, S. Chappa, E. Chi, C. Cooper, L. N. da Costa, E. Dede, G. Derylo, D. L. DePoy, J. de Vicente, P. Doel, A. Drlica-Wagner, J. Eiting, A. E. Elliott, J. Emes, J. Estrada, A. Fausti Neto, D. A. Finley, R. Flores, J. Frieman, D. Gerdes, M. D. Gladders, B. Gregory, G. R. Gutierrez, J. Hao, S. E. Holland, S. Holm, D. Huffman, C. Jackson, D. J. James, M. Jonas, A. Karcher, I. Karliner, S. Kent, R. Kessler, M. Kozlovsky, R. G. Kron, D. Kubik, K. Kuehn, S. Kuhlmann, K. Kuk, O. Lahav, A. Lathrop, J. Lee, M. E. Levi, P. Lewis, T. S. Li, I. Mandrichenko, J. L. Marshall, G. Martinez, K. W. Merritt, R. Miquel, F. Muñoz, E. H. Neilsen, R. C. Nichol, B. Nord, R. Ogando, J. Olsen, N. Palaio, K. Patton, J. Peoples, A. A. Plazas, J. Rauch, K. Reil, J. P. Rheault, N. A. Roe, H. Rogers, A. Roodman, E. Sanchez, V. Scarpine, R. H. Schindler, R. Schmidt, R. Schmitt, M. Schubnell, K. Schultz, P. Schurter, L. Scott, S. Serrano, T. M. Shaw, R. C. Smith, M. Soares-Santos, A. Stefanik, W. Stuermer, E. Suchyta, A. Sypniewski, G. Tarle, J. Thaler, R. Tighe, C. Tran, D. Tucker, A. R. Walker, G. Wang, M. Watson, C. Weaverdyck, W. Wester, R. Woods, B. Yanny, and DES Collaboration. The Dark Energy Camera. , 150(5):150, November 2015. doi: 10.1088/0004-6256/150/5/150.

[4] Dark Energy Survey Collaboration, T. Abbott, F. B. Abdalla, J. Aleksić, S. Allam, A. Amara, D. Bacon, E. Balbinot, M. Banerji, K. Bechtol, A. Benoit-Lévy, G. M. Bernstein, E. Bertin, J. Blazek, C. Bonnett, S. Bridle, D. Brooks, R. J. Brunner, E. Buckley-Geer, D. L. Burke, G. B. Caminha, D. Capozzi, J. Carlsen, A. Carnero-Rosell, M. Carollo, M. Carrasco-Kind, J. Carretero, F. J. Castander, L. Clerkin, T. Collett, C. Conselice, M. Crocce, C. E. Cunha, C. B. D'Andrea, L. N. da Costa, T. M. Davis, S. Desai, H. T. Diehl, J. P. Dietrich, S. Dodelson, P. Doel,

A. Drlica-Wagner, J. Estrada, J. Etherington, A. E. Evrard, J. Fabbri, D. A. Finley, B. Flaugher, R. J. Foley, P. Fosalba, J. Frieman, J. García-Bellido, E. Gaztanaga, D. W. Gerdes, T. Giannantonio, D. A. Goldstein, D. Gruen, R. A. Gruendl, P. Guarnieri, G. Gutierrez, W. Hartley, K. Honscheid, B. Jain, D. J. James, T. Jeltema, S. Jouvel, R. Kessler, A. King, D. Kirk, R. Kron, K. Kuehn, N. Kuropatkin, O. Lahav, T. S. Li, M. Lima, H. Lin, M. A. G. Maia, M. Makler, M. Manera, C. Maraston, J. L. Marshall, P. Martini, R. G. McMahon, P. Melchior, A. Merson, C. J. Miller, R. Miquel, J. J. Mohr, X. Morice-Atkinson, K. Naidoo, E. Neilsen, R. C. Nichol, B. Nord, R. Ogando, F. Ostrovski, A. Palmese, A. Papadopoulos, H. V. Peiris, J. Peoples, W. J. Percival, A. A. Plazas, S. L. Reed, A. Refregier, A. K. Romer, A. Roodman, A. Ross, E. Rozo, E. S. Rykoff, I. Sadeh, M. Sako, C. Sánchez, E. Sanchez, B. Santiago, V. Scarpine, M. Schubnell, I. Sevilla-Noarbe, E. Sheldon, M. Smith, R. C. Smith, M. Soares-Santos, F. Sobreira, M. Soumagnac, E. Suchyta, M. Sullivan, M. Swanson, G. Tarle, J. Thaler, D. Thomas, R. C. Thomas, D. Tucker, J. D. Vieira, V. Vikram, A. R. Walker, R. H. Wechsler, J. Weller, W. Wester, L. Whiteway, H. Wilcox, B. Yanny, Y. Zhang, and J. Zuntz. The Dark Energy Survey: more than dark energy - an overview. , 460(2):1270–1299, August 2016. doi: 10.1093/mnras/stw641.

[5] T. M. C. Abbott, F. B. Abdalla, A. Alarcon, J. Aleksić, S. Allam, S. Allen, A. Amara, J. Annis, J. Asorey, S. Avila, D. Bacon, E. Balbinot, M. Banerji, N. Banik, W. Barkhouse, M. Baumer, E. Baxter, K. Bechtol, M. R. Becker, A. Benoit-Lévy, B. A. Benson, G. M. Bernstein, E. Bertin, J. Blazek, S. L. Bridle, D. Brooks, D. Brout, E. Buckley-Geer, D. L. Burke, M. T. Busha, A. Campos, D. Capozzi, A. Carnero Rosell, M. Carrasco Kind, J. Carretero, F. J. Castander, R. Cawthon, C. Chang, N. Chen, M. Childress, A. Choi, C. Conselice, R. Crittenden, M. Crocce, C. E. Cunha, C. B. D'Andrea, L. N. da Costa, R. Das, T. M. Davis, C. Davis, J. De Vicente, D. L. DePoy, J. DeRose, S. Desai, H. T. Diehl, J. P. Dietrich, S. Dodelson, P. Doel, A. Drlica-Wagner, T. F. Eifler, A. E. Elliott, F. Elsner, J. Elvin-Poole, J. Estrada, A. E. Evrard, Y. Fang, E. Fernandez, A. Ferté, D. A. Finley, B. Flaugher, P. Fosalba, O. Friedrich, J. Frieman, J. García-Bellido, M. Garcia-Fernandez, M. Gatti, E. Gaztanaga, D. W. Gerdes, T. Giannantonio, M. S. S. Gill, K. Glazebrook, D. A. Goldstein, D. Gruen, R. A. Gruendl, J. Gschwend, G. Gutierrez, S. Hamilton, W. G. Hartley, S. R. Hinton, K. Honscheid, B. Hoyle, D. Huterer, B. Jain, D. J. James, M. Jarvis, T. Jeltema, M. D. Johnson, M. W. G. Johnson, T. Kacprzak, S. Kent, A. G. Kim, A. King, D. Kirk, N. Kokron, A. Kovacs, E. Krause, C. Krawiec, A. Kremin,

K. Kuehn, S. Kuhlmann, N. Kuropatkin, F. Lacasa, O. Lahav, T. S. Li, A. R. Liddle, C. Lidman, M. Lima, H. Lin, N. MacCrann, M. A. G. Maia, M. Makler, M. Manera, M. March, J. L. Marshall, P. Martini, R. G. McMahon, P. Melchior, F. Menanteau, R. Miquel, V. Miranda, D. Mudd, J. Muir, A. Möller, E. Neilsen, R. C. Nichol, B. Nord, P. Nugent, R. L. C. Ogando, A. Palmese, J. Peacock, H. V. Peiris, J. Peoples, W. J. Percival, D. Petravick, A. A. Plazas, A. Porredon, J. Prat, A. Pujol, M. M. Rau, A. Refregier, P. M. Ricker, N. Roe, R. P. Rollins, A. K. Romer, A. Roodman, R. Rosenfeld, A. J. Ross, E. Rozo, E. S. Rykoff, M. Sako, A. I. Salvador, S. Samuroff, C. Sánchez, E. Sanchez, B. Santiago, V. Scarpine, R. Schindler, D. Scolnic, L. F. Secco, S. Serrano, I. Sevilla-Noarbe, E. Sheldon, R. C. Smith, M. Smith, J. Smith, M. Soares-Santos, F. Sobreira, E. Suchyta, G. Tarle, D. Thomas, M. A. Troxel, D. L. Tucker, B. E. Tucker, S. A. Uddin, T. N. Varga, P. Vielzeuf, V. Vikram, A. K. Vivas, A. R. Walker, M. Wang, R. H. Wechsler, J. Weller, W. Wester, R. C. Wolf, B. Yanny, F. Yuan, A. Zenteno, B. Zhang, Y. Zhang, J. Zuntz, and Dark Energy Survey Collaboration. Dark Energy Survey year 1 results: Cosmological constraints from galaxy clustering and weak lensing. , 98 (4):043526, August 2018. doi: 10.1103/PhysRevD.98.043526.

[6] T. M. C. Abbott, M. Aguena, A. Alarcon, S. Allam, O. Alves, A. Amon, F. Andrade-Oliveira, J. Annis, S. Avila, D. Bacon, E. Baxter, K. Bechtol, M. R. Becker, G. M. Bernstein, S. Bhargava, S. Birrer, J. Blazek, A. Brandao-Souza, S. L. Bridle, D. Brooks, E. Buckley-Geer, D. L. Burke, H. Camacho, A. Campos, A. Carnero Rosell, M. Carrasco Kind, J. Carretero, F. J. Castander, R. Cawthon, C. Chang, A. Chen, R. Chen, A. Choi, C. Conselice, J. Cordero, M. Costanzi, M. Crocce, L. N. da Costa, M. E. da Silva Pereira, C. Davis, T. M. Davis, J. De Vicente, J. DeRose, S. Desai, E. Di Valentino, H. T. Diehl, J. P. Dietrich, S. Dodelson, P. Doel, C. Doux, A. Drlica-Wagner, K. Eckert, T. F. Eifler, F. Elsner, J. Elvin-Poole, S. Everett, A. E. Evrard, X. Fang, A. Farahi, E. Fernandez, I. Ferrero, A. Ferté, P. Fosalba, O. Friedrich, J. Frieman, J. García-Bellido, M. Gatti, E. Gaztanaga, D. W. Gerdes, T. Giannantonio, G. Giannini, D. Gruen, R. A. Gruendl, J. Gschwend, G. Gutierrez, I. Harrison, W. G. Hartley, K. Herner, S. R. Hinton, D. L. Hollowood, K. Honscheid, B. Hoyle, E. M. Huff, D. Huterer, B. Jain, D. J. James, M. Jarvis, N. Jeffrey, T. Jeltema, A. Kovacs, E. Krause, R. Kron, K. Kuehn, N. Kuropatkin, O. Lahav, P. F. Leget, P. Lemos, A. R. Liddle, C. Lidman, M. Lima, H. Lin, N. MacCrann, M. A. G. Maia, J. L. Marshall, P. Martini, J. McCullough, P. Melchior, J. Mena-Fernández, F. Menanteau, R. Miquel, J. J. Mohr, R. Morgan,

J. Muir, J. Myles, S. Nadathur, A. Navarro-Alsina, R. C. Nichol, R. L. C. Ogando, Y. Omori, A. Palmese, S. Pandey, Y. Park, F. Paz-Chinchón, D. Petravick, A. Pieres, A. A. Plazas Malagón, A. Porredon, J. Prat, M. Raveri, M. Rodriguez-Monroy, R. P. Rollins, A. K. Romer, A. Roodman, R. Rosenfeld, A. J. Ross, E. S. Rykoff, S. Samuroff, C. Sánchez, E. Sanchez, J. Sanchez, D. Sanchez Cid, V. Scarpine, M. Schubnell, D. Scolnic, L. F. Secco, S. Serrano, I. Sevilla-Noarbe, E. Sheldon, T. Shin, M. Smith, M. Soares-Santos, E. Suchyta, M. E. C. Swanson, M. Tabbutt, G. Tarle, D. Thomas, C. To, A. Troja, M. A. Troxel, D. L. Tucker, I. Tutusaus, T. N. Varga, A. R. Walker, N. Weaverdyck, R. Wechsler, J. Weller, B. Yanny, B. Yin, Y. Zhang, J. Zuntz, and DES Collaboration. Dark Energy Survey Year 3 results: Cosmological constraints from galaxy clustering and weak lensing. , 105(2):023520, January 2022. doi: 10.1103/PhysRevD.105.023520.

[7] Konrad Kuijken, Catherine Heymans, Hendrik Hildebrandt, Reiko Nakajima, Thomas Erben, Jelte T. A. de Jong, Massimo Viola, Ami Choi, Henk Hoekstra, Lance Miller, Edo van Uitert, Alexandra Amon, Chris Blake, Margot Brouwer, Axel Buddendiek, Ian Fenech Conti, Martin Eriksen, Aniello Grado, Joachim Harnois-Déraps, Ewout Helmich, Ricardo Herbonnet, Nancy Irisarri, Thomas Kitching, Dominik Klaes, Francesco La Barbera, Nicola Napolitano, Mario Radovich, Peter Schneider, Cristóbal Sifón, Gert Sikkema, Patrick Simon, Alexandru Tudorica, Edwin Valentijn, Gijs Verdoes Kleijn, and Ludovic van Waerbeke. Gravitational lensing analysis of the Kilo-Degree Survey. , 454(4):3500–3532, December 2015. doi: 10.1093/mnras/stv2140.

[8] Catherine Heymans, Tilman Tröster, Marika Asgari, Chris Blake, Hendrik Hildebrandt, Benjamin Joachimi, Konrad Kuijken, Chieh-An Lin, Ariel G. Sánchez, Jan Luca van den Busch, Angus H. Wright, Alexandra Amon, Maciej Bilicki, Jelte de Jong, Martin Crocce, Andrej Dvornik, Thomas Erben, Maria Cristina Fortuna, Fedor Getman, Benjamin Giblin, Karl Glazebrook, Henk Hoekstra, Shahab Joudaki, Arun Kannawadi, Fabian Köhlinger, Chris Lidman, Lance Miller, Nicola R. Napolitano, David Parkinson, Peter Schneider, HuanYuan Shan, Edwin A. Valentijn, Gijs Verdoes Kleijn, and Christian Wolf. KiDS-1000 Cosmology: Multi-probe weak gravitational lensing and spectroscopic galaxy clustering constraints. , 646:A140, February 2021. doi: 10.1051/0004-6361/202039063.

[9] Chiaki Hikage, Masamune Oguri, Takashi Hamana, Surhud More, Rachel Mandelbaum, Masahiro Takada, Fabian Köhlinger, Hironao Miyatake, Atsushi J. Nishizawa, Hiroaki Aihara, Robert Armstrong, James

Bosch, Jean Coupon, Anne Ducout, Paul Ho, Bau-Ching Hsieh, Yutaka Komiyama, François Lanusse, Alexie Leauthaud, Robert H. Lupton, Elinor Medezinski, Sogo Mineo, Shoken Miyama, Satoshi Miyazaki, Ryoma Murata, Hitoshi Murayama, Masato Shirasaki, Cristóbal Sifón, Melanie Simet, Joshua Speagle, David N. Spergel, Michael A. Strauss, Naoshi Sugiyama, Masayuki Tanaka, Yousuke Utsumi, Shiang-Yu Wang, and Yoshihiko Yamada. Cosmology from cosmic shear power spectra with Subaru Hyper Suprime-Cam first-year data. , 71(2):43, April 2019. doi: 10.1093/pasj/psz010.

[10] Hiroaki Aihara, Nobuo Arimoto, Robert Armstrong, Stéphane Arnouts, Neta A. Bahcall, Steven Bickerton, James Bosch, Kevin Bundy, Peter L. Capak, James H. H. Chan, Masashi Chiba, Jean Coupon, Eiichi Egami, Motohiro Enoki, Francois Finet, Hiroki Fujimori, Seiji Fujimoto, Hisanori Furusawa, Junko Furusawa, Tomotsugu Goto, Andy Goulding, Johnny P. Greco, Jenny E. Greene, James E. Gunn, Takashi Hamana, Yuichi Harikane, Yasuhiro Hashimoto, Takashi Hattori, Masao Hayashi, Yusuke Hayashi, Krzysztof G. Hełminiak, Ryo Higuchi, Chiaki Hikage, Paul T. P. Ho, Bau-Ching Hsieh, Kuiyun Huang, Song Huang, Hiroyuki Ikeda, Masatoshi Imanishi, Akio K. Inoue, Kazushi Iwasawa, Ikuru Iwata, Anton T. Jaelani, Hung-Yu Jian, Yukiko Kamata, Hiroshi Karoji, Nobunari Kashikawa, Nobuhiko Katayama, Satoshi Kawanomoto, Issha Kayo, Jin Koda, Michitaro Koike, Takashi Kojima, Yutaka Komiyama, Akira Konno, Shintaro Koshida, Yusei Koyama, Haruka Kusakabe, Alexie Leauthaud, Chien-Hsiu Lee, Lihwai Lin, Yen-Ting Lin, Robert H. Lupton, Rachel Mandelbaum, Yoshiki Matsuoka, Elinor Medezinski, Sogo Mineo, Shoken Miyama, Hironao Miyatake, Satoshi Miyazaki, Rieko Momose, Anupreeta More, Surhud More, Yuki Moritani, Takashi J. Moriya, Tomoki Morokuma, Shiro Mukae, Ryoma Murata, Hitoshi Murayama, Tohru Nagao, Fumiaki Nakata, Mana Niida, Hiroko Niikura, Atsushi J. Nishizawa, Yoshiyuki Obuchi, Masamune Oguri, Yukie Oishi, Nobuhiro Okabe, Sakurako Okamoto, Yuki Okura, Yoshiaki Ono, Masato Onodera, Masafusa Onoue, Ken Osato, Masami Ouchi, Paul A. Price, Tae-Soo Pyo, Masao Sako, Marcin Sawicki, Takatoshi Shibuya, Kazuhiro Shimasaku, Atsushi Shimono, Masato Shirasaki, John D. Silverman, Melanie Simet, Joshua Speagle, David N. Spergel, Michael A. Strauss, Yuma Sugahara, Naoshi Sugiyama, Yasushi Suto, Sherry H. Suyu, Nao Suzuki, Philip J. Tait, Masahiro Takada, Tadafumi Takata, Naoyuki Tamura, Manobu M. Tanaka, Masaomi Tanaka, Masayuki Tanaka, Yoko Tanaka, Tsuyoshi Terai, Yuichi Terashima, Yoshiki Toba, Nozomu Tominaga, Jun Toshikawa, Ed-

win L. Turner, Tomohisa Uchida, Hisakazu Uchiyama, Keiichi Umetsu, Fumihiro Uraguchi, Yuji Urata, Tomonori Usuda, Yousuke Utsumi, Shiang-Yu Wang, Wei-Hao Wang, Kenneth C. Wong, Kiyoto Yabe, Yoshihiko Yamada, Hitomi Yamanoi, Naoki Yasuda, Sherry Yeh, Atsunori Yonehara, and Suraphong Yuma. The Hyper Suprime-Cam SSP Survey: Overview and survey design. , 70:S4, January 2018. doi: 10.1093/pasj/psx066.

[11] Takashi Hamana, Masato Shirasaki, Satoshi Miyazaki, Chiaki Hikage, Masamune Oguri, Surhud More, Robert Armstrong, Alexie Leauthaud, Rachel Mandelbaum, Hironao Miyatake, Atsushi J. Nishizawa, Melanie Simet, Masahiro Takada, Hiroaki Aihara, James Bosch, Yutaka Komiyama, Robert Lupton, Hitoshi Murayama, Michael A. Strauss, and Masayuki Tanaka. Cosmological constraints from cosmic shear two-point correlation functions with HSC survey first-year data. , 72(1):16, February 2020. doi: 10.1093/pasj/psz138.

[12] Kyle S. Dawson, Jean-Paul Kneib, Will J. Percival, Shadab Alam, Franco D. Albareti, Scott F. Anderson, Eric Armengaud, Éric Aubourg, Stephen Bailey, Julian E. Bautista, Andreas A. Berlind, Matthew A. Bershady, Florian Beutler, Dmitry Bizyaev, Michael R. Blanton, Michael Blomqvist, Adam S. Bolton, Jo Bovy, W. N. Brandt, Jon Brinkmann, Joel R. Brownstein, Etienne Burtin, N. G. Busca, Zheng Cai, Chia-Hsun Chuang, Nicolas Clerc, Johan Comparat, Frances Cope, Rupert A. C. Croft, Irene Cruz-Gonzalez, Luiz N. da Costa, Marie-Claude Cousinou, Jeremy Darling, Axel de la Macorra, Sylvain de la Torre, Timothée Delubac, Hélion du Mas des Bourboux, Tom Dwelly, Anne Ealet, Daniel J. Eisenstein, Michael Eracleous, S. Escoffier, Xiaohui Fan, Alexis Finoguenov, Andreu Font-Ribera, Peter Frinchaboy, Patrick Gaulme, Antonis Georgakakis, Paul Green, Hong Guo, Julien Guy, Shirley Ho, Diana Holder, Joe Huehnerhoff, Timothy Hutchinson, Yipeng Jing, Eric Jullo, Vikrant Kamble, Karen Kinemuchi, David Kirkby, Francisco-Shu Kitaura, Mark A. Klaene, Russ R. Laher, Dustin Lang, Pierre Laurent, Jean-Marc Le Goff, Cheng Li, Yu Liang, Marcos Lima, Qiufan Lin, Weipeng Lin, Yen-Ting Lin, Daniel C. Long, Britt Lundgren, Nicholas MacDonald, Marcio Antonio Geimba Maia, Elena Malanushenko, Viktor Malanushenko, Vivek Mariappan, Cameron K. McBride, Ian D. McGreer, Brice Ménard, Andrea Merloni, Andres Meza, Antonio D. Montero-Dorta, Demitri Muna, Adam D. Myers, Kirpal Nandra, Tracy Naugle, Jeffrey A. Newman, Pasquier Noterdaeme, Peter Nugent, Ricardo Ogando, Matthew D. Olmstead, Audrey Oravetz, Daniel J.

Oravetz, Nikhil Padmanabhan, Nathalie Palanque-Delabrouille, Kaike Pan, John K. Parejko, Isabelle Pâris, John A. Peacock, Patrick Petitjean, Matthew M. Pieri, Alice Pisani, Francisco Prada, Abhishek Prakash, Anand Raichoor, Beth Reid, James Rich, Jethro Ridl, Sergio Rodriguez-Torres, Aurelio Carnero Rosell, Ashley J. Ross, Graziano Rossi, John Ruan, Mara Salvato, Conor Sayres, Donald P. Schneider, David J. Schlegel, Uros Seljak, Hee-Jong Seo, Branimir Sesar, Sarah Shandera, Yiping Shu, Anže Slosar, Flavia Sobreira, Alina Streblyanska, Nao Suzuki, Donna Taylor, Charling Tao, Jeremy L. Tinker, Rita Tojeiro, Mariana Vargas-Magaña, Yuting Wang, Benjamin A. Weaver, David H. Weinberg, Martin White, W. M. Wood-Vasey, Christophe Yeche, Zhongxu Zhai, Cheng Zhao, Gong-bo Zhao, Zheng Zheng, Guangtun Ben Zhu, and Hu Zou. The SDSS-IV Extended Baryon Oscillation Spectroscopic Survey: Overview and Early Data. , 151(2):44, February 2016. doi: 10.3847/0004-6256/151/2/44.

[13] Steven Weinberg. The Cosmological Constant Problem. *Rev. Mod. Phys.*, 61:1–23, 1989. doi: 10.1103/RevModPhys.61.1.

[14] R. R. Caldwell, Rahul Dave, and Paul J. Steinhardt. Cosmological imprint of an energy component with general equation of state. *Phys. Rev. Lett.*, 80:1582–1585, 1998. doi: 10.1103/PhysRevLett.80.1582.

[15] C. Armendariz-Picon, V. Mukhanov, and Paul J. Steinhardt. Essentials ofk-essence. *Physical Review D*, 63(10), Apr 2001. ISSN 1089-4918. doi: 10.1103/physrevd.63.103510. URL `http://dx.doi.org/10.1103/PhysRevD.63.103510`.

[16] Adam G. Riess, Wenlong Yuan, Lucas M. Macri, Dan Scolnic, Dillon Brout, Stefano Casertano, David O. Jones, Yukei Murakami, Gagandeep S. Anand, Louise Breuval, Thomas G. Brink, Alexei V. Filippenko, Samantha Hoffmann, Saurabh W. Jha, W. D'arcy Kenworthy, John Mackenty, Benjamin E. Stahl, and WeiKang Zheng. A Comprehensive Measurement of the Local Value of the Hubble Constant with 1 km s^{-1} Mpc^{-1} Uncertainty from the Hubble Space Telescope and the SH0ES Team. , 934(1):L7, July 2022. doi: 10.3847/2041-8213/ac5c5b.

[17] S. Joudaki, H. Hildebrandt, D. Traykova, N. E. Chisari, C. Heymans, A. Kannawadi, K. Kuijken, A. H. Wright, M. Asgari, T. Erben, H. Hoekstra, B. Joachimi, L. Miller, T. Tröster, and J. L. van den Busch. KiDS+VIKING-450 and DES-Y1 combined: Cosmology with cosmic shear. , 638:L1, June 2020. doi: 10.1051/0004-6361/201936154.

[18] Shadab Alam, Marie Aubert, Santiago Avila, Christophe Balland, Julian E. Bautista, Matthew A. Bershady, Dmitry Bizyaev, Michael R. Blanton, Adam S. Bolton, Jo Bovy, Jonathan Brinkmann, Joel R. Brownstein, Etienne Burtin, Solène Chabanier, Michael J. Chapman, Peter Doohyun Choi, Chia-Hsun Chuang, Johan Comparat, Marie-Claude Cousinou, Andrei Cuceu, Kyle S. Dawson, Sylvain de la Torre, Arnaud de Mattia, Victoria de Sainte Agathe, Hélion du Mas des Bourboux, Stephanie Escoffier, Thomas Etourneau, James Farr, Andreu Font-Ribera, Peter M. Frinchaboy, Sebastien Fromenteau, Héctor Gil-Marín, Jean-Marc Le Goff, Alma X. Gonzalez-Morales, Violeta Gonzalez-Perez, Kathleen Grabowski, Julien Guy, Adam J. Hawken, Jiamin Hou, Hui Kong, James Parker, Mark Klaene, Jean-Paul Kneib, Sicheng Lin, Daniel Long, Brad W. Lyke, Axel de la Macorra, Paul Martini, Karen Masters, Faizan G. Mohammad, Jeongin Moon, Eva-Maria Mueller, Andrea Muñoz-Gutiérrez, Adam D. Myers, Seshadri Nadathur, Richard Neveux, Jeffrey A. Newman, Pasquier Noterdaeme, Audrey Oravetz, Daniel Oravetz, Nathalie Palanque-Delabrouille, Kaike Pan, Romain Paviot, Will J. Percival, Ignasi Pérez-Ràfols, Patrick Petitjean, Matthew M. Pieri, Abhishek Prakash, Anand Raichoor, Corentin Ravoux, Mehdi Rezaie, James Rich, Ashley J. Ross, Graziano Rossi, Rossana Ruggeri, Vanina Ruhlmann-Kleider, Ariel G. Sánchez, F. Javier Sánchez, José R. Sánchez-Gallego, Conor Sayres, Donald P. Schneider, Hee-Jong Seo, Arman Shafieloo, Anže Slosar, Alex Smith, Julianna Stermer, Amelie Tamone, Jeremy L. Tinker, Rita Tojeiro, Mariana Vargas-Magaña, Andrei Variu, Yuting Wang, Benjamin A. Weaver, Anne-Marie Weijmans, Christophe Yèche, Pauline Zarrouk, Cheng Zhao, Gong-Bo Zhao, and Zheng Zheng. Completed SDSS-IV extended Baryon Oscillation Spectroscopic Survey: Cosmological implications from two decades of spectroscopic surveys at the Apache Point Observatory. , 103(8):083533, April 2021. doi: 10.1103/PhysRevD.103.083533.

[19] Adam B. Mantz, Anja von der Linden, Steven W. Allen, Douglas E. Applegate, Patrick L. Kelly, R. Glenn Morris, David A. Rapetti, Robert W. Schmidt, Saroj Adhikari, Mark T. Allen, Patricia R. Burchat, David L. Burke, Matteo Cataneo, David Donovan, Harald Ebeling, Sarah Shandera, and Adam Wright. Weighing the giants - IV. Cosmology and neutrino mass. , 446(3):2205–2225, January 2015. doi: 10.1093/mnras/stu2096.

[20] E. J. Groth and P. J. E. Peebles. Statistical analysis of catalogs of extragalactic objects. VII. Two- and three-point correlation functions

for the high-resolution Shane-Wirtanen catalog of galaxies. , 217:385–405, October 1977. doi: 10.1086/155588.

[21] J. Elvin-Poole, M. Crocce, A. J. Ross, T. Giannantonio, E. Rozo, E. S. Rykoff, S. Avila, N. Banik, J. Blazek, S. L. Bridle, R. Cawthon, A. Drlica-Wagner, O. Friedrich, N. Kokron, E. Krause, N. MacCrann, J. Prat, C. Sánchez, L. F. Secco, I. Sevilla-Noarbe, M. A. Troxel, T. M. C. Abbott, F. B. Abdalla, S. Allam, J. Annis, J. Asorey, K. Bechtol, M. R. Becker, A. Benoit-Lévy, G. M. Bernstein, E. Bertin, D. Brooks, E. Buckley-Geer, D. L. Burke, A. Carnero Rosell, D. Carollo, M. Carrasco Kind, J. Carretero, F. J. Castander, C. E. Cunha, C. B. D'Andrea, L. N. da Costa, T. M. Davis, C. Davis, S. Desai, H. T. Diehl, J. P. Dietrich, S. Dodelson, P. Doel, T. F. Eifler, A. E. Evrard, E. Fernandez, B. Flaugher, P. Fosalba, J. Frieman, J. García-Bellido, E. Gaztanaga, D. W. Gerdes, K. Glazebrook, D. Gruen, R. A. Gruendl, J. Gschwend, G. Gutierrez, W. G. Hartley, S. R. Hinton, K. Honscheid, J. K. Hoormann, B. Jain, D. J. James, M. Jarvis, T. Jeltema, M. W. G. Johnson, M. D. Johnson, A. King, K. Kuehn, S. Kuhlmann, N. Kuropatkin, O. Lahav, G. Lewis, T. S. Li, C. Lidman, M. Lima, H. Lin, E. Macaulay, M. March, J. L. Marshall, P. Martini, P. Melchior, F. Menanteau, R. Miquel, J. J. Mohr, A. Möller, R. C. Nichol, B. Nord, C. R. O'Neill, W. J. Percival, D. Petravick, A. A. Plazas, A. K. Romer, M. Sako, E. Sanchez, V. Scarpine, R. Schindler, M. Schubnell, E. Sheldon, M. Smith, R. C. Smith, M. Soares-Santos, F. Sobreira, N. E. Sommer, E. Suchyta, M. E. C. Swanson, G. Tarle, D. Thomas, B. E. Tucker, D. L. Tucker, S. A. Uddin, V. Vikram, A. R. Walker, R. H. Wechsler, J. Weller, W. Wester, R. C. Wolf, F. Yuan, B. Zhang, J. Zuntz, and DES Collaboration. Dark Energy Survey year 1 results: Galaxy clustering for combined probes. , 98(4):042006, August 2018. doi: 10.1103/PhysRevD.98.042006.

[22] S. Pandey, E. Krause, J. DeRose, N. MacCrann, B. Jain, M. Crocce, J. Blazek, A. Choi, H. Huang, C. To, X. Fang, J. Elvin-Poole, J. Prat, A. Porredon, L. F. Secco, M. Rodriguez-Monroy, N. Weaverdyck, Y. Park, M. Raveri, E. Rozo, E. S. Rykoff, G. M. Bernstein, C. Sánchez, M. Jarvis, M. A. Troxel, G. Zacharegkas, C. Chang, A. Alarcon, O. Alves, A. Amon, F. Andrade-Oliveira, E. Baxter, K. Bechtol, M. R. Becker, H. Camacho, A. Campos, A. Carnero Rosell, M. Carrasco Kind, R. Cawthon, R. Chen, P. Chintalapati, C. Davis, E. Di Valentino, H. T. Diehl, S. Dodelson, C. Doux, A. Drlica-Wagner, K. Eckert, T. F. Eifler, F. Elsner, S. Everett, A. Farahi, A. Ferté, P. Fosalba, O. Friedrich,

M. Gatti, G. Giannini, D. Gruen, R. A. Gruendl, I. Harrison, W. G. Hartley, E. M. Huff, D. Huterer, A. Kovacs, P. F. Leget, J. McCullough, J. Muir, J. Myles, A. Navarro-Alsina, Y. Omori, R. P. Rollins, A. Roodman, R. Rosenfeld, I. Sevilla-Noarbe, E. Sheldon, T. Shin, A. Troja, I. Tutusaus, T. N. Varga, R. H. Wechsler, B. Yanny, B. Yin, Y. Zhang, J. Zuntz, T. M. C. Abbott, M. Aguena, S. Allam, J. Annis, D. Bacon, E. Bertin, D. Brooks, D. L. Burke, J. Carretero, C. Conselice, M. Costanzi, L. N. da Costa, M. E. S. Pereira, J. De Vicente, J. P. Dietrich, P. Doel, A. E. Evrard, I. Ferrero, B. Flaugher, J. Frieman, J. García-Bellido, E. Gaztanaga, D. W. Gerdes, T. Giannantonio, J. Gschwend, G. Gutierrez, S. R. Hinton, D. L. Hollowood, K. Honscheid, D. J. James, T. Jeltema, K. Kuehn, N. Kuropatkin, O. Lahav, M. Lima, H. Lin, M. A. G. Maia, J. L. Marshall, P. Melchior, F. Menanteau, C. J. Miller, R. Miquel, J. J. Mohr, R. Morgan, A. Palmese, F. Paz-Chinchón, D. Petravick, A. Pieres, A. A. Plazas Malagón, E. Sanchez, V. Scarpine, S. Serrano, M. Smith, M. Soares-Santos, E. Suchyta, G. Tarle, D. Thomas, J. Weller, and DES Collaboration. Dark Energy Survey year 3 results: Constraints on cosmological parameters and galaxy-bias models from galaxy clustering and galaxy-galaxy lensing using the redMaGiC sample. , 106(4):043520, August 2022. doi: 10.1103/PhysRevD.106.043520.

[23] A. Porredon, M. Crocce, J. Elvin-Poole, R. Cawthon, G. Giannini, J. De Vicente, A. Carnero Rosell, I. Ferrero, E. Krause, X. Fang, J. Prat, M. Rodriguez-Monroy, S. Pandey, A. Pocino, F. J. Castander, A. Choi, A. Amon, I. Tutusaus, S. Dodelson, I. Sevilla-Noarbe, P. Fosalba, E. Gaztanaga, A. Alarcon, O. Alves, F. Andrade-Oliveira, E. Baxter, K. Bechtol, M. R. Becker, G. M. Bernstein, J. Blazek, H. Camacho, A. Campos, M. Carrasco Kind, P. Chintalapati, J. Cordero, J. DeRose, E. Di Valentino, C. Doux, T. F. Eifler, S. Everett, A. Ferté, O. Friedrich, M. Gatti, D. Gruen, I. Harrison, W. G. Hartley, K. Herner, E. M. Huff, D. Huterer, B. Jain, M. Jarvis, S. Lee, P. Lemos, N. MacCrann, J. Mena-Fernández, J. Muir, J. Myles, Y. Park, M. Raveri, R. Rosenfeld, A. J. Ross, E. S. Rykoff, S. Samuroff, C. Sánchez, E. Sanchez, J. Sanchez, D. Sanchez Cid, D. Scolnic, L. F. Secco, E. Sheldon, A. Troja, M. A. Troxel, N. Weaverdyck, B. Yanny, J. Zuntz, T. M. C. Abbott, M. Aguena, S. Allam, J. Annis, S. Avila, D. Bacon, E. Bertin, S. Bhargava, D. Brooks, E. Buckley-Geer, D. L. Burke, J. Carretero, M. Costanzi, L. N. da Costa, M. E. S. Pereira, T. M. Davis, S. Desai, H. T. Diehl, J. P. Dietrich, P. Doel, A. Drlica-Wagner, K. Eckert, A. E. Evrard, B. Flaugher, J. Frieman, J. García-Bellido, D. W. Gerdes, T. Giannantonio, R. A. Gruendl, J. Gschwend, G. Gutierrez,

S. R. Hinton, D. L. Hollowood, K. Honscheid, B. Hoyle, D. J. James, K. Kuehn, N. Kuropatkin, O. Lahav, C. Lidman, M. Lima, H. Lin, M. A. G. Maia, J. L. Marshall, P. Martini, P. Melchior, F. Menanteau, R. Miquel, J. J. Mohr, R. Morgan, R. L. C. Ogando, A. Palmese, F. Paz-Chinchón, D. Petravick, A. Pieres, A. A. Plazas Malagón, A. K. Romer, B. Santiago, V. Scarpine, M. Schubnell, S. Serrano, M. Smith, M. Soares-Santos, E. Suchyta, G. Tarle, D. Thomas, C. To, T. N. Varga, and J. Weller. Dark Energy Survey Year 3 results: Cosmological constraints from galaxy clustering and galaxy-galaxy lensing using the MagLim lens sample. *arXiv e-prints*, art. arXiv:2105.13546, May 2021.

[24] A. Amon, D. Gruen, M. A. Troxel, N. MacCrann, S. Dodelson, A. Choi, C. Doux, L. F. Secco, S. Samuroff, E. Krause, J. Cordero, J. Myles, J. DeRose, R. H. Wechsler, M. Gatti, A. Navarro-Alsina, G. M. Bernstein, B. Jain, J. Blazek, A. Alarcon, A. Ferté, P. Lemos, M. Raveri, A. Campos, J. Prat, C. Sánchez, M. Jarvis, O. Alves, F. Andrade-Oliveira, E. Baxter, K. Bechtol, M. R. Becker, S. L. Bridle, H. Camacho, A. Carnero Rosell, M. Carrasco Kind, R. Cawthon, C. Chang, R. Chen, P. Chintalapati, M. Crocce, C. Davis, H. T. Diehl, A. Drlica-Wagner, K. Eckert, T. F. Eifler, J. Elvin-Poole, S. Everett, X. Fang, P. Fosalba, O. Friedrich, E. Gaztanaga, G. Giannini, R. A. Gruendl, I. Harrison, W. G. Hartley, K. Herner, H. Huang, E. M. Huff, D. Huterer, N. Kuropatkin, P. Leget, A. R. Liddle, J. McCullough, J. Muir, S. Pandey, Y. Park, A. Porredon, A. Refregier, R. P. Rollins, A. Roodman, R. Rosenfeld, A. J. Ross, E. S. Rykoff, J. Sanchez, I. Sevilla-Noarbe, E. Sheldon, T. Shin, A. Troja, I. Tutusaus, I. Tutusaus, T. N. Varga, N. Weaverdyck, B. Yanny, B. Yin, Y. Zhang, J. Zuntz, M. Aguena, S. Allam, J. Annis, D. Bacon, E. Bertin, S. Bhargava, D. Brooks, E. Buckley-Geer, D. L. Burke, J. Carretero, M. Costanzi, L. N. da Costa, M. E. S. Pereira, J. De Vicente, S. Desai, J. P. Dietrich, P. Doel, I. Ferrero, B. Flaugher, J. Frieman, J. García-Bellido, E. Gaztanaga, D. W. Gerdes, T. Giannantonio, J. Gschwend, G. Gutierrez, S. R. Hinton, D. L. Hollowood, K. Honscheid, B. Hoyle, D. J. James, R. Kron, K. Kuehn, O. Lahav, M. Lima, H. Lin, M. A. G. Maia, J. L. Marshall, P. Martini, P. Melchior, F. Menanteau, R. Miquel, J. J. Mohr, R. Morgan, R. L. C. Ogando, A. Palmese, F. Paz-Chinchón, D. Petravick, A. Pieres, A. K. Romer, E. Sanchez, V. Scarpine, M. Schubnell, S. Serrano, M. Smith, M. Soares-Santos, G. Tarle, D. Thomas, C. To, J. Weller, and DES Collaboration. Dark Energy Survey Year 3 results: Cosmology from cosmic shear and robustness to data calibration. , 105 (2):023514, January 2022. doi: 10.1103/PhysRevD.105.023514.

[25] Scott Dodelson. *Modern Cosmology*. Academic Press, Elsevier Science, 2003.

[26] E. Krause, T. F. Eifler, J. Zuntz, O. Friedrich, M. A. Troxel, S. Dodelson, J. Blazek, L. F. Secco, N. MacCrann, E. Baxter, C. Chang, N. Chen, M. Crocce, J. DeRose, A. Ferte, N. Kokron, F. Lacasa, V. Miranda, Y. Omori, A. Porredon, R. Rosenfeld, S. Samuroff, M. Wang, R. H. Wechsler, T. M. C. Abbott, F. B. Abdalla, S. Allam, J. Annis, K. Bechtol, A. Benoit-Levy, G. M. Bernstein, D. Brooks, D. L. Burke, D. Capozzi, M. Carrasco Kind, J. Carretero, C. B. D'Andrea, L. N. da Costa, C. Davis, D. L. DePoy, S. Desai, H. T. Diehl, J. P. Dietrich, A. E. Evrard, B. Flaugher, P. Fosalba, J. Frieman, J. Garcia-Bellido, E. Gaztanaga, T. Giannantonio, D. Gruen, R. A. Gruendl, J. Gschwend, G. Gutierrez, K. Honscheid, D. J. James, T. Jeltema, K. Kuehn, S. Kuhlmann, O. Lahav, M. Lima, M. A. G. Maia, M. March, J. L. Marshall, P. Martini, F. Menanteau, R. Miquel, R. C. Nichol, A. A. Plazas, A. K. Romer, E. S. Rykoff, E. Sanchez, V. Scarpine, R. Schindler, M. Schubnell, I. Sevilla-Noarbe, M. Smith, M. Soares-Santos, F. Sobreira, E. Suchyta, M. E. C. Swanson, G. Tarle, D. L. Tucker, V. Vikram, A. R. Walker, and J. Weller. Dark Energy Survey Year 1 Results: Multi-Probe Methodology and Simulated Likelihood Analyses. *arXiv e-prints*, art. arXiv:1706.09359, June 2017.

[27] D. Nelson Limber. The Analysis of Counts of the Extragalactic Nebulae in Terms of a Fluctuating Density Field. , 117:134, January 1953. doi: 10.1086/145672.

[28] Marilena LoVerde and Niayesh Afshordi. Extended Limber Approximation. *Phys. Rev. D*, 78:123506, 2008. doi: 10.1103/PhysRevD.78.123506.

[29] Wayne Hu and Bhuvnesh Jain. Joint galaxy - lensing observables and the dark energy. *Phys. Rev. D*, 70:043009, 2004. doi: 10.1103/PhysRevD.70.043009.

[30] Marc Kamionkowski, Arif Babul, Catherine M. Cress, and Alexandre Refregier. Theory and statistics of weak lensing from large-scale mass inhomogeneities. *Monthly Notices of the Royal Astronomical Society*, 301 (4):1064–1072, 12 1998. ISSN 0035-8711. doi: 10.1046/j.1365-8711.1998.02054.x. URL `https://doi.org/10.1046/j.1365-8711.1998.02054.x`.

[31] Albert Stebbins. Weak Lensing On the Celestial Sphere. *arXiv e-prints*, art. astro-ph/9609149, September 1996.

[32] Wayne Hu. Power Spectrum Tomography with Weak Lensing. , 522(1): L21–L24, September 1999. doi: 10.1086/312210.

[33] E. Krause, X. Fang, S. Pandey, L. F. Secco, O. Alves, H. Huang, J. Blazek, J. Prat, J. Zuntz, T. F. Eifler, N. MacCrann, J. DeRose, M. Crocce, A. Porredon, B. Jain, M. A. Troxel, S. Dodelson, D. Huterer, A. R. Liddle, C. D. Leonard, A. Amon, A. Chen, J. Elvin-Poole, A. Ferté, J. Muir, Y. Park, S. Samuroff, A. Brandao-Souza, N. Weaverdyck, G. Zacharegkas, R. Rosenfeld, A. Campos, P. Chintalapati, A. Choi, E. Di Valentino, C. Doux, K. Herner, P. Lemos, J. Mena-Fernández, Y. Omori, M. Paterno, M. Rodriguez-Monroy, P. Rogozenski, R. P. Rollins, A. Troja, I. Tutusaus, R. H. Wechsler, T. M. C. Abbott, M. Aguena, S. Allam, F. Andrade-Oliveira, J. Annis, D. Bacon, E. Baxter, K. Bechtol, G. M. Bernstein, D. Brooks, E. Buckley-Geer, D. L. Burke, A. Carnero Rosell, M. Carrasco Kind, J. Carretero, F. J. Castander, R. Cawthon, C. Chang, M. Costanzi, L. N. da Costa, M. E. S. Pereira, J. De Vicente, S. Desai, H. T. Diehl, P. Doel, S. Everett, A. E. Evrard, I. Ferrero, B. Flaugher, P. Fosalba, J. Frieman, J. García-Bellido, E. Gaztanaga, D. W. Gerdes, T. Giannantonio, D. Gruen, R. A. Gruendl, J. Gschwend, G. Gutierrez, W. G. Hartley, S. R. Hinton, D. L. Hollowood, K. Honscheid, B. Hoyle, E. M. Huff, D. J. James, K. Kuehn, N. Kuropatkin, O. Lahav, M. Lima, M. A. G. Maia, J. L. Marshall, P. Martini, P. Melchior, F. Menanteau, R. Miquel, J. J. Mohr, R. Morgan, J. Myles, A. Palmese, F. Paz-Chinchón, D. Petravick, A. Pieres, A. A. Plazas Malagón, E. Sanchez, V. Scarpine, M. Schubnell, S. Serrano, I. Sevilla-Noarbe, M. Smith, M. Soares-Santos, E. Suchyta, G. Tarle, D. Thomas, C. To, T. N. Varga, and J. Weller. Dark Energy Survey Year 3 Results: Multi-Probe Modeling Strategy and Validation. *arXiv e-prints*, art. arXiv:2105.13548, May 2021.

[34] Micael Jarvis, G. Bernstein, and B. Jain. The skewness of the aperture mass statistic. *Mon. Not. Roy. Astron. Soc.*, 352:338–352, 2004. doi: 10.1111/j.1365-2966.2004.07926.x.

[35] P. J. E. Peebles. *The large-scale structure of the universe*. 1980.

[36] M. Davis and P. J. E. Peebles. A survey of galaxy redshifts. V. The two-point position and velocity correlations. , 267:465–482, April 1983. doi: 10.1086/160884.

[37] Stephen D. Landy and Alexander S. Szalay. Bias and Variance of Angular Correlation Functions. , 412:64, July 1993. doi: 10.1086/172900.

[38] Lucy Liuxuan Zhang and Ue-Li Pen. Fast n-point correlation functions and three-point lensing application. , 10(7):569–590, July 2005. doi: 10.1016/j.newast.2005.04.002.

[39] Elisabeth Krause and Tim Eifler. cosmolike – cosmological likelihood analyses for photometric galaxy surveys. *Mon. Not. Roy. Astron. Soc.*, 470(2):2100–2112, 2017. doi: 10.1093/mnras/stx1261.

[40] S. Pandey, E. Krause, J. DeRose, N. MacCrann, B. Jain, M. Crocce, J. Blazek, A. Choi, H. Huang, C. To, X. Fang, J. Elvin-Poole, J. Prat, A. Porredon, L. F. Secco, M. Rodriguez-Monroy, N. Weaverdyck, Y. Park, M. Raveri, E. Rozo, E. S. Rykoff, G. M. Bernstein, C. Sánchez, M. Jarvis, M. A. Troxel, G. Zacharegkas, C. Chang, A. Alarcon, O. Alves, A. Amon, F. Andrade-Oliveira, E. Baxter, K. Bechtol, M. R. Becker, H. Camacho, A. Campos, A. Carnero Rosell, M. Carrasco Kind, R. Cawthon, R. Chen, P. Chintalapati, C. Davis, E. Di Valentino, H. T. Diehl, S. Dodelson, C. Doux, A. Drlica-Wagner, K. Eckert, T. F. Eifler, F. Elsner, S. Everett, A. Farahi, A. Ferté, P. Fosalba, O. Friedrich, M. Gatti, G. Giannini, D. Gruen, R. A. Gruendl, I. Harrison, W. G. Hartley, E. M. Huff, D. Huterer, A. Kovacs, P. F. Leget, J. McCullough, J. Muir, J. Myles, A. Navarro-Alsina, Y. Omori, R. P. Rollins, A. Roodman, R. Rosenfeld, I. Sevilla-Noarbe, E. Sheldon, T. Shin, A. Troja, I. Tutusaus, T. N. Varga, R. H. Wechsler, B. Yanny, B. Yin, Y. Zhang, J. Zuntz, T. M. C. Abbott, M. Aguena, S. Allam, J. Annis, D. Bacon, E. Bertin, D. Brooks, D. L. Burke, J. Carretero, C. Conselice, M. Costanzi, L. N. da Costa, M. E. S. Pereira, J. De Vicente, J. P. Dietrich, P. Doel, A. E. Evrard, I. Ferrero, B. Flaugher, J. Frieman, J. García-Bellido, E. Gaztanaga, D. W. Gerdes, T. Giannantonio, J. Gschwend, G. Gutierrez, S. R. Hinton, D. L. Hollowood, K. Honscheid, D. J. James, T. Jeltema, K. Kuehn, N. Kuropatkin, O. Lahav, M. Lima, H. Lin, M. A. G. Maia, J. L. Marshall, P. Melchior, F. Menanteau, C. J. Miller, R. Miquel, J. J. Mohr, R. Morgan, A. Palmese, F. Paz-Chinchón, D. Petravick, A. Pieres, A. A. Plazas Malagón, E. Sanchez, V. Scarpine, S. Serrano, M. Smith, M. Soares-Santos, E. Suchyta, G. Tarle, D. Thomas, J. Weller, and DES Collaboration. Dark Energy Survey year 3 results: Constraints on cosmological parameters and galaxy-bias models from galaxy clustering and galaxy-galaxy lensing using the redMaGiC sample. , 106(4):043520, August 2022. doi: 10.1103/PhysRevD.106.043520.

[41] Andreas A. Berlind and David H. Weinberg. The Halo Occupation Distribution: Toward an Empirical Determination of the Relation between Galaxies and Mass. , 575(2):587–616, August 2002. doi: 10.1086/341469.

[42] James S. Bullock, Risa H. Wechsler, and Rachel S. Somerville. Galaxy halo occupation at high redshift. , 329(1):246–256, January 2002. doi: 10.1046/j.1365-8711.2002.04959.x.

[43] Zheng Zheng, Alison L. Coil, and Idit Zehavi. Galaxy Evolution from Halo Occupation Distribution Modeling of DEEP2 and SDSS Galaxy Clustering. , 667(2):760–779, October 2007. doi: 10.1086/521074.

[44] Alexie Leauthaud, Kevin Bundy, Shun Saito, Jeremy Tinker, Claudia Maraston, Rita Tojeiro, Song Huang, Joel R. Brownstein, Donald P. Schneider, and Daniel Thomas. The Stripe 82 Massive Galaxy Project - II. Stellar mass completeness of spectroscopic galaxy samples from the Baryon Oscillation Spectroscopic Survey. , 457(4):4021–4037, April 2016. doi: 10.1093/mnras/stw117.

[45] Jonathan Blazek, Niall MacCrann, M. A. Troxel, and Xiao Fang. Beyond linear galaxy alignments. *Phys. Rev. D*, 100(10):103506, 2019. doi: 10.1103/PhysRevD.100.103506.

[46] Christopher M. Hirata and Uros Seljak. Shear calibration biases in weak lensing surveys. *Mon. Not. Roy. Astron. Soc.*, 343:459–480, 2003. doi: 10.1046/j.1365-8711.2003.06683.x.

[47] N. MacCrann, M. R. Becker, J. McCullough, A. Amon, D. Gruen, M. Jarvis, A. Choi, M. A. Troxel, E. Sheldon, B. Yanny, K. Herner, S. Dodelson, J. Zuntz, K. Eckert, R. P. Rollins, T. N. Varga, G. M. Bernstein, R. A. Gruendl, I. Harrison, W. G. Hartley, I. Sevilla-Noarbe, A. Pieres, S. L. Bridle, J. Myles, A. Alarcon, S. Everett, C. Sánchez, E. M. Huff, F. Tarsitano, M. Gatti, L. F. Secco, T. M. C. Abbott, M. Aguena, S. Allam, J. Annis, D. Bacon, E. Bertin, D. Brooks, D. L. Burke, A. Carnero Rosell, M. Carrasco Kind, J. Carretero, M. Costanzi, M. Crocce, M. E. S. Pereira, J. De Vicente, S. Desai, H. T. Diehl, J. P. Dietrich, P. Doel, T. F. Eifler, I. Ferrero, A. Ferté, B. Flaugher, P. Fosalba, J. Frieman, J. García-Bellido, E. Gaztanaga, D. W. Gerdes, T. Giannantonio, J. Gschwend, G. Gutierrez, S. R. Hinton, D. L. Hollowood, K. Honscheid, D. J. James, O. Lahav, M. Lima, M. A. G. Maia, M. March, J. L. Marshall, P. Martini, P. Melchior, F. Menanteau, R. Miquel, J. J. Mohr, R. Morgan, J. Muir, R. L. C. Ogando, A. Palmese, F. Paz-Chinchón, A. A. Plazas, M. Rodriguez-Monroy, A. Roodman, S. Samuroff, E. Sanchez, V. Scarpine, S. Serrano, M. Smith, M. Soares-Santos, E. Suchyta, M. E. C. Swanson, G. Tarle, D. Thomas, C. To, R. D.

Wilkinson, R. D. Wilkinson, and DES Collaboration. Dark Energy Survey Y3 results: blending shear and redshift biases in image simulations. , 509(3):3371–3394, January 2022. doi: 10.1093/mnras/stab2870.

[48] T. M. C. Abbott, M. Aguena, A. Alarcon, O. Alves, A. Amon, F. Andrade-Oliveira, J. Annis, B. Ansarinejad, S. Avila, D. Bacon, E. J. Baxter, K. Bechtol, M. R. Becker, B. A. Benson, G. M. Bernstein, E. Bertin, J. Blazek, L. E. Bleem, S. Bocquet, D. Brooks, E. Buckley-Geer, D. L. Burke, H. Camacho, A. Campos, J. E. Carlstrom, A. Carnero Rosell, M. Carrasco Kind, J. Carretero, R. Cawthon, C. Chang, C. L. Chang, R. Chen, A. Choi, R. Chown, C. Conselice, J. Cordero, M. Costanzi, T. Crawford, A. T. Crites, M. Crocce, L. N. da Costa, C. Davis, T. M. Davis, T. de Haan, J. De Vicente, J. DeRose, S. Desai, H. T. Diehl, M. A. Dobbs, S. Dodelson, P. Doel, C. Doux, A. Drlica-Wagner, K. Eckert, T. F. Eifler, F. Elsner, J. Elvin-Poole, S. Everett, W. Everett, X. Fang, I. Ferrero, A. Ferté, B. Flaugher, P. Fosalba, O. Friedrich, J. Frieman, J. García-Bellido, M. Gatti, E. M. George, T. Giannantonio, G. Giannini, D. Gruen, R. A. Gruendl, J. Gschwend, G. Gutierrez, N. W. Halverson, I. Harrison, K. Herner, S. R. Hinton, G. P. Holder, D. L. Hollowood, W. L. Holzapfel, K. Honscheid, J. D. Hrubes, H. Huang, E. M. Huff, D. Huterer, B. Jain, D. J. James, M. Jarvis, T. Jeltema, S. Kent, L. Knox, A. Kovacs, E. Krause, K. Kuehn, N. Kuropatkin, O. Lahav, A. T. Lee, P. F. Leget, P. Lemos, A. R. Liddle, C. Lidman, D. Luong-Van, J. J. McMahon, N. MacCrann, M. March, J. L. Marshall, P. Martini, J. McCullough, P. Melchior, F. Menanteau, S. S. Meyer, R. Miquel, L. Mocanu, J. J. Mohr, R. Morgan, J. Muir, J. Myles, T. Natoli, A. Navarro-Alsina, R. C. Nichol, Y. Omori, S. Padin, S. Pandey, Y. Park, F. Paz-Chinchón, M. E. S. Pereira, A. Pieres, A. A. Plazas Malagón, A. Porredon, J. Prat, C. Pryke, M. Raveri, C. L. Reichardt, R. P. Rollins, A. K. Romer, A. Roodman, R. Rosenfeld, A. J. Ross, J. E. Ruhl, E. S. Rykoff, C. Sánchez, E. Sanchez, J. Sanchez, K. K. Schaffer, L. F. Secco, I. Sevilla-Noarbe, E. Sheldon, T. Shin, E. Shirokoff, M. Smith, Z. Staniszewski, A. A. Stark, E. Suchyta, M. E. C. Swanson, G. Tarle, C. To, M. A. Troxel, I. Tutusaus, T. N. Varga, J. D. Vieira, N. Weaverdyck, R. H. Wechsler, J. Weller, R. Williamson, W. L. K. Wu, B. Yanny, B. Yin, Y. Zhang, and J. Zuntz. Joint analysis of DES Year 3 data and CMB lensing from SPT and Planck III: Combined cosmological constraints. *arXiv e-prints*, art. arXiv:2206.10824, June 2022.

[49] Kunhao Zhong, Evan Saraivanov, Vivian Miranda, Jiachuan Xu, Tim

Eifler, and Elisabeth Krause. Growth and Geometry Split in Light of the DES-Y3 Survey. *arXiv e-prints*, art. arXiv:2301.03694, January 2023.

[50] Juan P. Cordero, Ian Harrison, Richard P. Rollins, G. M. Bernstein, S. L. Bridle, A. Alarcon, O. Alves, A. Amon, F. Andrade-Oliveira, H. Camacho, A. Campos, A. Choi, J. DeRose, S. Dodelson, K. Eckert, T. F. Eifler, S. Everett, X. Fang, O. Friedrich, D. Gruen, R. A. Gruendl, W. G. Hartley, E. M. Huff, E. Krause, N. Kuropatkin, N. MacCrann, J. McCullough, J. Myles, S. Pandey, M. Raveri, R. Rosenfeld, E. S. Rykoff, C. Sánchez, J. Sánchez, I. Sevilla-Noarbe, E. Sheldon, M. Troxel, R. Wechsler, B. Yanny, B. Yin, Y. Zhang, M. Aguena, S. Allam, E. Bertin, D. Brooks, D. L. Burke, A. Carnero Rosell, M. Carrasco Kind, J. Carretero, F. J. Castander, R. Cawthon, M. Costanzi, L. da Costa, M. E. da Silva Pereira, J. De Vicente, H. T. Diehl, J. Dietrich, P. Doel, J. Elvin-Poole, I. Ferrero, B. Flaugher, P. Fosalba, J. Frieman, J. Garcia-Bellido, D. Gerdes, J. Gschwend, G. Gutierrez, S. Hinton, D. L. Hollowood, K. Honscheid, B. Hoyle, D. James, K. Kuehn, O. Lahav, M. A. G. Maia, M. March, F. Menanteau, R. Miquel, R. Morgan, J. Muir, A. Palmese, F. Paz-Chinchon, A. Pieres, A. Plazas Malagón, E. Sánchez, V. Scarpine, S. Serrano, M. Smith, M. Soares-Santos, E. Suchyta, M. Swanson, G. Tarle, D. Thomas, C. To, T. N. Varga, and DES Collaboration. Dark Energy Survey Year 3 results: marginalization over redshift distribution uncertainties using ranking of discrete realizations. , 511(2):2170–2185, April 2022. doi: 10.1093/mnras/stac147.

[51] Tianqing Zhang, Markus Michael Rau, Rachel Mandelbaum, Xiangchong Li, and Ben Moews. Photometric redshift uncertainties in weak gravitational lensing shear analysis: models and marginalization. , 518 (1):709–723, January 2023. doi: 10.1093/mnras/stac3090.

[52] J. Elvin-Poole, N. MacCrann, S. Everett, J. Prat, E. S. Rykoff, J. De Vicente, B. Yanny, K. Herner, A. Ferté, E. Di Valentino, A. Choi, D. L. Burke, I. Sevilla-Noarbe, A. Alarcon, O. Alves, A. Amon, F. Andrade-Oliveira, E. Baxter, K. Bechtol, M. R. Becker, G. M. Bernstein, J. Blazek, H. Camacho, A. Campos, A. Carnero Rosell, M. Carrasco Kind, R. Cawthon, C. Chang, R. Chen, J. Cordero, M. Crocce, C. Davis, J. DeRose, H. T. Diehl, S. Dodelson, C. Doux, A. Drlica-Wagner, K. Eckert, T. F. Eifler, F. Elsner, X. Fang, P. Fosalba, O. Friedrich, M. Gatti, G. Giannini, D. Gruen, R. A. Gruendl, I. Harrison, W. G. Hartley, H. Huang, E. M. Huff, D. Huterer, E. Krause, N. Kuropatkin, P. F. Leget, P. Lemos, A. R. Liddle, J. McCullough, J. Muir, J. Myles, A. Navarro-Alsina, S. Pandey, Y. Park, A. Porredon,

M. Raveri, M. Rodriguez-Monroy, R. P. Rollins, A. Roodman, R. Rosenfeld, A. J. Ross, C. Sánchez, J. Sanchez, L. F. Secco, E. Sheldon, T. Shin, M. A. Troxel, I. Tutusaus, T. N. Varga, N. Weaverdyck, R. H. Wechsler, B. Yin, Y. Zhang, J. Zuntz, M. Aguena, S. Avila, D. Bacon, E. Bertin, S. Bocquet, D. Brooks, J. García-Bellido, K. Honscheid, M. Jarvis, T. S. Li, J. Mena-Fernández, C. To, and R. D. Wilkinson. Dark Energy Survey Year 3 results: Magnification modeling and impact on cosmological constraints from galaxy clustering and galaxy-galaxy lensing. *arXiv e-prints*, art. arXiv:2209.09782, September 2022.

[53] Niall MacCrann, Jonathan Blazek, Bhuvnesh Jain, and Elisabeth Krause. Controlling and leveraging small-scale information in tomographic galaxy–galaxy lensing. *Mon. Not. Roy. Astron. Soc.*, 491(4): 5498–5509, 2020. doi: 10.1093/mnras/stz2761.

[54] Julien Lesgourgues. Tasi lectures on cosmological perturbations, 2013.

[55] Chung-Pei Ma and Edmund Bertschinger. Cosmological perturbation theory in the synchronous and conformal newtonian gauges. *The Astrophysical Journal*, 455:7, Dec 1995. ISSN 1538-4357. doi: 10.1086/176550. URL `http://dx.doi.org/10.1086/176550`.

[56] Planck Collaboration, N. Aghanim, Y. Akrami, M. Ashdown, J. Aumont, C. Baccigalupi, M. Ballardini, A. J. Banday, R. B. Barreiro, N. Bartolo, S. Basak, K. Benabed, J. P. Bernard, M. Bersanelli, P. Bielewicz, J. J. Bock, J. R. Bond, J. Borrill, F. R. Bouchet, F. Boulanger, M. Bucher, C. Burigana, E. Calabrese, J. F. Cardoso, J. Carron, A. Challinor, H. C. Chiang, L. P. L. Colombo, C. Combet, B. P. Crill, F. Cuttaia, P. de Bernardis, G. de Zotti, J. Delabrouille, E. Di Valentino, J. M. Diego, O. Doré, M. Douspis, A. Ducout, X. Dupac, G. Efstathiou, F. Elsner, T. A. Enßlin, H. K. Eriksen, Y. Fantaye, R. Fernandez-Cobos, F. Finelli, F. Forastieri, M. Frailis, A. A. Fraisse, E. Franceschi, A. Frolov, S. Galeotta, S. Galli, K. Ganga, R. T. Génova-Santos, M. Gerbino, T. Ghosh, J. González-Nuevo, K. M. Górski, S. Gratton, A. Gruppuso, J. E. Gudmundsson, J. Hamann, W. Handley, F. K. Hansen, D. Herranz, E. Hivon, Z. Huang, A. H. Jaffe, W. C. Jones, A. Karakci, E. Keihänen, R. Keskitalo, K. Kiiveri, J. Kim, L. Knox, N. Krachmalnicoff, M. Kunz, H. Kurki-Suonio, G. Lagache, J. M. Lamarre, A. Lasenby, M. Lattanzi, C. R. Lawrence, M. Le Jeune, F. Levrier, A. Lewis, M. Liguori, P. B. Lilje, V. Lindholm, M. López-Caniego, P. M. Lubin, Y. Z. Ma, J. F. Macías-Pérez, G. Maggio, D. Maino, N. Mandolesi, A. Mangilli, A. Marcos-Caballero, M. Maris, P. G. Martin, E. Martínez-González, S. Matar-

rese, N. Mauri, J. D. McEwen, A. Melchiorri, A. Mennella, M. Migliaccio, M. A. Miville-Deschênes, D. Molinari, A. Moneti, L. Montier, G. Morgante, A. Moss, P. Natoli, L. Pagano, D. Paoletti, B. Partridge, G. Patanchon, F. Perrotta, V. Pettorino, F. Piacentini, L. Polastri, G. Polenta, J. L. Puget, J. P. Rachen, M. Reinecke, M. Remazeilles, A. Renzi, G. Rocha, C. Rosset, G. Roudier, J. A. Rubiño-Martín, B. Ruiz-Granados, L. Salvati, M. Sandri, M. Savelainen, D. Scott, C. Sirignano, R. Sunyaev, A. S. Suur-Uski, J. A. Tauber, D. Tavagnacco, M. Tenti, L. Toffolatti, M. Tomasi, T. Trombetti, J. Valiviita, B. Van Tent, P. Vielva, F. Villa, N. Vittorio, B. D. Wandelt, I. K. Wehus, M. White, S. D. M. White, A. Zacchei, and A. Zonca. Planck 2018 results. VIII. Gravitational lensing. , 641:A8, September 2020. doi: 10.1051/0004-6361/201833886.

[57] Planck Collaboration, P. A. R. Ade, N. Aghanim, M. Arnaud, M. Ashdown, J. Aumont, C. Baccigalupi, A. J. Banday, R. B. Barreiro, J. G. Bartlett, N. Bartolo, E. Battaner, K. Benabed, A. Benoît, A. Benoit-Lévy, J. P. Bernard, M. Bersanelli, P. Bielewicz, J. J. Bock, A. Bonaldi, L. Bonavera, J. R. Bond, J. Borrill, F. R. Bouchet, F. Boulanger, M. Bucher, C. Burigana, R. C. Butler, E. Calabrese, J. F. Cardoso, G. Castex, A. Catalano, A. Challinor, A. Chamballu, H. C. Chiang, P. R. Christensen, D. L. Clements, S. Colombi, L. P. L. Colombo, C. Combet, F. Couchot, A. Coulais, B. P. Crill, A. Curto, F. Cuttaia, L. Danese, R. D. Davies, R. J. Davis, P. de Bernardis, A. de Rosa, G. de Zotti, J. Delabrouille, J. M. Delouis, F. X. Désert, C. Dickinson, J. M. Diego, K. Dolag, H. Dole, S. Donzelli, O. Doré, M. Douspis, A. Ducout, X. Dupac, G. Efstathiou, F. Elsner, T. A. Enßlin, H. K. Eriksen, J. Fergusson, F. Finelli, O. Forni, M. Frailis, A. A. Fraisse, E. Franceschi, A. Frejsel, S. Galeotta, S. Galli, K. Ganga, T. Ghosh, M. Giard, Y. Giraud-Héraud, E. Gjerløw, J. González-Nuevo, K. M. Górski, S. Gratton, A. Gregorio, A. Gruppuso, J. E. Gudmundsson, F. K. Hansen, D. Hanson, D. L. Harrison, S. Henrot-Versillé, C. Hernández-Monteagudo, D. Herranz, S. R. Hildebrandt, E. Hivon, M. Hobson, W. A. Holmes, A. Hornstrup, W. Hovest, K. M. Huffenberger, G. Hurier, A. H. Jaffe, T. R. Jaffe, W. C. Jones, M. Juvela, A. Karakci, E. Keihänen, R. Keskitalo, K. Kiiveri, T. S. Kisner, R. Kneissl, J. Knoche, M. Kunz, H. Kurki-Suonio, G. Lagache, J. M. Lamarre, A. Lasenby, M. Lattanzi, C. R. Lawrence, R. Leonardi, J. Lesgourgues, F. Levrier, M. Liguori, P. B. Lilje, M. Linden-Vørnle, V. Lindholm, M. López-Caniego, P. M. Lubin, J. F. Macías-Pérez, G. Maggio, D. Maino, N. Mandolesi, A. Mangilli, M. Maris, P. G. Martin, E. Martínez-González, S. Masi, S. Matarrese,

P. McGehee, P. R. Meinhold, A. Melchiorri, J. B. Melin, L. Mendes, A. Mennella, M. Migliaccio, S. Mitra, M. A. Miville-Deschênes, A. Moneti, L. Montier, G. Morgante, D. Mortlock, A. Moss, D. Munshi, J. A. Murphy, P. Naselsky, F. Nati, P. Natoli, C. B. Netterfield, H. U. Nørgaard-Nielsen, F. Noviello, D. Novikov, I. Novikov, C. A. Oxborrow, F. Paci, L. Pagano, F. Pajot, D. Paoletti, F. Pasian, G. Patanchon, T. J. Pearson, O. Perdereau, L. Perotto, F. Perrotta, V. Pettorino, F. Piacentini, M. Piat, E. Pierpaoli, D. Pietrobon, S. Plaszczynski, E. Pointecouteau, G. Polenta, G. W. Pratt, G. Prézeau, S. Prunet, J. L. Puget, J. P. Rachen, R. Rebolo, M. Reinecke, M. Remazeilles, C. Renault, A. Renzi, I. Ristorcelli, G. Rocha, M. Roman, C. Rosset, M. Rossetti, G. Roudier, J. A. Rubiño-Martín, B. Rusholme, M. Sandri, D. Santos, M. Savelainen, D. Scott, M. D. Seiffert, E. P. S. Shellard, L. D. Spencer, V. Stolyarov, R. Stompor, R. Sudiwala, D. Sutton, A. S. Suur-Uski, J. F. Sygnet, J. A. Tauber, L. Terenzi, L. Toffolatti, M. Tomasi, M. Tristram, M. Tucci, J. Tuovinen, L. Valenziano, J. Valiviita, B. Van Tent, P. Vielva, F. Villa, L. A. Wade, B. D. Wandelt, I. K. Wehus, N. Welikala, D. Yvon, A. Zacchei, and A. Zonca. Planck 2015 results. XII. Full focal plane simulations. , 594:A12, September 2016. doi: 10.1051/0004-6361/201527103.

[58] J. Hartlap, P. Simon, and P. Schneider. Why your model parameter confidences might be too optimistic. Unbiased estimation of the inverse covariance matrix. , 464(1):399–404, March 2007. doi: 10.1051/0004-6361:20066170.

[59] Daniel J. Eisenstein, Hee-Jong Seo, and Martin White. On the Robustness of the Acoustic Scale in the Low-Redshift Clustering of Matter. , 664(2):660–674, August 2007. doi: 10.1086/518755.

[60] Bruce Bassett and Renée Hlozek. Baryon acoustic oscillations. In Pilar Ruiz-Lapuente, editor, *Dark Energy: Observational and Theoretical Approaches*, page 246. 2010.

[61] Ashley J. Ross, Lado Samushia, Cullan Howlett, Will J. Percival, Angela Burden, and Marc Manera. The clustering of the SDSS DR7 main Galaxy sample – I. A 4 per cent distance measure at $z = 0.15$. *Mon. Not. Roy. Astron. Soc.*, 449(1):835–847, 2015. doi: 10.1093/mnras/stv154.

[62] Florian Beutler, Chris Blake, Matthew Colless, D Heath Jones, Lister Staveley-Smith, Lachlan Campbell, Quentin Parker, Will Saunders, and Fred Watson. The 6df galaxy survey: baryon acoustic oscillations and

the local hubble constant. *Monthly Notices of the Royal Astronomical Society*, 416(4):3017–3032, 2011.

[63] Shadab Alam, Metin Ata, Stephen Bailey, Florian Beutler, Dmitry Bizyaev, Jonathan A. Blazek, Adam S. Bolton, Joel R. Brownstein, Angela Burden, Chia-Hsun Chuang, Johan Comparat, Antonio J. Cuesta, Kyle S. Dawson, Daniel J. Eisenstein, Stephanie Escoffier, Héctor Gil-Marín, Jan Niklas Grieb, Nick Hand, Shirley Ho, Karen Kinemuchi, David Kirkby, Francisco Kitaura, Elena Malanushenko, Viktor Malanushenko, Claudia Maraston, Cameron K. McBride, Robert C. Nichol, Matthew D. Olmstead, Daniel Oravetz, Nikhil Padmanabhan, Nathalie Palanque-Delabrouille, Kaike Pan, Marcos Pellejero-Ibanez, Will J. Percival, Patrick Petitjean, Francisco Prada, Adrian M. Price-Whelan, Beth A. Reid, Sergio A. Rodríguez-Torres, Natalie A. Roe, Ashley J. Ross, Nicholas P. Ross, Graziano Rossi, Jose Alberto Rubiño-Martín, Shun Saito, Salvador Salazar-Albornoz, Lado Samushia, Ariel G. Sánchez, Siddharth Satpathy, David J. Schlegel, Donald P. Schneider, Claudia G. Scóccola, Hee-Jong Seo, Erin S. Sheldon, Audrey Simmons, Anže Slosar, Michael A. Strauss, Molly E. C. Swanson, Daniel Thomas, Jeremy L. Tinker, Rita Tojeiro, Mariana Vargas Magaña, Jose Alberto Vazquez, Licia Verde, David A. Wake, Yuting Wang, David H. Weinberg, Martin White, W. Michael Wood-Vasey, Christophe Yèche, Idit Zehavi, Zhongxu Zhai, and Gong-Bo Zhao. The clustering of galaxies in the completed SDSS-III Baryon Oscillation Spectroscopic Survey: cosmological analysis of the DR12 galaxy sample. , 470(3):2617–2652, September 2017. doi: 10.1093/mnras/stx721.

[64] D. M. Scolnic, D. O. Jones, A. Rest, Y. C. Pan, R. Chornock, R. J. Foley, M. E. Huber, R. Kessler, G. Narayan, A. G. Riess, S. Rodney, E. Berger, D. J. Brout, P. J. Challis, M. Drout, D. Finkbeiner, R. Lunnan, R. P. Kirshner, N. E. Sanders, E. Schlafly, S. Smartt, C. W. Stubbs, J. Tonry, W. M. Wood-Vasey, M. Foley, J. Hand, E. Johnson, W. S. Burgett, K. C. Chambers, P. W. Draper, K. W. Hodapp, N. Kaiser, R. P. Kudritzki, E. A. Magnier, N. Metcalfe, F. Bresolin, E. Gall, R. Kotak, M. McCrum, and K. W. Smith. The Complete Light-curve Sample of Spectroscopically Confirmed SNe Ia from Pan-STARRS1 and Cosmological Constraints from the Combined Pantheon Sample. , 859(2):101, June 2018. doi: 10.3847/1538-4357/aab9bb.

[65] Dan Scolnic, Dillon Brout, Anthony Carr, Adam G. Riess, Tamara M. Davis, Arianna Dwomoh, David O. Jones, Noor Ali, Pranav Charvu, Rebecca Chen, Erik R. Peterson, Brodie Popovic, Benjamin M. Rose,

Charlotte M. Wood, Peter J. Brown, Ken Chambers, David A. Coulter, Kyle G. Dettman, Georgios Dimitriadis, Alexei V. Filippenko, Ryan J. Foley, Saurabh W. Jha, Charles D. Kilpatrick, Robert P. Kirshner, Yen-Chen Pan, Armin Rest, Cesar Rojas-Bravo, Matthew R. Siebert, Benjamin E. Stahl, and WeiKang Zheng. The Pantheon+ Analysis: The Full Data Set and Light-curve Release. , 938(2):113, October 2022. doi: 10.3847/1538-4357/ac8b7a.

[66] Brian D. Fields. The Primordial Lithium Problem. *Annual Review of Nuclear and Particle Science*, 61(1):47–68, November 2011. doi: 10.1146/annurev-nucl-102010-130445.

[67] Scott Burles, Kenneth M. Nollett, James W. Truran, and Michael S. Turner. Sharpening the Predictions of Big-Bang Nucleosynthesis. , 82 (21):4176–4179, May 1999. doi: 10.1103/PhysRevLett.82.4176.

[68] Ryan J. Cooke, Max Pettini, Kenneth M. Nollett, and Regina Jorgenson. The Primordial Deuterium Abundance of the Most Metal-poor Damped Lyman-α System. , 830(2):148, October 2016. doi: 10.3847/0004-637X/830/2/148.

[69] Michael J. Mortonson, Wayne Hu, and Dragan Huterer. Falsifying Paradigms for Cosmic Acceleration. *Phys. Rev. D*, 79:023004, 2009. doi: 10.1103/PhysRevD.79.023004.

[70] Andreas Albrecht, Gary Bernstein, Robert Cahn, Wendy L. Freedman, Jacqueline Hewitt, Wayne Hu, John Huth, Marc Kamionkowski, Edward W. Kolb, Lloyd Knox, John C. Mather, Suzanne Staggs, and Nicholas B. Suntzeff. Report of the Dark Energy Task Force. *arXiv e-prints*, art. astro-ph/0609591, September 2006.

[71] Mike Chu and Lloyd Knox. Testing cosmological models and understanding cosmological parameter determinations with metaparameters. *Astrophys. J.*, 620:1–6, 2005. doi: 10.1086/427064.

[72] Alexandra Abate and Ofer Lahav. The three faces of m: testing gravity with low- and high-redshift SNe Ia surveys. *Monthly Notices of the Royal Astronomical Society: Letters*, 389(1):L47–L51, 09 2008. ISSN 1745-3925. doi: 10.1111/j.1745-3933.2008.00519.x. URL `https://doi.org/10.1111/j.1745-3933.2008.00519.x`.

[73] Tristan L. Smith, Vivian Poulin, José Luis Bernal, Kimberly K. Boddy, Marc Kamionkowski, and Riccardo Murgia. Early dark energy is not

excluded by current large-scale structure data. *Phys. Rev. D*, 103(12): 123542, 2021. doi: 10.1103/PhysRevD.103.123542.

[74] J. Muir, E. Baxter, V. Miranda, C. Doux, A. Ferté, C. D. Leonard, D. Huterer, B. Jain, P. Lemos, M. Raveri, S. Nadathur, A. Campos, A. Chen, S. Dodelson, J. Elvin-Poole, S. Lee, L. F. Secco, M. A. Troxel, N. Weaverdyck, J. Zuntz, D. Brout, A. Choi, M. Crocce, T. M. Davis, D. Gruen, E. Krause, C. Lidman, N. MacCrann, A. Möller, J. Prat, A. J. Ross, M. Sako, S. Samuroff, C. Sánchez, D. Scolnic, B. Zhang, T. M. C. Abbott, M. Aguena, S. Allam, J. Annis, S. Avila, D. Bacon, E. Bertin, S. Bhargava, S. L. Bridle, D. Brooks, D. L. Burke, A. Carnero Rosell, M. Carrasco Kind, J. Carretero, R. Cawthon, M. Costanzi, L. N. da Costa, M. E. S. Pereira, S. Desai, H. T. Diehl, J. P. Dietrich, P. Doel, J. Estrada, S. Everett, A. E. Evrard, I. Ferrero, B. Flaugher, J. Frieman, J. García-Bellido, T. Giannantonio, R. A. Gruendl, J. Gschwend, G. Gutierrez, S. R. Hinton, D. L. Hollowood, K. Honscheid, B. Hoyle, D. J. James, T. Jeltema, K. Kuehn, N. Kuropatkin, O. Lahav, M. Lima, M. A. G. Maia, F. Menanteau, R. Miquel, R. Morgan, J. Myles, A. Palmese, F. Paz-Chinchón, A. A. Plazas, A. K. Romer, A. Roodman, E. Sanchez, V. Scarpine, S. Serrano, I. Sevilla-Noarbe, M. Smith, E. Suchyta, M. E. C. Swanson, G. Tarle, D. Thomas, C. To, D. L. Tucker, T. N. Varga, J. Weller, R. D. Wilkinson, and DES Collaboration. DES Y1 results: Splitting growth and geometry to test Λ CDM. , 103(2): 023528, January 2021. doi: 10.1103/PhysRevD.103.023528.

[75] Jaime Ruiz-Zapatero, Benjamin Stölzner, Benjamin Joachimi, Marika Asgari, Maciej Bilicki, Andrej Dvornik, Benjamin Giblin, Catherine Heymans, Hendrik Hildebrandt, Arun Kannawadi, Konrad Kuijken, Tilman Tröster, Jan Luca van den Busch, and Angus H. Wright. Geometry versus growth. Internal consistency of the flat ΛCDM model with KiDS-1000. , 655:A11, November 2021. doi: 10.1051/0004-6361/202141350.

[76] Eduardo J. Ruiz and Dragan Huterer. Testing the dark energy consistency with geometry and growth. *Phys. Rev. D*, 91:063009, 2015. doi: 10.1103/PhysRevD.91.063009.

[77] José Luis Bernal, Licia Verde, and Antonio J. Cuesta. Parameter splitting in dark energy: is dark energy the same in the background and in the cosmic structures? *JCAP*, 02:059, 2016. doi: 10.1088/1475-7516/2016/02/059.

[78] Michael J. Mortonson, Wayne Hu, and Dragan Huterer. Testable dark

energy predictions from current data. , 81(6):063007, March 2010. doi: 10.1103/PhysRevD.81.063007.

[79] Sheng Wang, Lam Hui, Morgan May, and Zoltan Haiman. Is Modified Gravity Required by Observations? An Empirical Consistency Test of Dark Energy Models. *Phys. Rev. D*, 76:063503, 2007. doi: 10.1103/PhysRevD.76.063503.

[80] V. Miranda and Cora Dvorkin. Model-Independent Predictions for Smooth Cosmic Acceleration Scenarios. *Phys. Rev. D*, 98(4):043537, 2018. doi: 10.1103/PhysRevD.98.043537.

[81] Mustapha Ishak, Amol Upadhye, and David N. Spergel. Probing cosmic acceleration beyond the equation of state: Distinguishing between dark energy and modified gravity models. *Phys. Rev. D*, 74:043513, 2006. doi: 10.1103/PhysRevD.74.043513.

[82] Dragan Huterer and Eric V. Linder. Separating Dark Physics from Physical Darkness: Minimalist Modified Gravity vs. Dark Energy. *Phys. Rev. D*, 75:023519, 2007. doi: 10.1103/PhysRevD.75.023519.

[83] Michael J. Mortonson, Dragan Huterer, and Wayne Hu. Figures of merit for present and future dark energy probes. , 82(6):063004, September 2010. doi: 10.1103/PhysRevD.82.063004.

[84] Julien Lesgourgues and Sergio Pastor. Massive neutrinos and cosmology. *Phys. Rept.*, 429:307–379, 2006. doi: 10.1016/j.physrep.2006.04.001.

[85] Daniel J. Eisenstein and Wayne Hu. Power spectra for cold dark matter and its variants. *Astrophys. J.*, 511:5, 1997. doi: 10.1086/306640.

[86] Angeliki Kiakotou, Oystein Elgaroy, and Ofer Lahav. Neutrino Mass, Dark Energy, and the Linear Growth Factor. *Phys. Rev. D*, 77:063005, 2008. doi: 10.1103/PhysRevD.77.063005.

[87] Uendert Andrade, Dhayaa Anbajagane, Rodrigo von Marttens, Dragan Huterer, and Jailson Alcaniz. A test of the standard cosmological model with geometry and growth. *JCAP*, 11:014, 2021. doi: 10.1088/1475-7516/2021/11/014.

[88] Eric V. Linder. Cosmic growth history and expansion history. *Phys. Rev. D*, 72:043529, 2005. doi: 10.1103/PhysRevD.72.043529.

[89] Spyros Basilakos and Fotios K. Anagnostopoulos. Growth index of matter perturbations in the light of Dark Energy Survey. *Eur. Phys. J. C*, 80(3):212, 2020. doi: 10.1140/epjc/s10052-020-7770-8.

[90] DES Collaboration, T. M. C. Abbott, M. Aguena, A. Alarcon, O. Alves, A. Amon, J. Annis, S. Avila, D. Bacon, E. Baxter, K. Bechtol, M. R. Becker, G. M. Bernstein, S. Birrer, J. Blazek, S. Bocquet, A. Brandao-Souza, S. L. Bridle, D. Brooks, D. L. Burke, H. Camacho, A. Campos, A. Carnero Rosell, M. Carrasco Kind, J. Carretero, F. J. Castander, R. Cawthon, C. Chang, A. Chen, R. Chen, A. Choi, C. Conselice, J. Cordero, M. Costanzi, M. Crocce, L. N. da Costa, M. E. S. Pereira, C. Davis, T. M. Davis, J. DeRose, S. Desai, E. Di Valentino, H. T. Diehl, S. Dodelson, P. Doel, C. Doux, A. Drlica-Wagner, K. Eckert, T. F. Eifler, F. Elsner, J. Elvin-Poole, S. Everett, X. Fang, A. Farahi, I. Ferrero, A. Ferté, B. Flaugher, P. Fosalba, D. Friedel, O. Friedrich, J. Frieman, J. García-Bellido, M. Gatti, L. Giani, T. Giannantonio, G. Giannini, D. Gruen, R. A. Gruendl, J. Gschwend, G. Gutierrez, N. Hamaus, I. Harrison, W. G. Hartley, K. Herner, S. R. Hinton, D. L. Hollowood, K. Honscheid, H. Huang, E. M. Huff, D. Huterer, B. Jain, D. J. James, M. Jarvis, N. Jeffrey, T. Jeltema, A. Kovacs, E. Krause, K. Kuehn, N. Kuropatkin, O. Lahav, S. Lee, P. F. Leget, P. Lemos, C. D. Leonard, A. R. Liddle, M. Lima, H. Lin, N. MacCrann, J. L. Marshall, J. McCullough, J. Mena-Fernández, F. Menanteau, R. Miquel, V. Miranda, J. J. Mohr, J. Muir, J. Myles, S. Nadathur, A. Navarro-Alsina, R. C. Nichol, R. L. C. Ogando, Y. Omori, A. Palmese, S. Pandey, Y. Park, M. Paterno, F. Paz-Chinchón, W. J. Percival, A. Pieres, A. A. Plazas Malagón, A. Porredon, J. Prat, M. Raveri, M. Rodriguez-Monroy, P. Rogozenski, R. P. Rollins, A. K. Romer, A. Roodman, R. Rosenfeld, A. J. Ross, E. S. Rykoff, S. Samuroff, C. Sánchez, E. Sanchez, J. Sanchez, D. Sanchez Cid, V. Scarpine, D. Scolnic, L. F. Secco, I. Sevilla-Noarbe, E. Sheldon, T. Shin, M. Smith, M. Soares-Santos, E. Suchyta, M. Tabbutt, G. Tarle, D. Thomas, C. To, A. Troja, M. A. Troxel, I. Tutusaus, T. N. Varga, M. Vincenzi, A. R. Walker, N. Weaverdyck, R. H. Wechsler, J. Weller, B. Yanny, B. Yin, Y. Zhang, and J. Zuntz. Dark Energy Survey Year 3 Results: Constraints on extensions to ΛCDM with weak lensing and galaxy clustering. *arXiv e-prints*, art. arXiv:2207.05766, July 2022.

[91] Carlos García-García, Jaime Ruiz Zapatero, David Alonso, Emilio Bellini, Pedro G. Ferreira, Eva-Maria Mueller, Andrina Nicola, and Pilar Ruiz-Lapuente. The growth of density perturbations in the last ∼10

billion years from tomographic large-scale structure data. *JCAP*, 10:030, 2021. doi: 10.1088/1475-7516/2021/10/030.

[92] Lukas Wenzl, Cyrille Doux, Chen Heinrich, Rachel Bean, Bhuvnesh Jain, Olivier Doré, Tim Eifler, and Xiao Fang. Cosmology with the Roman Space Telescope – Synergies with CMB lensing. *Mon. Not. Roy. Astron. Soc.*, 512(4):5311–5328, 2022. doi: 10.1093/mnras/stac790.

[93] Georges Obied, Cora Dvorkin, Chen Heinrich, Wayne Hu, and Vinicius Miranda. Inflationary Features and Shifts in Cosmological Parameters from Planck 2015 Data. *Phys. Rev. D*, 96(8):083526, 2017. doi: 10.1103/PhysRevD.96.083526.

[94] Marco Raveri and Cyrille Doux. Non-Gaussian estimates of tensions in cosmological parameters. , 104(4):043504, August 2021. doi: 10.1103/PhysRevD.104.043504.

[95] P. Lemos, M. Raveri, A. Campos, Y. Park, C. Chang, N. Weaverdyck, D. Huterer, A. R. Liddle, J. Blazek, R. Cawthon, A. Choi, J. DeRose, S. Dodelson, C. Doux, M. Gatti, D. Gruen, I. Harrison, E. Krause, O. Lahav, N. MacCrann, J. Muir, J. Prat, M. M. Rau, R. P. Rollins, S. Samuroff, J. Zuntz, M. Aguena, S. Allam, J. Annis, S. Avila, D. Bacon, G. M. Bernstein, E. Bertin, D. Brooks, D. L. Burke, A. Carnero Rosell, M. Carrasco Kind, J. Carretero, F. J. Castander, C. Conselice, M. Costanzi, M. Crocce, M. E. S. Pereira, T. M. Davis, J. De Vicente, S. Desai, H. T. Diehl, P. Doel, K. Eckert, T. F. Eifler, J. Elvin-Poole, S. Everett, A. E. Evrard, I. Ferrero, A. Ferté, B. Flaugher, P. Fosalba, J. Frieman, J. García-Bellido, E. Gaztanaga, D. W. Gerdes, T. Giannantonio, R. A. Gruendl, J. Gschwend, G. Gutierrez, W. G. Hartley, S. R. Hinton, D. L. Hollowood, K. Honscheid, B. Hoyle, E. M. Huff, D. J. James, M. Jarvis, M. Lima, M. A. G. Maia, M. March, J. L. Marshall, P. Martini, P. Melchior, F. Menanteau, R. Miquel, J. J. Mohr, R. Morgan, J. Myles, R. L. C. Ogando, A. Palmese, S. Pandey, F. Paz-Chinchón, A. A. Plazas Malagón, M. Rodriguez-Monroy, A. Roodman, E. Sanchez, V. Scarpine, M. Schubnell, L. F. Secco, S. Serrano, I. Sevilla-Noarbe, M. Smith, M. Soares-Santos, E. Suchyta, M. E. C. Swanson, G. Tarle, D. Thomas, C. To, M. A. Troxel, T. N. Varga, J. Weller, W. Wester, and DES Collaboration. Assessing tension metrics with dark energy survey and Planck data. , 505(4):6179–6194, August 2021. doi: 10.1093/mnras/stab1670.

[96] George Papamakarios, Theo Pavlakou, and Iain Murray. Masked

Autoregressive Flow for Density Estimation. *arXiv e-prints*, art. arXiv:1705.07057, May 2017.

[97] Byeonghee Yu, J. Colin Hill, and Blake D. Sherwin. Multitracer CMB delensing maps from Planck and WISE data. , 96(12):123511, December 2017. doi: 10.1103/PhysRevD.96.123511.

[98] Julien Carron, Antony Lewis, and Anthony Challinor. Internal delensing of Planck CMB temperature and polarization. , 2017(5):035, May 2017. doi: 10.1088/1475-7516/2017/05/035.

[99] Pavel Motloch and Wayne Hu. Tensions between direct measurements of the lens power spectrum from Planck data. *Phys. Rev. D*, 97(10): 103536, 2018. doi: 10.1103/PhysRevD.97.103536.

[100] Shi-Fan Chen, Zvonimir Vlah, and Martin White. A new analysis of galaxy 2-point functions in the BOSS survey, including full-shape information and post-reconstruction BAO. , 2022(2):008, February 2022. doi: 10.1088/1475-7516/2022/02/008.

[101] Hung-Jin Huang, Tim Eifler, Rachel Mandelbaum, Gary M. Bernstein, Anqi Chen, Ami Choi, Juan García-Bellido, Dragan Huterer, Elisabeth Krause, Eduardo Rozo, Sukhdeep Singh, Sarah Bridle, Joseph DeRose, Jack Elvin-Poole, Xiao Fang, Oliver Friedrich, Marco Gatti, Enrique Gaztanaga, Daniel Gruen, Will Hartley, Ben Hoyle, Mike Jarvis, Niall MacCrann, Vivian Miranda, Markus Rau, Judit Prat, Carles Sánchez, Simon Samuroff, Michael Troxel, Joe Zuntz, Tim Abbott, Michel Aguena, James Annis, Santiago Avila, Matthew Becker, Emmanuel Bertin, David Brooks, David Burke, Aurelio Carnero Rosell, Matias Carrasco Kind, Jorge Carretero, Francisco Javier Castander, Luiz da Costa, Juan De Vicente, Jörg Dietrich, Peter Doel, Spencer Everett, Brenna Flaugher, Pablo Fosalba, Josh Frieman, Robert Gruendl, Gaston Gutierrez, Samuel Hinton, Klaus Honscheid, David James, Kyler Kuehn, Ofer Lahav, Marcos Lima, Marcio Maia, Jennifer Marshall, Felipe Menanteau, Ramon Miquel, Francisco Paz-Chinchón, Andrés Plazas Malagón, Kathy Romer, Aaron Roodman, Eusebio Sanchez, Vic Scarpine, Santiago Serrano, Ignacio Sevilla, Mathew Smith, Marcelle Soares-Santos, Eric Suchyta, Molly Swanson, Gregory Tarle, Diehl H. Thomas, Jochen Weller, and DES Collaboration. Dark energy survey year 1 results: Constraining baryonic physics in the Universe. , 502(4):6010–6031, April 2021. doi: 10.1093/mnras/stab357.

[102] Nickolas Kokron, Joseph DeRose, Shi-Fan Chen, Martin White, and Risa H. Wechsler. The cosmology dependence of galaxy clustering and lensing from a hybrid N-body–perturbation theory model. *Mon. Not. Roy. Astron. Soc.*, 505(1):1422–1440, 2021. doi: 10.1093/mnras/stab1358.

[103] Zheng Zheng, Andreas A. Berlind, David H. Weinberg, Andrew J. Benson, Carlton M. Baugh, Shaun Cole, Romeel Davé, Carlos S. Frenk, Neal Katz, and Cedric G. Lacey. Theoretical Models of the Halo Occupation Distribution: Separating Central and Satellite Galaxies. , 633 (2):791–809, November 2005. doi: 10.1086/466510.

[104] Idit Zehavi, Zheng Zheng, David H. Weinberg, Michael R. Blanton, Neta A. Bahcall, Andreas A. Berlind, Jon Brinkmann, Joshua A. Frieman, James E. Gunn, Robert H. Lupton, Robert C. Nichol, Will J. Percival, Donald P. Schneider, Ramin A. Skibba, Michael A. Strauss, Max Tegmark, and Donald G. York. Galaxy Clustering in the Completed SDSS Redshift Survey: The Dependence on Color and Luminosity. , 736 (1):59, July 2011. doi: 10.1088/0004-637X/736/1/59.

[105] K. Kuijken, C. Heymans, A. Dvornik, H. Hildebrandt, J. T. A. de Jong, A. H. Wright, T. Erben, M. Bilicki, B. Giblin, H. Y. Shan, F. Getman, A. Grado, H. Hoekstra, L. Miller, N. Napolitano, M. Paolilo, M. Radovich, P. Schneider, W. Sutherland, M. Tewes, C. Tortora, E. A. Valentijn, and G. A. Verdoes Kleijn. The fourth data release of the Kilo-Degree Survey: ugri imaging and nine-band optical-IR photometry over 1000 square degrees. , 625:A2, May 2019. doi: 10.1051/0004-6361/201834918.

[106] Marika Asgari, Chieh-An Lin, Benjamin Joachimi, Benjamin Giblin, Catherine Heymans, Hendrik Hildebrandt, Arun Kannawadi, Benjamin Stölzner, Tilman Tröster, Jan Luca van den Busch, Angus H. Wright, Maciej Bilicki, Chris Blake, Jelte de Jong, Andrej Dvornik, Thomas Erben, Fedor Getman, Henk Hoekstra, Fabian Köhlinger, Konrad Kuijken, Lance Miller, Mario Radovich, Peter Schneider, HuanYuan Shan, and Edwin Valentijn. KiDS-1000 cosmology: Cosmic shear constraints and comparison between two point statistics. , 645:A104, January 2021. doi: 10.1051/0004-6361/202039070.

[107] C. To, E. Krause, E. Rozo, H. Wu, D. Gruen, R. H. Wechsler, T. F. Eifler, E. S. Rykoff, M. Costanzi, M. R. Becker, G. M. Bernstein, J. Blazek, S. Bocquet, S. L. Bridle, R. Cawthon, A. Choi, M. Crocce, C. Davis,

J. DeRose, A. Drlica-Wagner, J. Elvin-Poole, X. Fang, A. Farahi, O. Friedrich, M. Gatti, E. Gaztanaga, T. Giannantonio, W. G. Hartley, B. Hoyle, M. Jarvis, N. MacCrann, T. McClintock, V. Miranda, M. E. S. Pereira, Y. Park, A. Porredon, J. Prat, M. M. Rau, A. J. Ross, S. Samuroff, C. Sánchez, I. Sevilla-Noarbe, E. Sheldon, M. A. Troxel, T. N. Varga, P. Vielzeuf, Y. Zhang, J. Zuntz, T. M. C. Abbott, M. Aguena, A. Amon, J. Annis, S. Avila, E. Bertin, S. Bhargava, D. Brooks, D. L. Burke, A. Carnero Rosell, M. Carrasco Kind, J. Carretero, C. Chang, C. Conselice, L. N. da Costa, T. M. Davis, S. Desai, H. T. Diehl, J. P. Dietrich, S. Everett, A. E. Evrard, I. Ferrero, B. Flaugher, P. Fosalba, J. Frieman, J. García-Bellido, R. A. Gruendl, G. Gutierrez, S. R. Hinton, D. L. Hollowood, K. Honscheid, D. Huterer, D. J. James, T. Jeltema, R. Kron, K. Kuehn, N. Kuropatkin, M. Lima, M. A. G. Maia, J. L. Marshall, F. Menanteau, R. Miquel, R. Morgan, J. Muir, J. Myles, A. Palmese, F. Paz-Chinchón, A. A. Plazas, A. K. Romer, A. Roodman, E. Sanchez, B. Santiago, V. Scarpine, S. Serrano, M. Smith, E. Suchyta, M. E. C. Swanson, G. Tarle, D. Thomas, D. L. Tucker, J. Weller, W. Wester, R. D. Wilkinson, and DES Collaboration. Dark Energy Survey Year 1 Results: Cosmological Constraints from Cluster Abundances, Weak Lensing, and Galaxy Correlations. , 126(14):141301, April 2021. doi: 10.1103/PhysRevLett.126.141301.

[108] F. Feroz, M. P. Hobson, and M. Bridges. MultiNest: an efficient and robust Bayesian inference tool for cosmology and particle physics. *Mon. Not. Roy. Astron. Soc.*, 398:1601–1614, 2009. doi: 10.1111/j.1365-2966.2009.14548.x.

[109] W. J. Handley, M. P. Hobson, and A. N. Lasenby. POLYCHORD: next-generation nested sampling. , 453(4):4384–4398, November 2015. doi: 10.1093/mnras/stv1911.

[110] Steven Weinberg. Anthropic bound on the cosmological constant. *Phys. Rev. Lett.*, 59:2607–2610, Nov 1987. doi: 10.1103/PhysRevLett.59.2607. URL `https://link.aps.org/doi/10.1103/PhysRevLett.59.2607`.

[111] Bharat Ratra and P. J. E. Peebles. Cosmological consequences of a rolling homogeneous scalar field. , 37(12):3406–3427, June 1988. doi: 10.1103/PhysRevD.37.3406.

[112] Sean M. Carroll, Mark Hoffman, and Mark Trodden. Can the dark energy equation-of-state parameter w be less than -1? , 68(2):023509, July 2003. doi: 10.1103/PhysRevD.68.023509.

[113] Antony Lewis, Anthony Challinor, and Anthony Lasenby. Efficient computation of CMB anisotropies in closed FRW models. , 538:473–476, 2000. doi: 10.1086/309179.

[114] Cullan Howlett, Antony Lewis, Alex Hall, and Anthony Challinor. CMB power spectrum parameter degeneracies in the era of precision cosmology. , 1204:027, 2012. doi: 10.1088/1475-7516/2012/04/027.

[115] Diego Blas, Julien Lesgourgues, and Thomas Tram. The Cosmic Linear Anisotropy Solving System (CLASS). Part II: Approximation schemes. , 2011(7):034, July 2011. doi: 10.1088/1475-7516/2011/07/034.

[116] Hideo Kodama and Misao Sasaki. Cosmological Perturbation Theory. *Progress of Theoretical Physics Supplement*, 78:1, January 1984. doi: 10.1143/PTPS.78.1.

[117] John Joseph M. Carrasco, Mark P. Hertzberg, and Leonardo Senatore. The effective field theory of cosmological large scale structures. *Journal of High Energy Physics*, 2012:82, September 2012. doi: 10.1007/JHEP09(2012)082.

[118] Wenjuan Fang, Wayne Hu, and Antony Lewis. Crossing the Phantom Divide with Parameterized Post-Friedmann Dark Energy. *Phys. Rev. D*, 78:087303, 2008. doi: 10.1103/PhysRevD.78.087303.

[119] Wayne Hu. Crossing the phantom divide: Dark energy internal degrees of freedom. *Phys. Rev. D*, 71:047301, 2005. doi: 10.1103/PhysRevD.71.047301.

[120] Wayne Hu. Structure formation with generalized dark matter. *Astrophys. J.*, 506:485–494, 1998. doi: 10.1086/306274.

[121] Wayne Hu. Parametrized Post-Friedmann Signatures of Acceleration in the CMB. *Phys. Rev. D*, 77:103524, 2008. doi: 10.1103/PhysRevD.77.103524.

[122] Wilmar Cardona, Lukas Hollenstein, and Martin Kunz. The traces of anisotropic dark energy in light of Planck. , 2014(7):032, July 2014. doi: 10.1088/1475-7516/2014/07/032.

[123] Gabriela Garcia-Arroyo, Jorge L. Cervantes-Cota, Ulises Nucamendi, and Alejandro Aviles. Effects of dark energy anisotropic stress on the matter power spectrum. *Physics of the Dark Universe*, 30:100668, December 2020. doi: 10.1016/j.dark.2020.100668.

[124] A. Spurio Mancini, F. Köhlinger, B. Joachimi, V. Pettorino, B. M. Schäfer, R. Reischke, Edo van Uitert, S. Brieden, M. Archidiacono, and J. Lesgourgues. KiDS + GAMA: constraints on horndeski gravity from combined large-scale structure probes. *Mon. Not. Roy. Astron. Soc.*, 490 (2):2155–2177, 2019. doi: 10.1093/mnras/stz2581.

[125] Luca Amendola and Shinji Tsujikawa. *Dark Energy: Theory and Observations*. Cambridge University Press, 2010. doi: 10.1017/CBO9780511750823.

[126] Gregory Walter Horndeski. Second-Order Scalar-Tensor Field Equations in a Four-Dimensional Space. *International Journal of Theoretical Physics*, 10(6):363–384, September 1974. doi: 10.1007/BF01807638.

[127] Alberto Nicolis, Riccardo Rattazzi, and Enrico Trincherini. Galileon as a local modification of gravity. , 79(6):064036, March 2009. doi: 10.1103/PhysRevD.79.064036.

[128] Robert J. Scherrer. Purely kinetic k-essence as unified dark matter. *Phys. Rev. Lett.*, 93:011301, 2004. doi: 10.1103/PhysRevLett.93.011301.

[129] C. Armendáriz-Picón, T. Damour, and V. Mukhanov. k-inflation. *Physics Letters B*, 458(2):209–218, 1999. ISSN 0370-2693. doi: https://doi.org/10.1016/S0370-2693(99)00603-6. URL `https://www.sciencedirect.com/science/article/pii/S0370269399006036`.

[130] Carlos García-García, Emilio Bellini, Pedro G. Ferreira, Dina Traykova, and Miguel Zumalacárregui. Theoretical priors in scalar-tensor cosmologies: Thawing quintessence. *Physical Review D*, 101(6), Mar 2020. ISSN 2470-0029. doi: 10.1103/physrevd.101.063508. URL `http://dx.doi.org/10.1103/PhysRevD.101.063508`.

[131] Paul J. Steinhardt, Limin Wang, and Ivaylo Zlatev. Cosmological tracking solutions. , 59(12):123504, June 1999. doi: 10.1103/PhysRevD.59.123504.

[132] Takeshi Chiba, Takahiro Okabe, and Masahide Yamaguchi. Kinetically driven quintessence. *Phys. Rev. D*, 62:023511, 2000. doi: 10.1103/PhysRevD.62.023511.

[133] Kazuharu Bamba, Jiro Matsumoto, and Shin'ichi Nojiri. Cosmological perturbations in k-essence model. *Phys. Rev. D*, 85:084026, 2012. doi: 10.1103/PhysRevD.85.084026.

[134] Federico Piazza and Shinji Tsujikawa. Dilatonic ghost condensate as dark energy. *JCAP*, 07:004, 2004. doi: 10.1088/1475-7516/2004/07/004.

[135] Ryuichi Takahashi, Masanori Sato, Takahiro Nishimichi, Atsushi Taruya, and Masamune Oguri. Revising the Halofit Model for the Nonlinear Matter Power Spectrum. *Astrophys. J.*, 761:152, 2012. doi: 10.1088/0004-637X/761/2/152.

[136] Luciano Casarini, Andrea V. Macciò, and Silvio A. Bonometto. Dynamical dark energy simulations: high accuracy power spectra at high redshift. , 2009(3):014, March 2009. doi: 10.1088/1475-7516/2009/03/014.

[137] Euclid Collaboration, M. Knabenhans, J. Stadel, D. Potter, J. Dakin, S. Hannestad, T. Tram, S. Marelli, A. Schneider, R. Teyssier, P. Fosalba, S. Andreon, N. Auricchio, C. Baccigalupi, A. Balaguera-Antolínez, M. Baldi, S. Bardelli, P. Battaglia, R. Bender, A. Biviano, C. Bodendorf, E. Bozzo, E. Branchini, M. Brescia, C. Burigana, R. Cabanac, S. Camera, V. Capobianco, A. Cappi, C. Carbone, J. Carretero, C. S. Carvalho, R. Casas, S. Casas, M. Castellano, G. Castignani, S. Cavuoti, R. Cledassou, C. Colodro-Conde, G. Congedo, C. J. Conselice, L. Conversi, Y. Copin, L. Corcione, J. Coupon, H. M. Courtois, A. Da Silva, S. de la Torre, D. Di Ferdinando, C. A. J. Duncan, X. Dupac, G. Fabbian, S. Farrens, P. G. Ferreira, F. Finelli, M. Frailis, E. Franceschi, S. Galeotta, B. Garilli, C. Giocoli, G. Gozaliasl, J. Graciá-Carpio, F. Grupp, L. Guzzo, W. Holmes, F. Hormuth, H. Israel, K. Jahnke, E. Keihanen, S. Kermiche, C. C. Kirkpatrick, B. Kubik, M. Kunz, H. Kurki-Suonio, S. Ligori, P. B. Lilje, I. Lloro, D. Maino, O. Marggraf, K. Markovic, N. Martinet, F. Marulli, R. Massey, N. Mauri, S. Maurogordato, E. Medinaceli, M. Meneghetti, B. Metcalf, G. Meylan, M. Moresco, B. Morin, L. Moscardini, E. Munari, C. Neissner, S. M. Niemi, C. Padilla, S. Paltani, F. Pasian, L. Patrizii, V. Pettorino, S. Pires, G. Polenta, M. Poncet, F. Raison, A. Renzi, J. Rhodes, G. Riccio, E. Romelli, M. Roncarelli, R. Saglia, A. G. Sánchez, D. Sapone, P. Schneider, V. Scottez, A. Secroun, S. Serrano, C. Sirignano, G. Sirri, L. Stanco, F. Sureau, P. Tallada Crespí, A. N. Taylor, M. Tenti, I. Tereno, R. Toledo-Moreo, F. Torradeflot, L. Valenziano, J. Valiviita, T. Vassallo, M. Viel, Y. Wang, N. Welikala, L. Whittaker, A. Zacchei, and E. Zucca. Euclid preparation: IX. EuclidEmulator2 - power spectrum emulation with massive neutrinos and self-consistent dark energy perturbations. , 505(2):2840–2869, August 2021. doi: 10.1093/mnras/stab1366.

[138] Bill S. Wright, Ashim Sen Gupta, Tessa Baker, and Georgios Valogian-

nis. Hi-COLA: Fast, approximate simulations of structure formation in Horndeski gravity. *arXiv e-prints*, art. arXiv:2209.01666, September 2022. doi: 10.48550/arXiv.2209.01666.

[139] João Rebouças, Jonathan Gordon, Diogo H. F. de Souza, Kunhao Zhong, Vivian Miranda, Rogerio Rosenfeld, Tim Eifler, and Elisabeth Krause. Early dark energy constraints with late-time expansion marginalization. *arXiv e-prints*, art. arXiv:2302.07333, February 2023. doi: 10.48550/arXiv.2302.07333.

[140] N. Aghanim et al. Planck intermediate results. LI. Features in the cosmic microwave background temperature power spectrum and shifts in cosmological parameters. *Astron. Astrophys.*, 607:A95, 2017. doi: 10.1051/0004-6361/201629504.

[141] Kenneth C. Wong, Sherry H. Suyu, Geoff C. F. Chen, Cristian E. Rusu, Martin Millon, Dominique Sluse, Vivien Bonvin, Christopher D. Fassnacht, Stefan Taubenberger, Matthew W. Auger, Simon Birrer, James H. H. Chan, Frederic Courbin, Stefan Hilbert, Olga Tihhonova, Tommaso Treu, Adriano Agnello, Xuheng Ding, Inh Jee, Eiichiro Komatsu, Anowar J. Shajib, Alessandro Sonnenfeld, Roger D. Blandford, Léon V. E. Koopmans, Philip J. Marshall, and Georges Meylan. H0LiCOW - XIII. A 2.4 per cent measurement of H_0 from lensed quasars: 5.3σ tension between early- and late-Universe probes. , 498(1):1420–1439, October 2020. doi: 10.1093/mnras/stz3094.

[142] Adam G. Riess. The Expansion of the Universe is Faster than Expected. *Nature Rev. Phys.*, 2(1):10–12, 2019. doi: 10.1038/s42254-019-0137-0.

[143] Adam G. Riess, Stefano Casertano, Wenlong Yuan, Lucas M. Macri, and Dan Scolnic. Large Magellanic Cloud Cepheid Standards Provide a 1% Foundation for the Determination of the Hubble Constant and Stronger Evidence for Physics beyond ΛCDM. *Astrophys. J.*, 876(1):85, 2019. doi: 10.3847/1538-4357/ab1422.

[144] Kenneth C. Wong, Sherry H. Suyu, Geoff C. F. Chen, Cristian E. Rusu, Martin Millon, Dominique Sluse, Vivien Bonvin, Christopher D. Fassnacht, Stefan Taubenberger, Matthew W. Auger, Simon Birrer, James H. H. Chan, Frederic Courbin, Stefan Hilbert, Olga Tihhonova, Tommaso Treu, Adriano Agnello, Xuheng Ding, Inh Jee, Eiichiro Komatsu, Anowar J. Shajib, Alessandro Sonnenfeld, Roger D. Blandford, Léon V. E. Koopmans, Philip J. Marshall, and Georges Meylan. H0LiCOW - XIII. A 2.4 per cent measurement of H_0 from lensed quasars: 5.3σ

tension between early- and late-Universe probes. , 498(1):1420–1439, October 2020. doi: 10.1093/mnras/stz3094.

[145] G. Efstathiou. A Lockdown Perspective on the Hubble Tension (with comments from the SH0ES team). *arXiv e-prints*, art. arXiv:2007.10716, July 2020. doi: 10.48550/arXiv.2007.10716.

[146] Lloyd Knox and Marius Millea. Hubble constant hunter's guide. *Phys. Rev. D*, 101(4):043533, 2020. doi: 10.1103/PhysRevD.101.043533.

[147] Tanvi Karwal and Marc Kamionkowski. Dark energy at early times, the Hubble parameter, and the string axiverse. , 94(10):103523, November 2016. doi: 10.1103/PhysRevD.94.103523.

[148] Vivian Poulin, Tristan L. Smith, Tanvi Karwal, and Marc Kamionkowski. Early Dark Energy can Resolve the Hubble Tension. , 122(22):221301, June 2019. doi: 10.1103/PhysRevLett.122.221301.

[149] Prateek Agrawal, Francis-Yan Cyr-Racine, David Pinner, and Lisa Randall. Rock 'n' Roll Solutions to the Hubble Tension. *arXiv e-prints*, art. arXiv:1904.01016, April 2019. doi: 10.48550/arXiv.1904.01016.

[150] Meng-Xiang Lin, Giampaolo Benevento, Wayne Hu, and Marco Raveri. Acoustic dark energy: Potential conversion of the Hubble tension. , 100 (6):063542, September 2019. doi: 10.1103/PhysRevD.100.063542.

[151] Florian Niedermann and Martin S. Sloth. New Early Dark Energy. *arXiv e-prints*, art. arXiv:1910.10739, October 2019. doi: 10.48550/arXiv.1910.10739.

[152] Tanvi Karwal, Marco Raveri, Bhuvnesh Jain, Justin Khoury, and Mark Trodden. Chameleon early dark energy and the Hubble tension. , 105 (6):063535, March 2022. doi: 10.1103/PhysRevD.105.063535.

[153] Katherine Freese and Martin Wolfgang Winkler. Chain early dark energy: A Proposal for solving the Hubble tension and explaining today's dark energy. , 104(8):083533, October 2021. doi: 10.1103/PhysRevD.104.083533.

[154] Meng-Xiang Lin, Evan McDonough, J. Colin Hill, and Wayne Hu. A Dark Matter Trigger for Early Dark Energy Coincidence. *arXiv e-prints*, art. arXiv:2212.08098, December 2022. doi: 10.48550/arXiv.2212.08098.

[155] J. Colin Hill, Evan McDonough, Michael W. Toomey, and Stephon Alexander. Early dark energy does not restore cosmological concordance. *Phys. Rev. D*, 102(4):043507, 2020. doi: 10.1103/PhysRevD.102.043507.

[156] J. Colin Hill, Erminia Calabrese, Simone Aiola, Nicholas Battaglia, Boris Bolliet, Steve K. Choi, Mark J. Devlin, Adriaan J. Duivenvoorden, Jo Dunkley, Simone Ferraro, Patricio A. Gallardo, Vera Gluscevic, Matthew Hasselfield, Matt Hilton, Adam D. Hincks, Renée Hložek, Brian J. Koopman, Arthur Kosowsky, Adrien La Posta, Thibaut Louis, Mathew S. Madhavacheril, Jeff McMahon, Kavilan Moodley, Sigurd Naess, Umberto Natale, Federico Nati, Laura Newburgh, Michael D. Niemack, Lyman A. Page, Bruce Partridge, Frank J. Qu, Maria Salatino, Alessandro Schillaci, Neelima Sehgal, Blake D. Sherwin, Cristóbal Sifón, David N. Spergel, Suzanne T. Staggs, Emilie R. Storer, Alexander van Engelen, Eve M. Vavagiakis, Edward J. Wollack, and Zhilei Xu. Atacama Cosmology Telescope: Constraints on prerecombination early dark energy. , 105(12):123536, June 2022. doi: 10.1103/PhysRevD.105.123536.

[157] Lachlan Lancaster, Francis-Yan Cyr-Racine, Lloyd Knox, and Zhen Pan. A tale of two modes: neutrino free-streaming in the early universe. , 2017 (7):033, July 2017. doi: 10.1088/1475-7516/2017/07/033.

[158] Anirban Das and Subhajit Ghosh. Flavor-specific interaction favors strong neutrino self-coupling in the early universe. , 2021(7):038, July 2021. doi: 10.1088/1475-7516/2021/07/038.

[159] Thejs Brinckmann, Jae Hyeok Chang, and Marilena LoVerde. Self-interacting neutrinos, the Hubble parameter tension, and the cosmic microwave background. , 104(6):063523, September 2021. doi: 10.1103/PhysRevD.104.063523.

[160] Shouvik Roy Choudhury, Steen Hannestad, and Thomas Tram. Updated constraints on massive neutrino self-interactions from cosmology in light of the H_0 tension. , 2021(3):084, March 2021. doi: 10.1088/1475-7516/2021/03/084.

[161] Christina D. Kreisch, Minsu Park, Erminia Calabrese, Francis-Yan Cyr-Racine, Rui An, J. Richard Bond, Olivier Dore, Jo Dunkley, Patricio Gallardo, Vera Gluscevic, J. Colin Hill, Adam D. Hincks, Mathew S. Madhavacheril, Jeff McMahon, Kavilan Moodley, Thomas W. Morris, Federico Nati, Lyman A. Page, Bruce Partridge, Maria Salatino, Cristobal Sifon, David N. Spergel, Cristian Vargas, and Edward J. Wollack. The Atacama Cosmology Telescope: The Persistence of Neu-

trino Self-Interaction in Cosmological Measurements. *arXiv e-prints*, art. arXiv:2207.03164, July 2022. doi: 10.48550/arXiv.2207.03164.

[162] Daniel Aloni, Asher Berlin, Melissa Joseph, Martin Schmaltz, and Neal Weiner. A Step in understanding the Hubble tension. , 105(12):123516, June 2022. doi: 10.1103/PhysRevD.105.123516.

[163] Melissa Joseph, Daniel Aloni, Martin Schmaltz, Eashwar N. Sivarajan, and Neal Weiner. A Step in Understanding the S_8 Tension. *arXiv e-prints*, art. arXiv:2207.03500, July 2022. doi: 10.48550/arXiv.2207.03500.

[164] Ashish Vaswani, Noam Shazeer, Niki Parmar, Jakob Uszkoreit, Llion Jones, Aidan N. Gomez, Lukasz Kaiser, and Illia Polosukhin. Attention Is All You Need. *arXiv e-prints*, art. arXiv:1706.03762, June 2017. doi: 10.48550/arXiv.1706.03762.

[165] Aston Zhang, Zachary C. Lipton, Mu Li, and Alexander J. Smola. Dive into Deep Learning. *arXiv e-prints*, art. arXiv:2106.11342, June 2021. doi: 10.48550/arXiv.2106.11342.

[166] Diederik P. Kingma and Jimmy Ba. Adam: A Method for Stochastic Optimization. *arXiv e-prints*, art. arXiv:1412.6980, December 2014. doi: 10.48550/arXiv.1412.6980.

[167] Supranta S. Boruah, Tim Eifler, Vivian Miranda, and Sai Krishanth P. M. Accelerating cosmological inference with Gaussian processes and neural networks – an application to LSST Y1 weak lensing and galaxy clustering. 3 2022.

[168] Chun-Hao To, Eduardo Rozo, Elisabeth Krause, Hao-Yi Wu, Risa H. Wechsler, and Andrés N. Salcedo. LINNA: Likelihood Inference Neural Network Accelerator. , 2023(1):016, January 2023. doi: 10.1088/1475-7516/2023/01/016.